# CHAPTER 1

## Introduction

### 1.1 Overview of Atmospheric Pressure Discharge

The numerous applications of atmospheric pressure discharges accelerated the development and research in this area. By dispensing with vacuum system, atmospheric pressure discharges become economical and easy to handle, attracting much interest by many researchers from all over the world. The atmospheric pressure discharge is an alternative for low pressure discharge in various applications. The detailed study which include the physical interpretation of the discharge regimes and the plasma chemistry of atmospheric pressure discharge that focused mainly on the dielectric barrier discharge configuration started to progress rapidly after the 90s by Eliasson & Kogelschatz (Eliasson & Kogelschatz, 1991b), Okazaki et al. (Okazaki, Kogoma, Uehara, & Kimura, 1993), Massines & Gouda (Massines & Gouda, 1998) and Roth et al. (Roth, Nourgostar, & Bonds, 2007) even though the study of this type of discharge was carried out since several decades ago. The detailed investigation was prohibited due to the lack of advance and high performance research instruments before the 90s (Pappas, 2011).

The atmospheric discharge can be categorized into thermal and non-thermal types as depicted in Table 1.1. The sources of thermal plasma jet included transferred arc, DC plasma torch and RF inductively coupled plasma torch (Boulos, 1991). The temperature of this type of discharge is very high, ranging from 5000 K up to 50000 K (Kogelschatz, Akishev, & Napartovich, 2005, p.19). The high temperature plasma sources are widely used in material processing such as plasma spray to produce layers of coatings on the substrate/film (Bonizzoni & Vassallo, 2002; Yoshida, 1990), plasma synthesis of fine

powders down to nanometer size (Pfender, 1999), metal cutting (Fauchais & Vardelle, 1997; Ramakrishnan & Rogozinski, 1997; Hoult, Pashby, & Chan, 1995) and plasma welding (Bertrand, Ignatiev, Flamant, & Smurov, 2000).

There are few ways to generate non-thermal plasma at atmospheric pressure namely corona discharge, dielectric barrier discharge, RF discharge, microwave discharge, and plasma jet by using RF, microwave, pulsed, AC or DC excitation schemes. Among the plasma sources mentioned, non-thermal plasma jet is a more recently generated type which is the main interest in this work.

**Table. 1.1.** Characteristics of low temperature plasma and high temperature plasma.

| Low Temperature Plasma | | High Temperature Plasma |
|---|---|---|
| Thermal | Non-thermal | $T_e \approx T_i \approx T \gtrsim 10^7$ K |
| $T_e \approx T_i \approx T_n \lesssim 2 \times 10^4$ K | $T_i \approx T_n \approx 300$ K<br>$T_i \ll T_e \lesssim 10^5$ K | |
| Plasma torch<br>Arc plasma | Corona discharge<br>Barrier discharge<br>RF discharge<br>Microwave discharge<br>Low pressure glow discharge<br>Plasma Jet | Fusion plasma |

The non-thermal types are also referred to as non-equilibrium plasmas, in which the total number density of ions and electrons are much fewer than the total number density of the neutral particles (Eliasson & Kogelschatz, 1991). Very often the temperature of non-thermal plasmas is near to room temperature. The electron temperature in non-thermal plasma is much higher than ions and neutral gas particles temperature. This is because most of the energy generated in the discharge is gained by electrons to ionize or excite other molecules or atoms producing excited species and radicals. Conversely, ions and neutral gain less energy than electrons due to lower energy exchange with other particles and remain cold (Ehlbeck et al., 2011). When all the particles (electrons,

ions and neutral gas particles) have temperatures close to each other, the discharge is in equilibrium state. In this case, the gas is significantly ionized compared to non-thermal plasma. However, the lower degree of ionization in non-thermal plasma is capable of producing higher concentration of reactive species (radicals and excited species) by energetic electrons. Hence, the discharges generated under this category are usually very reactive (Kong, 2006). The high reactivity and non-thermal feature of the plasmas have lead to a variety of applications such as surface activation to increase surface energy, surface cleaning to remove contaminants, destruction of waste, surface etching to create a relief, surface coating (Tendero, Tixier, Tristant, Desmaison, & Leprince, 2006), bacterial deactivation (Laroussi, 2002), and sterilization of bottles (Koulik, Begounov, & Goloviatinskii, 1999) and etc.

## 1.2 Atmospheric Pressure Non-Thermal Plasma Jet

Two types of plasma jet can be generated under atmospheric pressure, that is, thermal and non-thermal types. The thermal type has been in use (e.g. plasma torch) for many decades but the non-thermal atmospheric plasma jet was first described by Koinuma et al. in 1992 (Koinuma et. al, 1992). Generally, the plasma jet can be designed in compact size which makes it portable and it can be operated at atmospheric environment. The dimension and electrode shape of the plasma jet is flexible. It can be scaled up to the dimension needed in industrial applications (Schutze et al., 1998) or arranged in arrays to increase the production rate in industrial processing. The atmospheric pressure non-thermal plasma jet is characterized by low electron temperature (1-2 eV) and gas temperature where the jet generated is usually near to room temperature. The cold behavior of plasma jet is described in many literatures. The cold, compact size and portable feature of plasma jet is widely used in material

processing, biological and biomedical applications (Wagner et al., 2003; Laroussi, 2002).

Various configurations of plasma jet were introduced, usually comprised of a centre needle electrode, rod electrode or hollow electrode inside the glass/quartz tube. There exist configurations modified from the dielectric barrier discharge (DBD) arrangement with the electrodes placed outside the tube.

## 1.3 Motivation and Objective

The economical way of generating non-thermal plasma at atmospheric pressure with the elimination of vacuum setup that eases the installation as well as its non-thermal behavior which is suitable to treat thermally sensitive specimens without damage, leading to various applications in material processing have drawn our interest in this study. Plasma jets are often produced at the open end of capillary tubes with little or no constriction in the gas flow (Zhang, Sun, Wang, & Wang, 2006; Lu et al., 2008; Laroussi, Hynes, Akan, Lu, & Tendero, 2008). However we worked on a variant design in which the gas flow is significantly constricted by a small orifice (nozzle) such that the internal DBD discharge was subjected to pressure rising above one atmosphere, and the plasma jet could be formed when the gas exited the nozzle at high speed (up to $M_a$=0.7 at corrected gas flow rate of 12 LPM) into ambient atmospheric air. The filamentary DBD mode was chosen as it could be easily produced by AC high voltage at a few kHz.

The objectives of this work were to characterize the DBD jet produced and apply it for surface treatment of plastic film. Electrical and optical characteristics as well as the physical structure of the jet were investigated. The electrical characteristics included the current-voltage relationship as well as the charge transferred in the discharge and the jet. The optical characterization involving study of the optical emission spectra could

indicate the active species produced in the jet. These characteristics were investigated for different gas compositions, gas flow rates and applied voltages. On the application to surface treatment, macroscopic property of the surface such as wettability was obtained through contact angle measurement.

## 1.4 Layout of Dissertation

Introduction to the topic of research as well as the motivation and objective of this work has been given in the preceding sections of this chapter. Chapter 2 contains the overview of DBD including various configurations, breakdown phenomena and its historical development. The development of DBD jet which covered different design of the jet with different excitation schemes and various useful applications are presented in this chapter as well. Chapter 3 covers the experimental setup with detailed description of the configuration of DBD jet system, H.V. power supply, gas flow system and different diagnostics methods to study the characteristics of the DBD jet. Next, the setup and procedure for surface treatment is described. The results are presented and discussed in chapters 4 and 5. Chapter 4 focuses on the electrical and optical behaviour of DBD jet while chapter 5 describes about the effect of treatment time as well as the ageing effect on the treated Mylar surface. The results obtained are compared with the results reported in the literature. The last chapter is devoted to a summary of the findings obtained and suggestions for future works and improvement.

# CHAPTER 2

## Dielectric Barrier Discharge Jet

### 2.1 Dielectric Barrier Discharges (DBD)

#### 2.1.1 DBD Configuration

DBD system consists of two metal electrodes with at least one of the electrode insulated by dielectric material. It can be generated through volume discharge arrangement and surface discharge arrangement (Kogelschatz, 2010) in various configurations as shown in Fig. 2.1(a)-(l). Electrodes are separated by a gas gap for volume discharge arrangement and the gap width usually varies from 0.1 mm to a few cm. The discharge bridges the gap when sufficient voltage is applied across the electrodes. For surface discharge arrangement, the electrodes are in contact with the dielectric layer where no gas gap is needed for this arrangement, therefore, the luminous discharge area is observed on the surface of dielectric layer (Gibalov & Pietsch, 2000). Surface DBD was introduced by Masuda et al. for ozone production (Masuda, Akutsu, Kuroda, Awatsu, & Shibuya, 1988). They fabricated the high voltage electrode in the form of strips and the grounded electrode was a film which was separated by a cylindrical or planar dielectric layer as shown in Fig. 2.1(h). Another electrode arrangement of surface barrier discharge where the electrodes are embedded in the dielectric as shown in Fig. 2.1(i), is commonly used in the AC plasma display panel (Boeuf, 2003).

Common dielectric materials being used are glass, alumina, mica, quartz, ceramics ($Al_2O_3$) and polymer layers. The use of dielectric material is to restrict the discharge

current and prevent arc transition with large current flowing between the two metal electrodes. This is achieved when charges accumulated on the dielectric surface creates an electric field that opposes the applied voltage which reduces the electric field strength at the location of filament formation until the filament is extinguished (Kogelschatz, 2010).

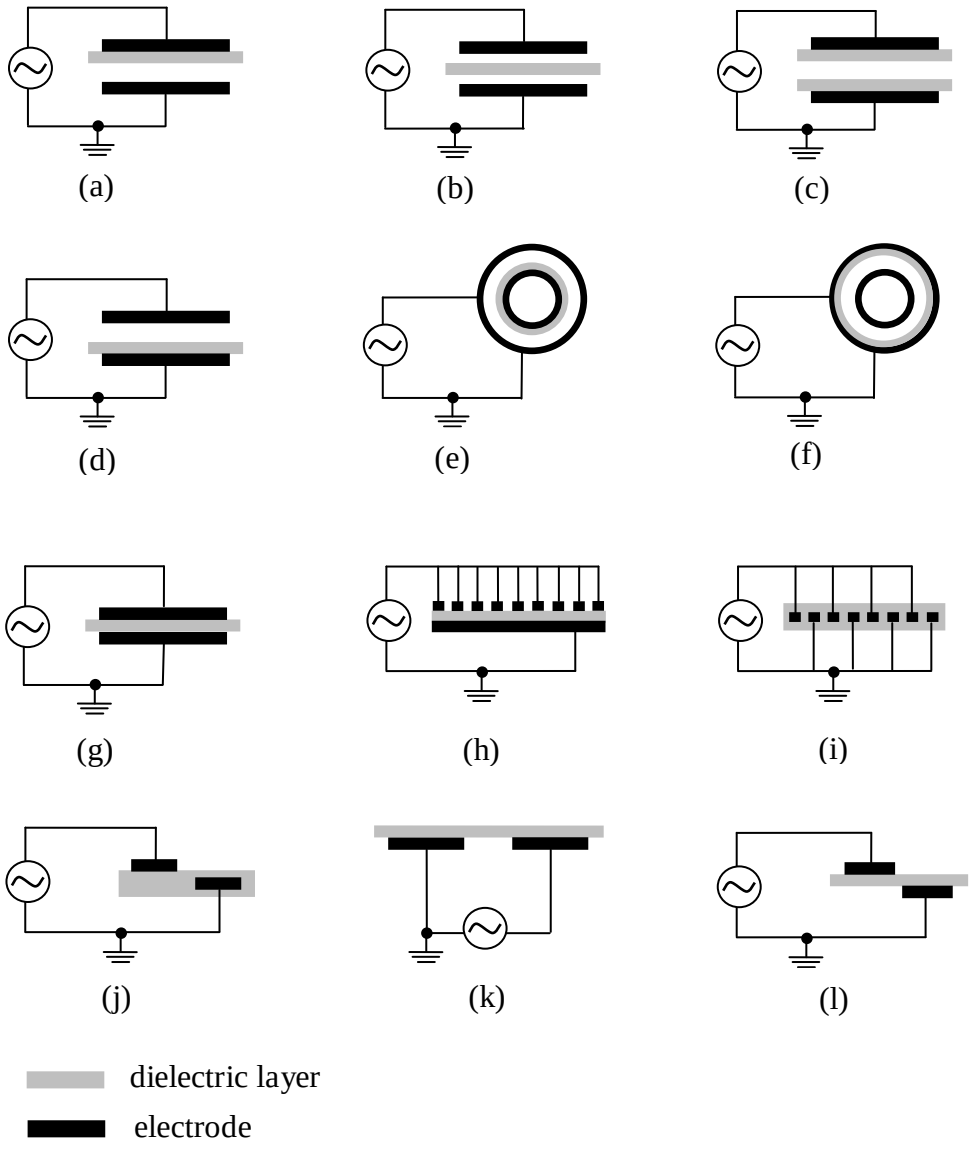


**Figure 2.1.** Numerous volume discharge and surface discharge configurations. (a)-(d) volume discharges, (e)-(f) coplanar discharges, and (g)-(l) surface discharges.

## 2.1.2 Electrical Breakdown Consideration

The breakdown of gases occurs when the potential applied across the electrodes exceeds the threshold value and the neutral gas starts to conduct. The breakdown mechanism of gases usually starts with electron multiplication in cascade ionization when accelerated by electric field. It can be described in a plane parallel plate separated by a distance, *d* as illustrated in Fig. 2.2. The primary electrons near the cathode surface are accelerated by external electric field and drift to the anode. The electrons ionize the background gas by bombarding the neutral atoms or molecules to create ions and free electrons. The electron multiplication produced through ionization along their way from cathode to anode leads to electron avalanche.

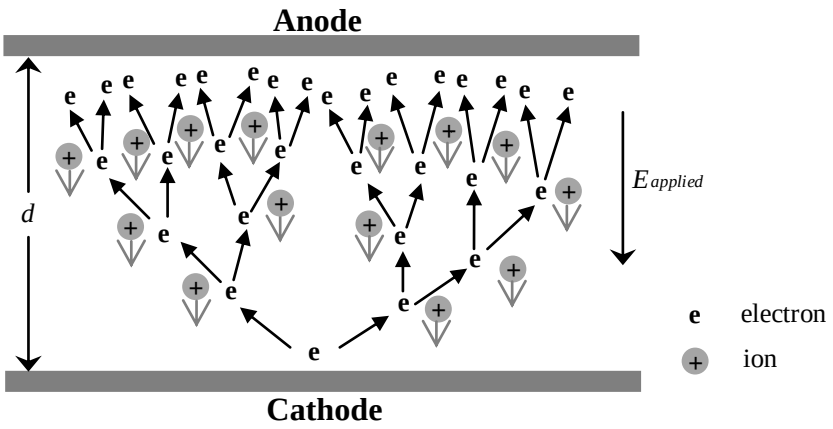


**Figure** 2.2. Illustration of electrical breakdown mechanism between two parallel-plate electrodes.

The threshold value at breakdown is known as breakdown voltage or ignition voltage. This is the maximum voltage applied to the gas to become conductive at the moment of breakdown and large current passes through the gas. This breakdown voltage is governed by Paschen Law, which is a function of the product of gap pressure, *p* and gap width, *d*, usually written as *V=f(pd)* (Townsend, 1910) or *V=f(Nd)*, where *N* is the number density of gases. The former relation is mostly applicable under room

temperature while the latter relation is more common where it depends on the number density and is independent of temperature (Kogelschatz et al.,2005, p.30) .

Lower value of *pd* product where the electron mean free path over the gas gap is high, the breakdown is considered as Townsend breakdown. The time scale of this breakdown is in the range of microseconds. The Townsend breakdown mechanism is not suitable to describe the breakdown mechanism when the electrons mean free path over the gas gap is reduced. This is the situation when the *pd* product is high ($>$ 200 Torr-cm). Due to the high *pd* value, the electronic avalanche is large, which is able to produce sufficient amount of ions, giving rise to a localized space charge field and creates a thin conducting channel across the gap. This kind of breakdown is named streamer breakdown. The time scale of streamer breakdown is in the range of nanoseconds (Massines, Gherardi, Naude, & Segur, 2009). This concept of streamer breakdown mechanism was developed by Raether, Loeb and Meek (as cited in Kogelschatz, 2002).

Massines et al. reported that DBD can be categorized into Townsend breakdown or streamer breakdown. The Townsend breakdown usually leads to homogeneous DBD while the streamer breakdown usually leads to filamentary DBD. However, the connection between the breakdown mechanism and the type of discharge cannot be fulfilled when the discharge is the streamer coupling type (close to homogeneous discharge) (Massines et al., 2009).

The process of the streamer formation involves the initial electron avalanche, followed by the streamer transition and finally the streamer propagation as shown in Fig. 2.3. The electron avalanche is propagating from cathode to anode. During the avalanche, the lighter electrons are moving much faster than the heavy ions, therefore, the electrons are at the head of the avalanche leaving ions at the tail of the avalanche. When the avalanche head reaches the anode, the electrons disappear into the metal

while the ions remain in the gap. Streamer starts to propagate when the avalanche reaches the anode. This streamer is also known as cathode directed streamer and usually moves from anode to cathode. The streamer moves very fast (faster than electron avalanche), reaching the cathode in nanoseconds. The positive charges at the streamers head are attracting additional avalanches while propagating from anode to cathode (Chirokov, Gutsol, & Fridman, 2005).

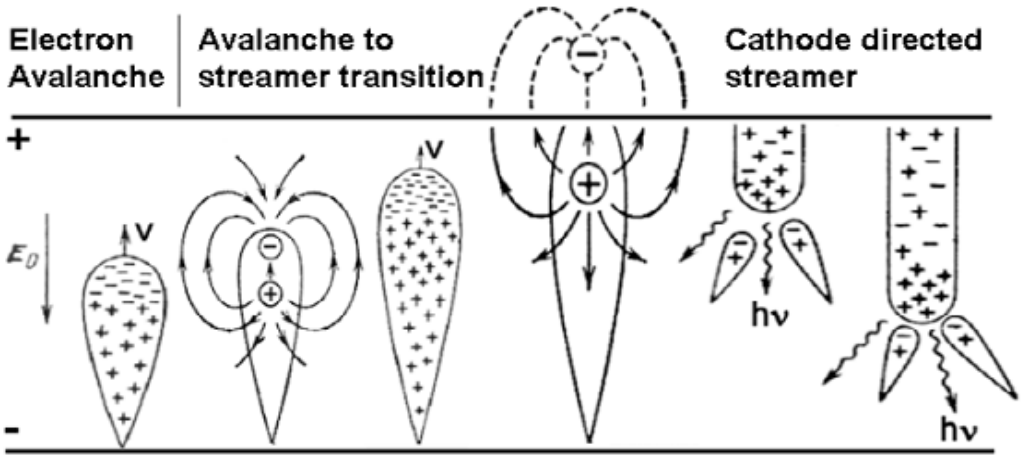


**Figure 2.3.** The process of streamer formation (Chirokov et al., 2005).

In the case of dielectric barrier discharge gap, the streamers tend to hit at the same position each time when the polarity of the applied voltage changes. This phenomenon is due to the memory effect where charges are accumulated during the preceding cycle and remains until the next half cycle. Memory effect in barrier discharge helps to ignite the discharge in the next half cycle at a lower external voltage.

### 2.1.3 Historical Development of DBD Research

The investigations on barrier discharge dates back to more than 1 century ago. The first experimental investigations on ozone production were carried out by Wer Von Siemens in 1857. Siemens found that ozone can be produced when the oxygen or air

flowed through a discharge gap. The discharge setup proposed by Siemens was different from the typical parallel plate setup with the electrode in contact with the discharge. The electrodes were not in contact with the discharge as they were located outside the chamber. Two coaxial glass tubes functioned as the dielectric and the discharges occurred in the annular gap between the glass tubes (as cited in Kogelschatz, 2003).

An effort of characterizing the barrier discharge was made by Buss in 1932. He discovered that the discharge occurred in the form of tiny current filaments between planar parallel electrodes covered by dielectric and took the first photographic image of these current filaments. Current and voltage signals obtained from oscilloscope were documented (as cited in Kogelschatz, 2002; Pappas, 2011). In 1943, Manley showed that the dissipated power of DBD can be obtained by using charge-voltage (*Q*-*V*) Lissajous figures and he derived the useful Manley's equation to calculate the power dissipated per cycle of an ozonator (Manley, 1943).

Further investigations of DBD revealed that DBD occurs in filamentary mode and also glow mode. In filamentary mode, the current filaments are randomly distributed in time and space over the entire dielectric surface. One current filament is about 0.1 mm in diameter and the duration of a current filament is approximately 10-100 ns (Dong et al., 2003). It has been proven that homogeneous glow discharges can be obtained under atmospheric pressure although it is not easy for glow discharges to sustain under this condition. In 1968, Bartnikas reported that spark, pseudo-glow and true glow conditions were observed between two narrow parallel plane electrodes or metallic-dielectric electrodes in helium AC discharge. The term 'pseudo- glow' was used when the glow appearance was observed between the electrodes though discrete pulses were shown in the voltage waveforms (Bartnikas, 1968). Twenty years later, Kanazawa and co-workers revealed favourable conditions for the occurrence of a stable glow discharge at

atmospheric pressure. A continuous glow mode was observed in $CF_4$+$O_2$+He. (Kanazawa, Kogoma, Moriwaki, & Okazaki, 1988)

Under certain conditions, the glow mode is possible to be established at atmospheric pressure. It is also referred to as homogeneous DBD where the discharge is free of current filaments. The current waveform consists of one current pulse for half cycle with longer duration than the current filament obtained from filamentary discharge. The microseconds range of the current pulse in glow mode is a few orders longer than the nanoseconds range of the current filament of filamentary mode (Massines, Segur, Gherardi, Khamphan, & Ricard, 2003). The investigation of stable, non-filamentary appearance of DBD was initiated by Okazaki at al., which opened up better understanding of DBD (Okazaki et al., 1993). They reported conditions required to obtain glow discharge such as Helium being employed as working gas, high frequency source applied (kHz range or radio frequency instead of 50 Hz), grounded plate being insulated by dielectric layer, and brush like high voltage electrode which consisted of 25 stainless steel or tungsten wires was fabricated instead of plate electrode (Kanazawa et al., 1988). Realizing the high cost of using Helium as working gas, the group with Okazaki introduced a new way of generating stable glow discharge in air, oxygen, nitrogen and argon under atmospheric pressure driven by a 50 Hz source a few years later. They proposed a fine wire mesh electrode covered by polyethylene terephthalate (PET) as the dielectric to sustain the glow mode in air, oxygen, nitrogen and argon. They tested on different kind of insulators and proved that not all types of insulators used are able to produce stable glow discharge at atmospheric pressure (Okazaki et al., 1993). Several authors have published their work and reported that uniformity of the discharge is possible by inserting a wire mesh between the electrode and the dielectric barrier which is based on the work of Okazaki (Tepper, Lindmayer, & Salge, 1998; Fang, Qiu, & Luo, 2003). The uniformity of the discharge guaranteed a uniform surface

treatment where the active species created during the discharge are uniformly spread out on the surfaces. The uniform distribution of the active species on the surfaces cannot be realized in filamentary discharge (Massines & Gouda, 1998; Massines, Messaoudi, & Mayoux, 1998).

The observation of current waveform and taking high speed photographs of the discharge is usually carried out to differentiate between the filament discharges and glow discharges. Glow discharge is characterized by only one current peak observed for each of the positive and negative polarity of the voltage waveform. The imaging tool with exposure time of ns is required for taking the photograph of the discharge as the filament develops in some tens of nanoseconds (Massines & Gouda, 1998). Okazaki et al. proposed another method which is the observation of *Q*-*V* Lissajous figure to differentiate between filament discharges and glow discharges. The Lissajous figure appears as a parallelogram if the discharge is in filamentary mode while the Lissajous figure shows only two voltage line (top line and the bottom line of the parallelogram) in glow mode DBD (Okazaki et al., 1993). This method to ascertain the type of discharge is necessary as the observation of the appearance of the discharge can give wrong information.

The detailed study of the discharge physics was carried out by Massines and coworkers at Paul Sabatier University, France and a few approaches to obtain the atmospheric pressure glow discharge (APGD) were proposed (Massines et al., 2009). They included memory effect (trapping of ions from preceding cycle and the creation of long live metastables that remains until the next half cycle), enhancement of secondary electron emission at the cathode surface by ions, photons or excited state species as well as the reduction of gas ionization via Penning ionization to avoid large electronic avalanche leading to filamentary discharge.

Modeling of DBD contributes to enhance the understanding of its discharge properties. It gives new insight of discharge processes which could not be deduced through the measurement from experiment. Most of the publications on the modeling were obtained at the end of $20^{th}$ century due to the lack of advance computer systems hindering the modeling work before that. Two types of DBD models were proposed, a physical model and the other an electrical model. Physical model is used to study the partial movements of charged particles and boundary conditions where fluid equations are applied (Zhang et al., 2010). The first 2-D model to analyze the formation of a microdischarge in a DBD was carried out by Gibalov et al. in 1981 (as cited in Kogelschatz, Eliasson, & Egli, 1999). Two decades later, Gibalov & Pietsch presented a detailed study of the dynamics of DBD which included the temporal and spatial development of a microdischarge in volume discharge and the single discharge step in surface discharge. The dynamics of the charged particles, the development of the discharge on pre-charged surfaces as well as the energy density of the volume and surface discharges were modeled numerically (Gibalov & Pietsch, 2000). Many works involving the numerical analysis of the electrons temperature, distributions of electrons, ions, excited species and neutral particle densities as well as surface charges build up were published by different groups (Braun, Gibalov, & Pietsch, 1992; Jeong, Shin, & Whang, 1999; Sjoberg, Serdyuk, Gubanski, & Leijon, 2003).

Calculations involved in physical models are rather complicated compared to electrical models. Electrical models involve a simple equivalent circuit to study the electrical behaviour of DBD with two capacitances ($C_{air\ gap}$ and $C_{dielectric}$) arranged in series and an equivalent resistance is paired in parallel with air gap capacitance after breakdown. In 2003, Liu & Neiger introduced an electrical model for homogeneous DBD and several equations for internal electrical quantities such as voltage across the gap, internal discharge current and power consumed in the gap were derived. This

model explained in details about different currents found in DBDs and emphasized the true discharge current in the gap is not the same as the measured external current due to the existence of displacement current in the gap (Liu & Neiger, 2003) . An electrical model to study the transition from an atmospheric pressure Townsend discharge to a filamentary discharge was proposed by Naude et al. where two back-to-back Zener diodes were used to model the Townsend breakdown (Naude, Cambronne, Gherardi, & Massines, 2005). Electrical models to study the electrical characteristics of a DBD such as discharge current, charges transported, energy and power deposited in a cycle, breakdown condition and number of pulses under the influence of various operating parameters (frequency, applied voltage, gas flow rate, gap width) were discussed in many other works (Valdivia-Barrientos, Pacheco-Sotelo, Pacheco-Pacheco, Benitez-Read, & Lopez-Callejas, 2006; Jidenko, Petit, & Borra, 2006; Pal et al., 2009; Zhang et al., 2010).

DBD has been gaining the interest of the researchers from all over the world after 1990. This is revealed in the number of publications where it increased from 68 publications in 1997 to about 680 publications in 2009 (Pappas, 2011). From the understanding of the discharge physics and optimization of the discharge parameters to obtain the chemical species in DBD, it has led to several applications. The earliest application is the production of ozone for waste water treatment, disinfection of drinking water and bleaching processes. Large ozone generators consisting of several hundred discharge tubes were built for industrial application. The modern high power ozone generator with higher operating frequency enables the operation at lower voltage ($< 5$kV) and higher power density. Modern technology allows higher production of ozone where several hundred kilograms of ozone is able to be produced in an hour at the power consumption of several megawatts (Eliasson & Kogelschatz, 1991a; Kogelschatz, 2003).

DBD is one of the solutions for pollution control and destruction of poisonous compounds. The poisonous compounds include nitrogen oxides, sulphur oxides obtained from flue gases and volatile organic compounds (VOC) such as hydrocarbons and chrolofluorocarbon, which can lead to the serious pollution in the environment. These compounds can be attacked by radicals, electrons and photons generated from DBD (Kogelschatz et al., 1999). Various research on the removal of $NO_x$, NO, $SO_2$ and VOC produced from the industrial processes and automobiles were carried out by many researches using DBD and was demonstrated that it can be used for pollution control (Chang, 2001; Nagao, Nishida, Yukimura, Kambara, & Maruyama, 2002; Chen & Mathur, 2002; Ma, Chen, Zhang, Lin, & Ruan, 2002; Chae, 2003; Takaki, Shimizu, Mukaigawa, & Fujiwara, 2004; Plaksin, Penkov, Ko, & Lee, 2010).

DBD is also frequently utilized for material processing applications such as surface activation, etching and deposition. Although it has been known for years that low pressure plasma is developed for material processing but due to vacuum operation of the low pressure plasma which requires expensive pumping system, the maintenance cost is comparatively high. When comparing to low pressure plasma, DBD has the potential to scale up to larger size for industrial application with lower cost where no vacuum system is required. Detailed study of the interaction of active species with the surfaces can be found in numerous publications (Salge, 1996; Sonnenfeld et al., 2001; Massines, Gherardi, Fornelli, & Martin, 2005; De Geyter et al., 2009; Fang, Yang, & Qiu, 2010). It is found that the uniformity of the discharge will ensure uniform treatment or coating where energy can be distributed uniformly on the surfaces. Massines et al. showed in their work that uniform or homogeneous treatment of surfaces by atmospheric glow DBD has higher efficiency over the filamentary DBD (Massines et al., 1998).

Recently, DBD has gained popularity in biological and biomedical field. Application of DBD in biological and biomedical field include blood coagulation

(Fridman et al., 2006; Kalghatgi et al., 2007), living tissue sterilization (Fridman et al., 2006), hand disinfection (Morfill, Shimizu, Steffes, & Schmidt, 2009) and bacterial inactivation (Laroussi, Alexeff, & Kang, 2000; Choi et al., 2006; Kostov et al., 2010). It is found that not only are the reactive species responsible for the inactivation of bacteria or sterilization when in contact with living cells, tissues or bacteria, but the charged particles (ions and electrons) are playing important roles when they reach the treated surface (Dobrynin, Fridman, Friedman, & Fridman, 2009). The application of plasma in biological and biomedical field is a more recent development where detailed understanding of the mechanism of the plasma with the living cells and human cells, risk analysis as well as the safety issue needs to be studied.

## 2.2 Development of Plasma Jet

Plasma jet is another type of non-thermal discharge at atmospheric pressure where the area of the discharge is usually smaller than the planar DBD. It was developed after 1990s and it is based on the ideas from corona discharge and dielectric barrier discharge (Kim, Chung, & Bae, 2009). The plasma jets typically consist of a nozzle and the jet expanding into the surrounding when gas is allowed to flow through the nozzle. The plasma jets described in the literatures are different mainly in their electrode arrangement, gas compositions, operating frequency and excitation schemes. Plasma jet is designed in such a way that it can be used to treat small spot and complex geometries as it can penetrate into small cavities, narrow gaps or surfaces which are inaccessible. This is a solution to treat not only the flat and smooth surfaces but also the complicated and uneven surfaces which could not be achieved by the planar DBD configuration.

### 2.2.1 Configurations of Plasma Jet

Numerous plasma jets with different types of configuration have been developed and described in the literatures as shown in Fig. 2.4. Most of the design used capillary tube or a straight tube as the dielectric layer where the flow of the gas is unobstructed to obtain a longer jet.

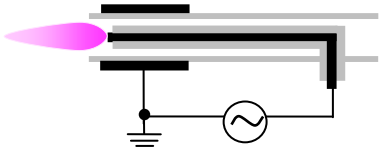

(a)
(Xu, Ma, & Zhang, 2008)

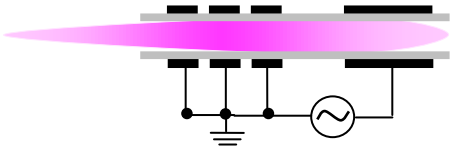

(b)
(Jiang, Ji, & Cao, 2010)

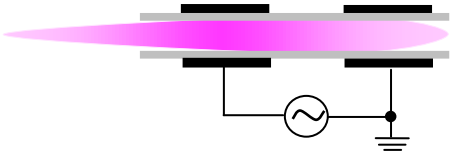

(c)
(Jiang, Ji, & Cao, 2009)

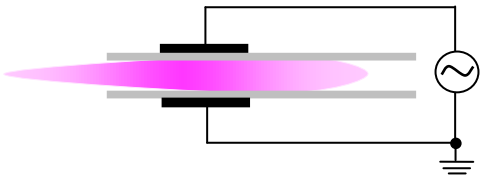

(d)
(Jiang et al., 2009)

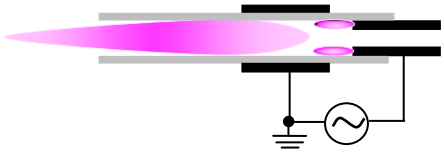

(e)
(Sakamoto, Kikuchi, & Ohyama, 2007)

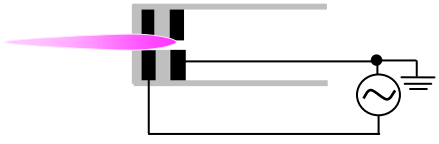

(f)
(Hong & Uhm, 2006)

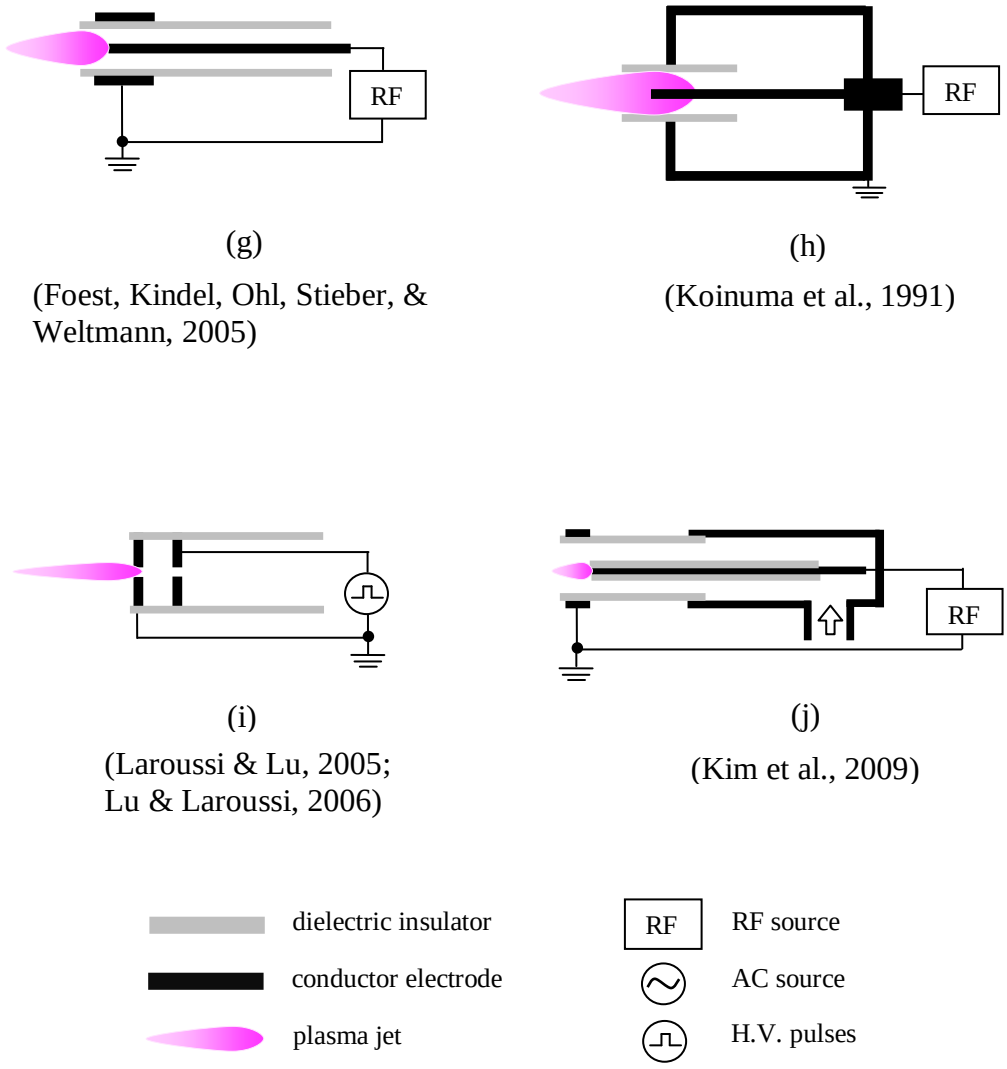


(g)
(Foest, Kindel, Ohl, Stieber, & Weltmann, 2005)

(h)
(Koinuma et al., 1991)

(i)
(Laroussi & Lu, 2005; Lu & Laroussi, 2006)

(j)
(Kim et al., 2009)

**Figure 2.4.** Various configurations of plasma jets at atmospheric pressure.

## 2.2.2 Excitation Schemes of Plasma Jet

Plasma jet can be excited by various excitation schemes such as DC, AC, RF and microwave discharge. The range of the operating frequency of the plasma jet is wide where it can be operated under several tens of kilohertz or up to radio frequency range (Kim et al., 2009). Different names were given to the plasma jet under various excitation schemes such as cold plasma torch, plasma pencil, microwave torch, atmospheric pressure plasma jet, plasma needle and etc.

Many researchers worked with RF as excitation schemes to generate plasma jet at atmospheric pressure. The cold plasma torch (Fig. 2.4(h)) was first demonstrated by Koinuma et al. in 1992 (Koinuma et. al, 1992). It is designed based on DBD arrangement where a quartz tube is inserted between the needle electrode and the grounded electrode. The needle electrode is powered by RF 13.56 MHz power supply.

A uniform low temperature RF atmospheric pressure plasma jet was developed by Jeong et al. for material processing such as etching and deposition (Jeong et al., 1998). This plasma jet consisted of two concentric stainless steel electrodes and does not require a dielectric material between the electrodes. Water was used for cooling purpose. Oxygen was added to the Helium carrier gas for etching organic films while carbon tetrafluoride was added in addition to oxygen for etching silicon dioxide and metal. This plasma device was able to etch the Kapton at the rate of 8.0 μm/min while silicon dioxide, tantalum and tungsten were etched at the rate of 1.5, 2.0 and 1.0 μm/min respectively. Etching result for Kapton showed that singlet delta metastable oxygen and atomic oxygen were probably participating in the etching process. Besides etching, this device has shown its potential in deposition of silicon dioxide films. Mixtures of helium and oxygen gas were flowing into the device and tetraethoxysilane was mixed with the effluent of the jet to deposit silicon dioxide on the silicon substrate. Deposition rate of 3020 Å/min can be achieved at temperature range of 115 to 350 °C, which was comparable to thermally grown silicon dioxide (Babayan et al., 1998).

Janca et al. developed a unipolar high frequency (13.56 MHz) plasma pencil based on hollow cathode configuration (Janca, Klima, Slavicek, & Zajickova, 1999). A hollow needle or hollow cylinder acts as the cathode and is inserted in a quartz capillary. Gas flows in the hollow electrode and the quartz capillary. Jet is formed in the hollow electrode and outside of the nozzle. This plasma pencil was applied on various plasma

chemical technologies, restoration of archeological glass artifacts as well as to reduce the corrosion products on historical metal artifacts.

Another design of plasma jet similar to the unipolar high frequency plasma pencil was demonstrated by Hubicka et al. in 2002 (Hubicka et al., 2002). It is called RF barrier torch discharge. They have proven that by adding a dielectric at the electrode, the overheating and melting of the nozzle can be avoided. It was shown that the multi torch barrier discharges comprising of nine nozzles is possible and the discharge channels remained stable. This multi plasma jet source was able to interact with the PVC substrate without heating the substrate, avoiding damages to the surface. It was shown that this barrier torch is a promising tool for treatment of thermally sensitive surfaces.

Kim et al. have demonstrated a RF plasma jet at atmospheric pressure. They have proposed a method to improve the plasma reactivity by attaching a grounded copper ring at the outer wall of glass tube as shown in Fig. 2.4(j). The radius of the jet became thicker while the amplitude of the discharge current and the intensity of the optical emission were enhanced significantly (Kim et al., 2009).

Plasma jet can also be generated by using microwave power source. The name such as microwave torch discharge, microwave plasma jet or microwave plasma torch were given to the system and it is usually driven by coaxial line or waveguide based microwave power where impedance matching is required. A microwave plasma torch with the name axial injection torch (TIA) was developed by Moisan et al. in 1994 (Moisan, Sauve, Zakrzewski, & Hubert, 1994). The gas flows within the inner conductor and exits through a nozzle at its conical tip. Due to the axial injection design, a denser torch can be generated. They focused on the study of the electrodynamic of the torch which was related to the impedance matching of their system and the power flow within the system which has not been published during that time.

Due to the complicated design of TIA where its construction required expensive workmanship, Moisan et al. modified the microwave torch to a simple and compact one-nozzle unit torch with the name TIAGO few years later (Moisan, Zakrzewski, & Rostaing, 2001). A microwave torch discharge based on the design of TIAGO was developed by Jasinski et al. in 2002 (Jasinski, Mizeraczyk, Zakrzewski, Ohkubo, & Chang, 2002). It is named Microwave Torch Discharge (MTD). A quartz tube was attached around the nozzle to reduce the interaction of the plasma flame with the surrounding and a metal grid was placed coaxially around the nozzle to protect the personnel and instrumentation from electromagnetic radiation which was not implemented in TIAGO. The stability of the $N_2$ MTD was improved by attaching the grid around the nozzle and it was employed for the destruction of Freon CFC-11. CFC-11 can be highly decomposed at moderate power with $N_2$ as carrier gas to prevent the production of hazardous oxygen compounds.

Anghel & Simon proposed a simple one electrode plasma source sustained by a DC supply voltage lower than 10 V. The thin copper wire with 0.15 mm diameter was inserted into the plasma torch which represented the plasma sustaining electrode and the discharge was sustained in He, Ar and open air. They have shown that the DC plasma torch with He as feed gas was safe to touch by bare hand without electrical shock. The temperature of the He plasma torch was 55 °C, measured at a distance 1.5 mm from the electrode tip (Anghel & Simon, 2007).

Dudek et al. used a DC excitation scheme to generate plasma jet operated in a glow regime at atmospheric pressure. It is called DC powered atmospheric pressure plasma jet source (DC-APPJS). It consisted of a cathode pin where it was inserted into an acrylic tube and a conical cylinder acted as the anode. The gas temperature in the active plasma zone (near the cathode tip) is relatively high, up to 950 K compared to the lower

temperature in the effluent flow (a few millimeters from the cathode tip) which is lower than 350 K (Dudek, Bibinov, Engemann, & Awakowicz, 2007).

Another design which consisted of a single electrode plasma jet device driven by a sub-microsecond pulsed DC voltage was introduced by Lu et al. (Lu et al., 2008). The length of the Helium plasma plume created was up to 4 cm long, which can be adjusted by the gas flow rate and applied voltages. The gas temperature of the plume is near to room temperature although the plume carried a peak current up to 360 mA. The reactive oxygen species (O, $O_3$, metastable state $O_2$) were found to have significant role in bacterial inactivation compared to the excited $N_2$*, $N_2^+$*, He* and UV which exerted no significant direct effect on the inactivation process. The electric field created along the plume was extremely low, hence, its effect on the inactivation process can be ignored. With the same device, Lu and coworkers carried out an experiment to study the behaviour of the plasma bullet where the plumes are not a continuous volume of plasma but rather in a bullet form. In their study, a glass tube was placed in front of the syringe nozzle at a distance from a few millimeters to a few centimeters. It is found that when the bullet traveled from the nozzle to the wall of the glass tube, the luminance of the bullet decreases upon reaching the wall of the tube and after about 200 ns, the secondary plume was ignited in the glass tube. This phenomenon might be due to the local electric field which was created by the charges deposited on wall of the glass tube (Lu et al., 2009).

Recently, a touchable pulsed air plasma plume which was driven by DC power supply was reported. The plume was generated when a counter electrode, e.g. finger was placed near to the needle tip. The temperature of plasma plume varies with the type of working gas being used and it is usually higher than room temperature when ambient air is employed. However, plasma plume presented in this work was able to operate in ambient air while the gas temperature remained at room temperature. The plume can be

touched by human body directly without feeling the heat or electric shock. The current pulse that lasted for short period (pulse width of about 100 ns) resulted in the non-thermal behavior of the plume. Preliminary inactivation results showed that this device can be used for root canal treatment (Wu, Lu, Xiong, & Pan, 2010).

Several plasma jets with AC power have been developed besides the aforementioned RF, microwave and DC plasma jets. Chen et al. designed an atmospheric pressure glow discharge plume (APGD-p) by using an AC power source with maximum peak voltage of 30 kV. The copper rod acted as the powered electrode while the potassium chloride (KCI) solution in the outer layer of the device acted as the counter electrode. The conductive liquid in the outer layer helped to cool the device, resulting in lower power consumption, increase in the duration of operation as well as produced more uniform discharge. They studied the effect of downstream gases of the plume on the dye wastewater. The treatment result showed that the downstream gases of air and $O_2$ exerted significant effect on the degradation of the dye where the dye solution with violet color disappeared entirely (Chen et al., 2006).

A 11 cm long cold plasma plume driven by a 40 kHz AC high voltage was developed in 2008. This was the longest plume expanding into the surrounding air ever reported. This device is suitable for the application in plasma medicine due to its ability to generate active species, operation under atmospheric air, hand held, low gas temperature without arcing and safe to be touched by human with no harm (Lu et al., 2008).

Jiang et al. studied the behaviour of the atmospheric pressure plasma jet and the mechanism of jet formation by using three different types of electrode configuration under AC excitation scheme. They have successfully shown that the jet can be formed in the upstream and downstream regions of a capillary tube at a reduced voltage

(compared to the conventional double electrodes DBD arrangement) even when the grounded electrode was removed (Jiang et al., 2009).

Chiang et al. proposed a parallel plate DBD atmospheric pressure plasma jet which was powered by a distorted AC power supply. They used the plasma jet created for the inactivation of *E.Coli* and *B.Subtilis*. The results had proven that the post-discharge jet region was able to inactivate the bacterial cells efficiently by compressed-air plasma jet or oxygen plasma jet but not nitrogen plasma jet (Chiang et al., 2010).

Another type of plasma jet device comprised of a syringe needle which was inserted into a glass tube was reported recently. This device was driven by a DC-AC inverter where the DC voltage of 0-50 V can be adjusted to obtain the AC voltage up to 5 kV. The characteristics of the plume were investigated based on the different arrangement of the ground electrode. When the ground electrode was placed at the outer wall of the glass tube, the plume can be operated at lower voltage and current compared to the arrangement when there is no ground electrode attached or with a floating electrode. This feature is an advantage for applications in biomedical field where the damage of the living tissue through burning or electric shock can be prevented (Cho et al., 2011).

The non-thermal plasma jets reviewed in the preceding sections are configured with unobstructed gas flow at atmospheric pressure under various excitation schemes. Some of the jets could extend quite far (up to 11 cm) into ambient air. What happens when the flow is obstructed? The answer to this forms the main objective for this research project, to investigate the influence of obstructed gas flows on the behaviour of plasma jet. These are presented in Chapter 4.

## 2.3 Applications of Plasma Jet

Plasma jets are utilized in various applications based on their excitation schemes, temperature, configurations and operating conditions. As discussed in the preceding

section, the atmospheric pressure plasma jet shows great potential in material processing of various materials, including surface treatment, surface cleaning, etching (Jeong et al., 1999) and deposition (Babayan et al., 2001; Benedikt, Focke, Yanguas-Gil, & Von Keudell, 2006). Besides that, the atmospheric plasma jets have been employed in various biological and biomedical applications. Various works on the plasma interaction with biological cells were carried out by Laroussi since year 2000 (Laroussi, 2002, 2009; Laroussi & Lu, 2005). The application of plasma jet on biomedical field is a new approach after the biological application. Stoffels et al. has used the plasma jet for wide range of biomedical applications, including treatment of living cells, and tissue (Stoffels, Kieft, & Sladek, 2003; Stoffels et al., 2006) as well as its ability to sterilize dental tissues (Sladek, Stoffels, Walraven, Tielbeek, & Koolhoven, 2004). However, it is a great challenge where a few potential risk factors need to be considered such as the temperature of the gas, power transferred to the target, UV radiation and the production of toxic gases which could be harmful to the patient (Weltmann & von Woedtke, 2011).

In this project, we will focus on surface treatment and the DBD jet for surface treatment which will be discussed in Chapter 5. The low temperature behaviour of the plasma jet makes it possible to be applied on thermally sensitive substrates. The discharge is expelled through the nozzle and onto the substrate where the substrate is not affected by the electric field formed in the discharge area. Thus, the discharge is safe to be applied on metal surface or electrically sensitive substrate besides the commonly used non-conductive substrate. Plasma jet can be the replacement of planar DBD for material processing to treat surfaces with complicated shapes, non-flat surfaces and even micro cavities (Weltmann et al., 2010).

Polymer is usually chosen for the study of surface treatment as it is known for its low surface energy which is a disadvantage in industrial uses and a solution is needed to solve this problem. The low surface energy due to the presence of weak cohesion layer

at the polymer surfaces leads to poor surface wetting, hence, poor in adhesion to other materials. To solve this, pre-treatment is required to increase the surface energy of the surfaces before printing, painting or coating to promote higher degree of adhesion. There are many ways to improve the surface wetting, such as chemical processing, thermal processing, mechanical processing, and plasma processing. Each of these methods has its own advantages. The application of cold plasmas on surface activation is receiving growing attention in recent years as it is able to generate highly reactive species which is capable to initiate the chemical reactions after reactive species bombardment on the surfaces. This method only changes the uppermost atomic layers of the polymer surfaces without affecting the bulk property (Poll, Schladitz, & Schreiter, 2001). Besides that, plasma based treatment is environmentally friendly process without waste production, which can be harmful to the environment (Yip, Chan, Sin, & Lau, 2002).

In 1993, Okazaki & Kogoma used the downstream plasma which was created through the sharp edges of a metal tube outlet to treat polyethylene film. It was reported that the wettability of the treated film by helium discharge did not change over a period of six months in the air which was much longer than the treatment of plastic film by corona discharge. However, detailed study of the mechanism of surface wetting was not performed (Okazaki & Kogoma, 1993).

Kim et al. used a 30 mm length plasma jet generated in air with mixed gases of $N_2$:$O_2$ (4:1) to treat the stainless steel substrates. The stainless steel surface became hydrophilic after treatment. The optimum surface energy calculated from the contact angle measurement was determined to be at the distance 10 mm from the nozzle and with the nozzle moving velocity of 5 mm/s. Placing the substrates too near to the nozzle (< 10mm) will cause damage to the substrates due to arc generated at the end of the nozzle tip. They mentioned that the increase of the surface energy is mainly due to the

effect of sputtering by Nitrogen atom and surface oxidation by Oxygen atom (Kim et al., 2002). It is important to determine the distance between the substrate and the nozzle in order to minimize the thermal damage especially dealing with heat sensitive materials (Sarani, Nikiforov, De Geyter, Morent, & Leys, 2011). Similar work on surface treatment by cold plasma jet on metal surfaces was carried out by Toshifuji et al. and results showed that the wettability of the metal surfaces were improved without any damage by plasma torch jet compared to the serious damage of the substrate with arc-spot when the substrate was irradiated by a bipolar pulsed power gliding arc (Toshifuji, Katsumata, Takikawa, Sakakibara, & Shimizu, 2002).

In another work, the surface treatment was performed on textile structure by a commercial RF atmospheric pressure plasma jet in helium/oxygen gas to study the effect of treatment time on the penetration depth of the treated surface. Four layers of woven polyester fabrics were glued together at their edges to avoid plasma penetration through the edges. The increase of the content of O 1s and the decrease of the content C 1s shown by the XPS analysis suggested that oxygen was incorporated on the treated surfaces of all the layers of the fabrics treated by plasma jet. The oxygen content lead to the formation of oxygen containing polar functional groups on the treated surfaces, resulting in a change of the property of the fabric surfaces from hydrophobicity to hydrophilicity. The improved wettability of the top and bottom sides of each fabric layer suggested that the active species can penetrate into the fabric layers through the pores in the fabric. The effectiveness of the penetration effect reduced when the fabric layers increased and a maximum penetration depth of six layers was predicted by an empirical model in their study (Wang, Liu, Xu, Ren, & Qiu, 2008).

A radio frequency Argon cold plasma jet with the nozzle diameter of 0.8 mm was designed by Ionita et al. for surface treatment. The plasma source was mounted on a motorized scanning stage where its movement (x-y coordinate) was controlled by a

computer. The substrates used were PET, PE, PTFE foils and they were scanned over 10 mm x 10 mm area. The contact angle decreases significantly from 83° to 47° for PET and from 92° to 52° for PE after only 5 scans or treatment duration of 1 s/mm$^{2.}$ The roughening of the polymers surface when the treatment duration was increased can be observed through the investigation of surface topology. The AFM images of PET surface before treatment and after treatment are shown in Fig. 2.5 while the AFM images of treated PE and PTFE after 500 scans of treatment are shown in Fig. 2.6. The surface roughening was due to the etching of polymer surface by reactive species (Ionita, Ionita, Stancu, Teodorescu, & Dinescu, 2009).

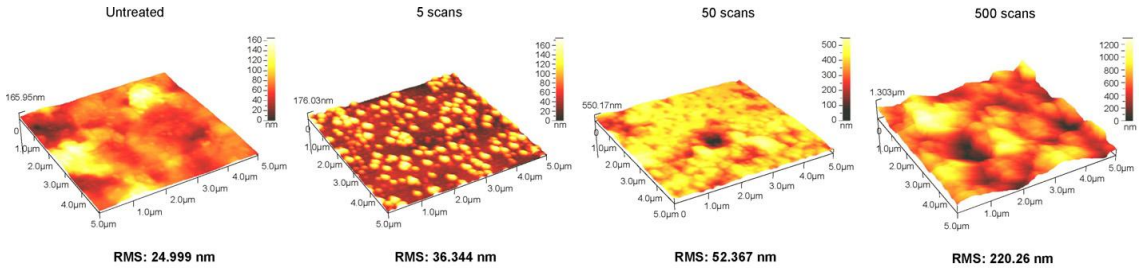


**Figure 2.5.** AFM images of PET substrate before and after treatment with 5 scans, 50 scans and 500 scans.

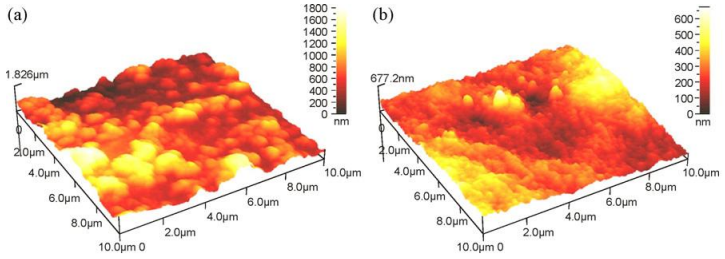


**Figure 2.6.** AFM images of treated (a) PE substrate and (b) PTFE substrate after 500 scans.

The area which can be treated by a single plasma jet is small and it is not suitable for large scale treatment. Cao et al. proposed a solution to arrange the jets in arrays, for the treatment of larger surface area to become possible. They proposed a ten-jet array

housed in an acrylic case with individual ballast and gas feed, which is capable of treating massive three dimensional surfaces. The width of this device, measured from the first to the last jet is 3.2 cm. The interesting part of this work is that by using a screwdriver and a surgical tissue forceps as the downstream ground electrode, the jet can be ignited at different nozzle-to-forceps and nozzle-to-screwdriver distances. To confirm the jet is able to treat 3-D surfaces, they replaced the metal substrate with a 10° sloped PVC substrate, the result showed all ten jets were able to ignite at different nozzle-to-substrate distances. They explained that this might be due to the self-adjustment mechanism among the individual jets and also the spatial redistribution of the surface charges on the acrylic case. The processing time can be reduced when the jet is arranged in arrays for surface treatment (Cao, Walsh, & Kong, 2009).

However, one of the drawbacks of surface treatment by plasma sources is the ageing effect of the treated surface where the hydrophobic recovery over time is observed. The recovery process depends on treatment parameters, the environment as well as the storage temperature. According to Chan et al., the rate of ageing can be reduced in two ways. One way is to increase the crystallinity of the surface which hinders the mobility of the polymer chains due to orderly packed structure, resulting in slower ageing. Another way is to introduce higher degree of cross-linking surfaces which limits the movement of polymer chains, thus, reducing the ageing effect (Chan, Ko, & Hiraoka, 1996). Banik et al. carried out an experiment to study the influence of crystallinity on the ageing effect by using high density polyethylene with different degrees of crystallinities. The increase of crystalline surface can be achieved by annealing the substrate at various temperatures and duration. Their study had shown that the ageing effect on the treated surface was slower in the surface with higher degree of crystallinity (Banik et al., 2003). Another work by Kim et al. to study the ageing effect on the low density polyethylene films with different crystallinity showed similar results where the

hydrophobic recovery of treated films with higher crystallinity was lower. (Kim, Ryu, Park, Sur, & Park, 2003).

# CHAPTER 3

## Experimental Setup

### 3.1 DBD Jet System

#### 3.1.1 Configuration of DBD Jet

The dielectric barrier discharge jet (DBD jet) was designed and constructed based on DBD configuration with one of the electrode insulated by dielectric material as depicted in Fig. 3.1. The DBD jet consisted of a hemispherical electrode, end plate electrode and borosilicate glass test tube. Both the hemispherical electrode and end plate are made from copper. The end plate is 50 mm in diameter and the thickness is 0.5 mm. A 1.0 mm hole is drilled at the center of the end plate (which is usually electrically grounded) to enable the jet formation outside the electrode.

In this setup, the dielectric barrier used is a 75 mm long Borosilicate glass test tube of internal diameter 10 mm and wall thickness of 1.0 mm. The hemispherical electrode is inserted into this glass test tube until the hemispherical surface touches the inner wall of the rounded end of the tube. The hemispherical electrode and the inner wall of the glass tube need to be cleaned with alcohol from time to time as the green deposit that forms on the surface of the hemispherical electrode after some time of operation will interrupt the discharge. This green deposit is due to the reaction of copper with moisture in the air forming hydrated copper carbonate (Corrosionist, n.d.). Thus, the discharge can lose its stability if operated for more than 3 minutes continuously especially in Ar. The test tube is held coaxially in a Teflon cylinder of inner diameter 30.6 mm and wall

thickness 4.3 mm. The internal length of this Teflon housing is 58 mm when the gap between the end of the test tube and the end electrode plate is set at 0.5 mm.

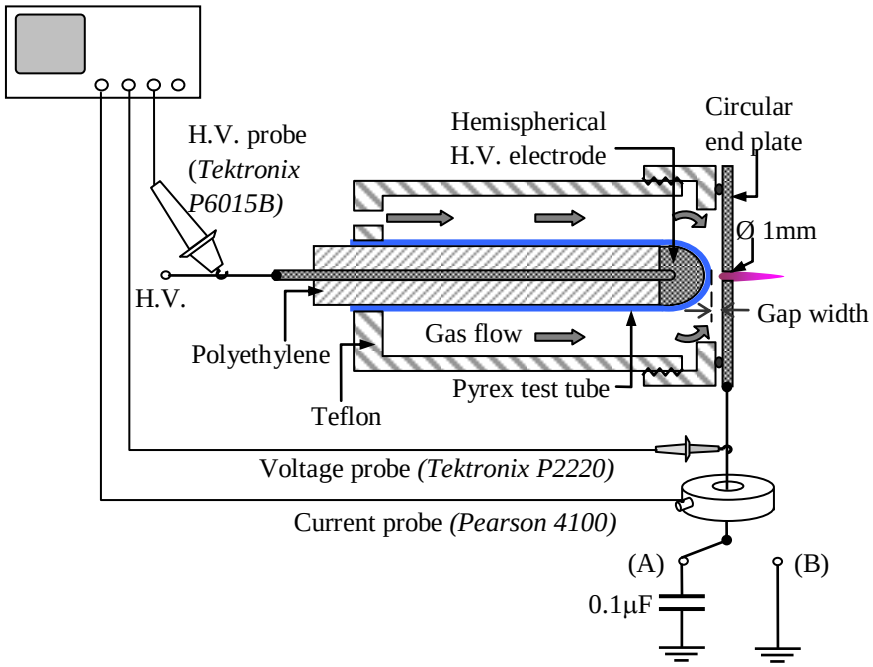


**Figure 3.1.** Schematic of the DBD jet.

### 3.1.2 H.V. Source

A home built power supply is used to power the DBD jet and the schematic is presented in Fig 3.2. The output voltage is stepped up by a car ignition transformer which is driven by a MOSFET and is able to deliver sinusoidal voltages up to 23 kV peak-to-peak (p-p) and frequency up to 12 kHz. The voltage to the drain terminal of MOSFET is supplied by the variable voltage regulator and the amplitude of the H.V. sinusoidal output can be controlled. The frequency is adjusted by a 555 timer with continuous square pulses of amplitude about 11 V. This voltage is supplied by a 12 Vdc regulator that drives the timer.

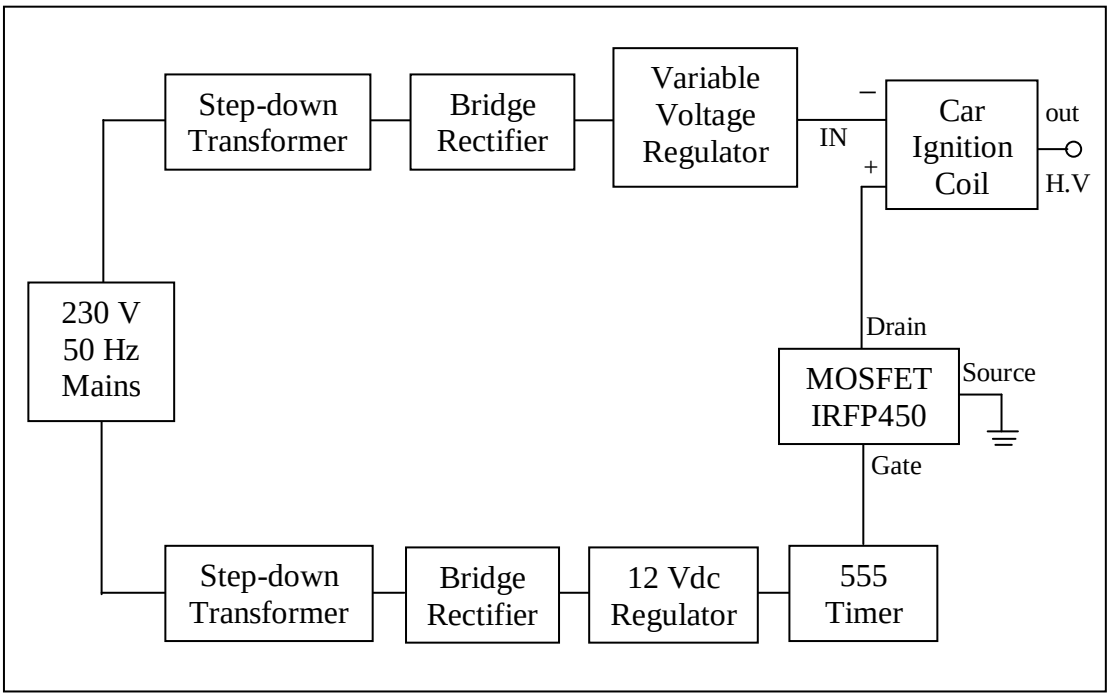


**Figure 3.2.** Schematic circuit of H.V. source

### 3.1.3 Gas Flow System

The DBD jet system operates under atmospheric pressure. Different types of gas were employed in this study, namely Argon (Ar), Nitrogen ($N_2$) and mixture of Argon and Nitrogen (Ar:$N_2$). The gases were controlled using a mechanical flow meter and flowed continuously into the chamber as shown in the schematic of Fig. 3.3.

A variable area flow meter (Dwyer RMA-21-SSV) as shown in Fig. 3.4 was used to control and read the rate of gas flow. This flow meter can be used at pressure up to 100 psi or 6.89 bar and temperatures up to 54 °C. The flow rate has to be increased slowly especially at high flow rates to avoid the float from getting stuck when it reaches highest mechanical position. The observed readings from the flow meter scale have to be corrected as it is dependent on outlet pressure, temperature and density of the medium. To determine the actual gas pressure at the outlet, a Bourdon Tube Pressure Gauge (WIKA 212.53.63) was fixed between the exit of the flow meter and the inlet to

Teflon DBD chamber. With the recorded pressure readings, the correction factor for pressure and temperature, $K_{T\&P}$ can be calculated based on equation (3.1).

$$K_{T\&P} = \sqrt{\frac{p_1 \, x \, T_2}{p_2 \, x \, T_1}}$$

$$= \sqrt{\frac{(14.7 + gauge\ pressure) \, x \, 294}{14.7 \, x \, (273 + temp.\ in\ °C)}} \qquad (3.1)$$

where

$P_1$ = Actual gas pressure (14.7 psia + gauge pressure), measured at outlet

$P_2$ = Standard gas pressure (14.7 psia) ≡ 0 psig

$T_1$ = Actual temperature (273 K + temperature °C)

$T_2$ = Standard temperature (294 K), equivalent to 21 °C

Two types of gases, purified $N_2$ and purified Ar (both of 99.999% purity), and their mixture were made to flow into the DBD chamber. Both of the pure gases have different gas density, hence, besides the correction for pressure and temperature, the actual gas flow rate needs to be corrected by multiplying a correction factor for density. The correction factor is 1.01 and 0.895 for $N_2$ and Ar respectively and the corrected flow rate for $N_2$ and Ar can be calculated as shown in equations (3.2) and (3.3).

$$Q_2 = Q_1 \text{ x } K_{T\&P} \text{ x } \sqrt{\frac{D_{Air}}{D_{N2}}} \qquad (3.2)$$

$$Q_2 = Q_1 \text{ x } K_{T\&P} \text{ x } \sqrt{\frac{D_{Air}}{D_{Ar}}} \qquad (3.3)$$

where

$Q_1$ = Observed reading

$Q_2$ = Actual flow corrected for pressure, temperature and density

$D_{Air}$ = Density of air = 1.161 $kgm^{-3}$ at 300 K (27°C)

$D_{N2}$ = Density of Nitrogen = 1.145 $kgm^{-3}$ at 300 K (27°C)

$D_{Ar}$ = Density of Argon = 1.449 $kgm^{-3}$ at 300 K (27°C) (The Physics Hypertextbook, n.d.)

The corrected reading for gas density, pressure and temperature at the rates ranging from 1-9 litre per minute (LPM) as read from the flow meter reading for $N_2$, Ar and $N_2$:Ar is depicted in Fig. 3.5.

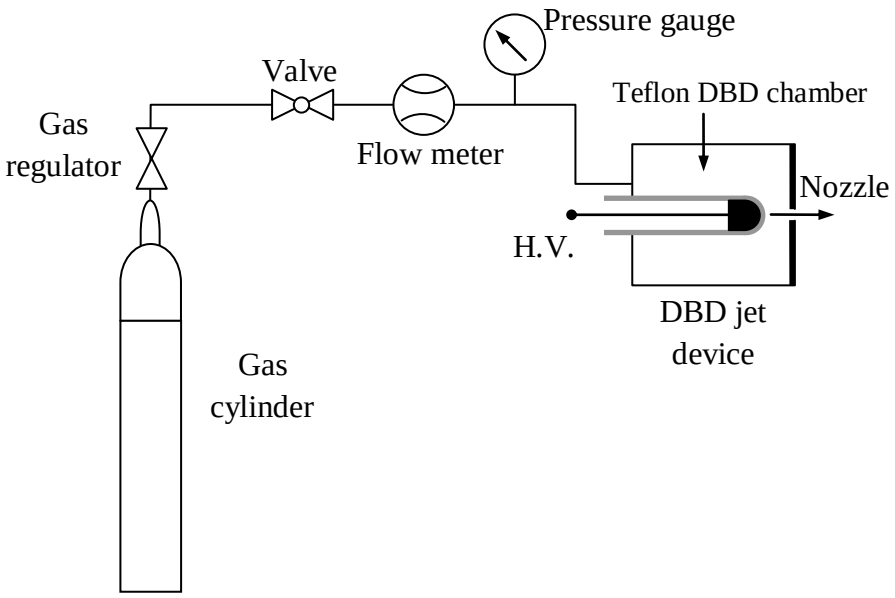


**Figure 3.3.** Schematic of gas flow system

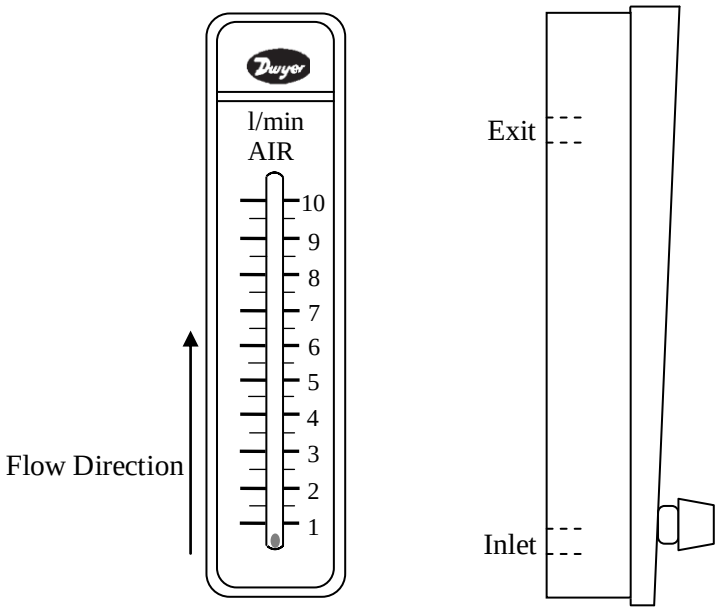


**Figure 3.4.** Figure of flowmeter

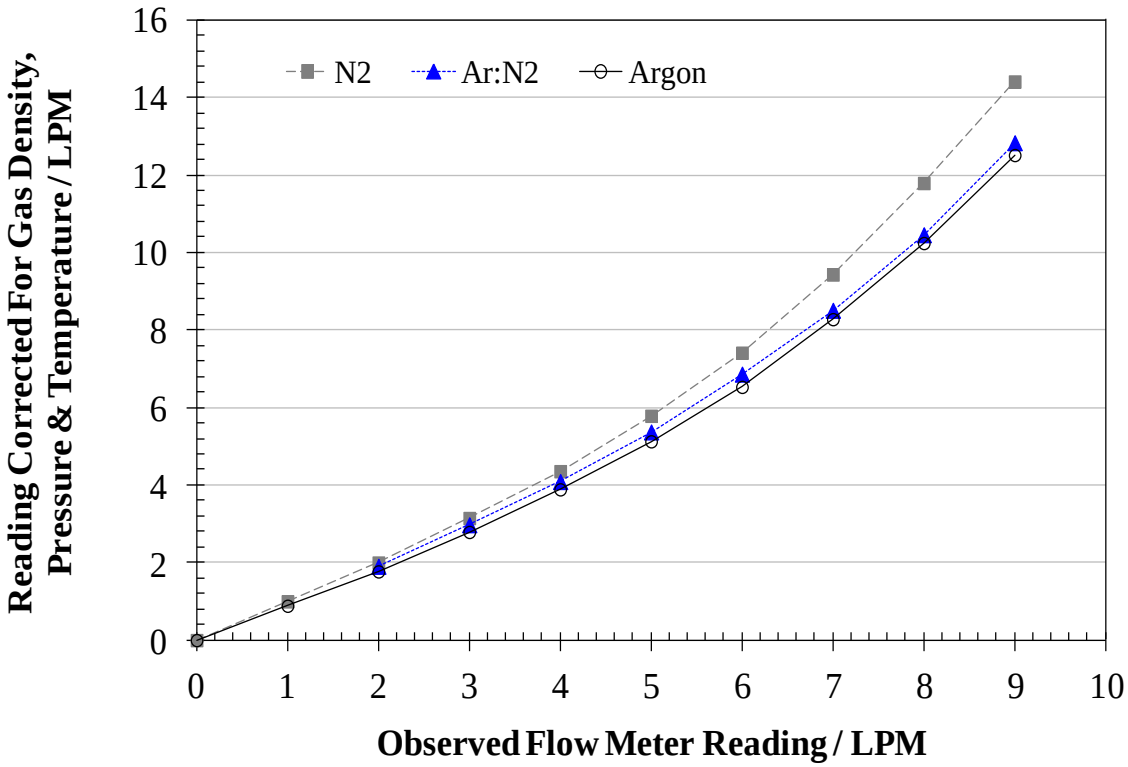


**Figure 3.5.** The corrected reading for $N_2$, Ar and $N_2$:Ar.

A simple estimate of the velocity of the flow at the nozzle is determined from the following expression:

$$V_{Nozzle} = \frac{Q_2}{A}$$

where $Q_2$ = Actual flow corrected for pressure, temperature and density ($m^3s^{-1}$)

$A$ = cross sectional area of the nozzle with 1 mm diameter ($m^2$)

It has been assumed that the pressure measured just before the inlet to the Teflon chamber is the same as the pressure built-up in the chamber due to flow constriction at the nozzle. The estimated value of the flow velocity against corrected flow is given in Fig. 3.6. The flow velocity increases linearly with increase in gas flow rate. The gas flowing out through the nozzle attains subsonic speed at high flow rate (taking the speed of sound in air at 300 K to be 347 $ms^{-1}$).

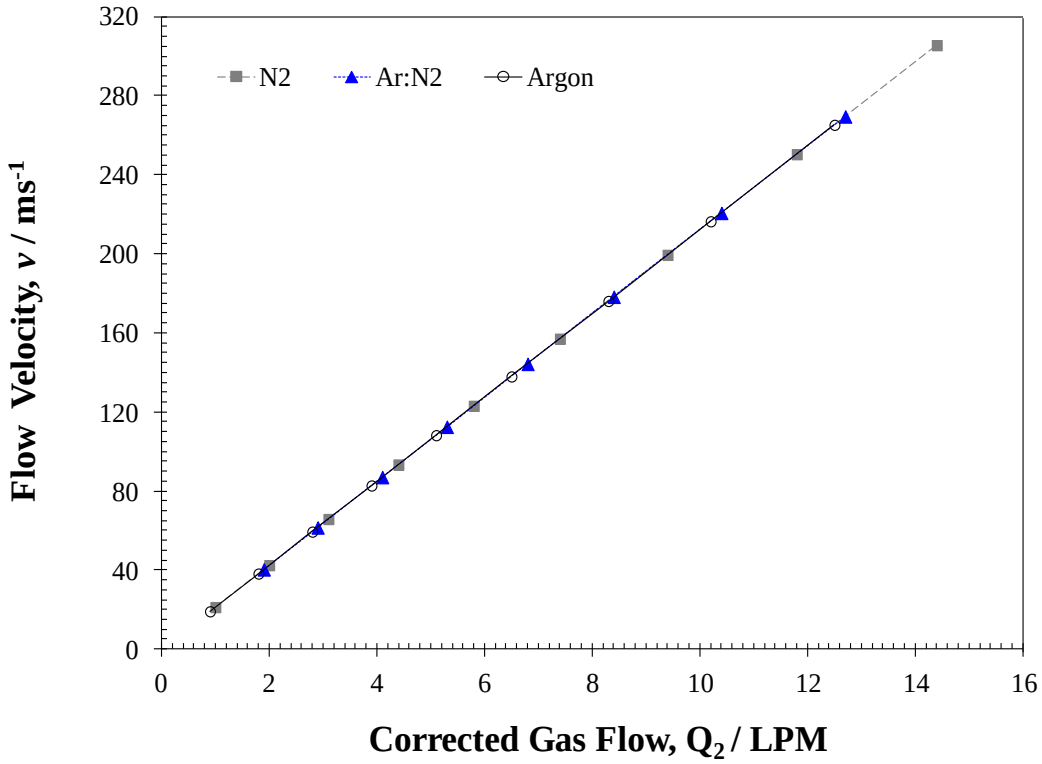


**Figure 3.6.** Variation of the estimated flow velocity at the nozzle versus corrected gas flow rate.

## 3.2 Electrical Diagnostics

The electrical behaviour of DBD jet to be investigated includes the behaviour of the voltage and current signals of the discharge, the amount of charge transferred in the discharge and by the jet.

### 3.2.1 Current and Voltage Measurement

As shown in Fig. 3.1, the high voltage is monitored by a Tektronix high voltage probe (1000:1) model P6015B while the low voltage by Tektronix P2220 probe (10:1). The high voltage probe is able to measure DC voltage up to 20 kV and AC peak-to-peak voltage up to 40 kV. The current is measured by enclosing the current carrying conductor with a Current Transformer (Pearson Model 4100) of sensitivity of 1 V/A and output resistance of 50 ohms. The maximum peak current and maximum RMS current

allowed for this current monitor are 500 A and 5 A respectively with usable rise time of 10 ns. The dimensions of this current monitor are shown in Fig. 3.7. The measurements obtained were acquired by a 200 MHz and 2 GS/s four channel digital storage oscilloscope (Tektronix TDS 2024B). Data can be saved using a USB flash drive through the oscilloscope USB port or by connecting the computer to the oscilloscope and capturing the waveform data via Tektronix Open Choice Desktop interface.

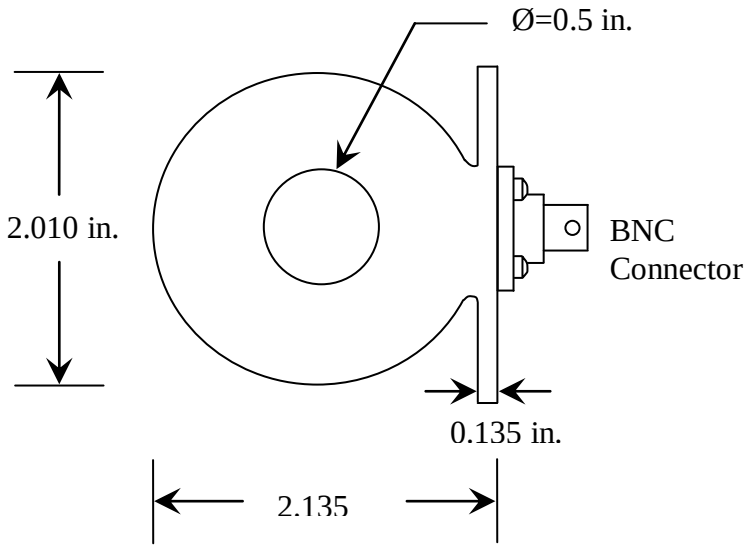


**Figure 3.7.** Dimensions of the Pearson Current Monitor (Model 4100).

### 3.2.2 *Q-V* Measurement

The charges, power dissipated and energy deposited in the DBD can be determined by connecting a capacitor of much larger capacitance (0.1 μF) value than the DBD device (picofarad range) in series to the end electrode (connection marked (A) in the arrangement in Fig. 3.1). A typical *Q-V* Lissajous plot for the DBD is shown in Fig. 3.8. *V* is the applied voltage, and *Q* is the charge measured across the series capacitor, calculated by multiplying its capacitance value with the voltage drop across the series capacitor. From this Lissajous plot, the charge transferred (*Q*), energy deposited per cycle (*E*), mean power dissipated per cycle (*P*), breakdown voltage ($V_b$), capacitance of

dielectric ($C_d$) and capacitance of air gap ($C_g$) can be determined (Manley, 1943; Falkenstein & Coogan, 1997). When no discharge occurs in the air gap, the *Q*-*V* Lissajous plot shows a straight line intercepting the origin and its slope gives the total capacitance, $C_T$ of the system as shown in Fig. 3.9. When the DBD is ignited, the straight line intercepting the origin will change into a parallelogram (Fig. 3.8). The charge transferred per half cycle, $\Delta Q_{1/2}$ was measured directly from the two extremes (BC or DA) of the charge axis of the parallelogram while the mean energy, *E* deposited into the discharge per cycle was calculated from the enclosed area of *Q*-*V* Lissajous parallelogram. The mean power dissipated in the discharge, *P* can be calculated by multiplying the working frequency, *f* with *E*. The slope of the discharge regions (BC, DA) gives $C_d$ while the slope of the non-discharge regions (AB, CD) gives the total capacitance, $C_T$ of the device. The measurement of $C_d$ from *Q*-*V* Lissajous parallelogram is useful when the geometry of electrode is complicated. $C_g$ is determined from the series capacitance relation, $C_T^{-1} = C_d^{-1} + C_g^{-1}$. Negligible stray capacitance was assumed.

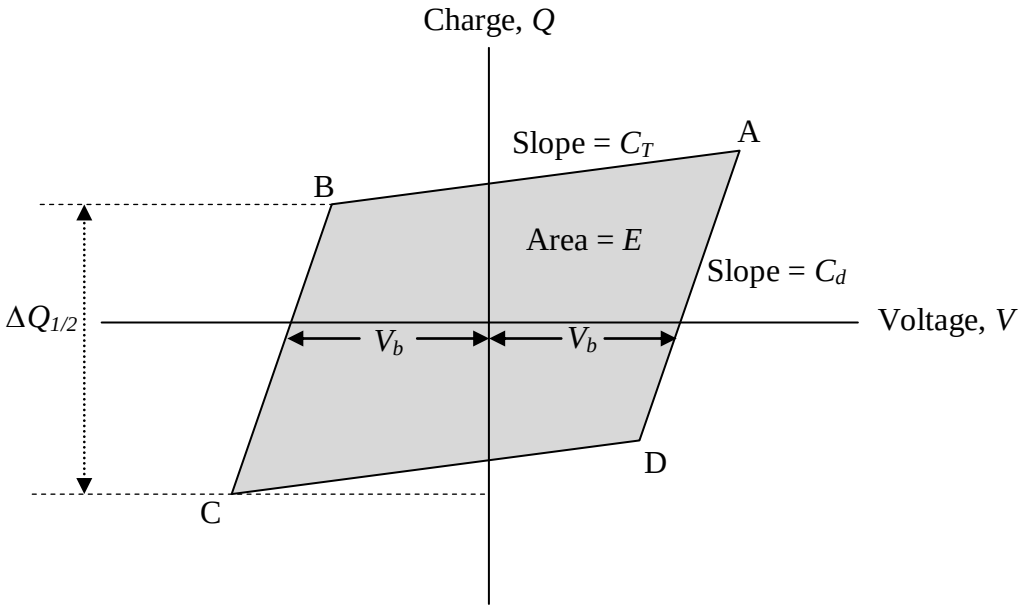


**Figure 3.8.** A typical *Q*-*V* Lissajous plot when DBD is ON.

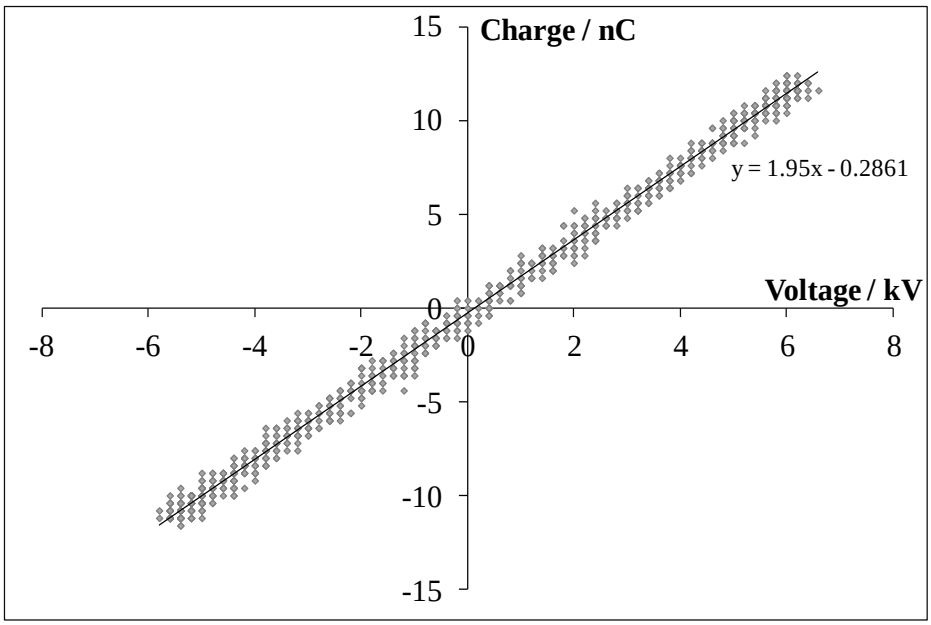


**Figure 3.9.** The *Q*-*V* Lissajous plot when the DBD is OFF.

### 3.2.3 Charge Measurement of the Jet via an Intercepting Plate

To measure the relative net charges transported in the plasma jet by the gas flow, a 'stopping' copper disc of diameter 1 cm is placed to intercept the path of the jet (Fig. 3.10). It is connected to a capacitor (47 nF) in parallel with a resistor (12 MΩ). The *RC* time constant was chosen to be much longer than the period of the AC applied voltage, hence, the DC shift of the voltage measured across the capacitor will give a relative measure the net charges collected on the 'stopping' disc. To confirm that the DC shift was due to the presence of the jet and not an electrical noise, a filamentary DBD was produced in an air gap without gas flow (i.e. no plasma jet was produced), and no DC shift was observed. Likewise, when the 'stopping' disc was placed with its surface parallel to the jet but not touching the jet (approximately 5 mm from the axis), no DC shift in voltage was observed.

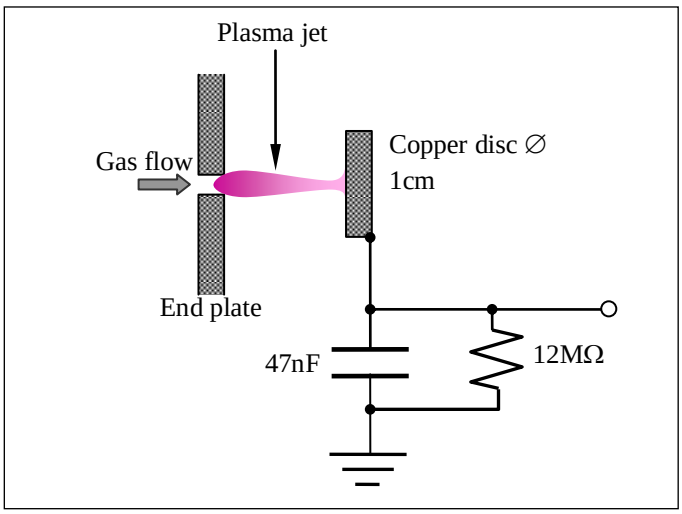


**Figure 3.10.** Arrangement to measure the charges transferred by the plasma jet.

## 3.3 Optical Diagnostics

### 3.3.1 Imaging Setup

The physical structure of the DBD jets (Ar, $N_2$ and Ar:$N_2$) is captured by a digital SLR camera (Canon EOS 40D) featuring a CMOS sensor with 10.1 megapixel. A 18-55 mm lens with *f*/3.5-5.6 was attached to this camera. For the study of physical structure of DBD jet, the shutter speed was adjusted to 4 seconds where the correct exposure was obtained to match with the brightness of the jet while the ISO (image sensor's sensitivity to light) was set to 400 to obtain a better image under dark condition. At higher ISO rating, the sensor is more sensitive to light which can produce more digital noise. The *f*/number, which control the amount of light transmitted to the sensor, is determined by dividing the focal length with the diameter of aperture hole. It was set at *f*/5.6. Higher *f*/number (smaller aperture hole) was chosen where more of the background and foreground fall within the focus. Conversely, with smaller *f*/number (bigger aperture hole), less background and foreground fall within the focus, subject at one distance is in focused, the rest of the image (nearer or farther) is out of focus (blur).

These three elements (shutter speed, ISO and *f*/number) need to be adjusted properly to obtain a higher quality image of the jet.

The camera is positioned to view the jet stream laterally as demonstrated in Fig. 3.11. The plasma jet length and width can be measured from the images whilst plasma density of the jets can only be compared qualitatively based on the brightness of the images.

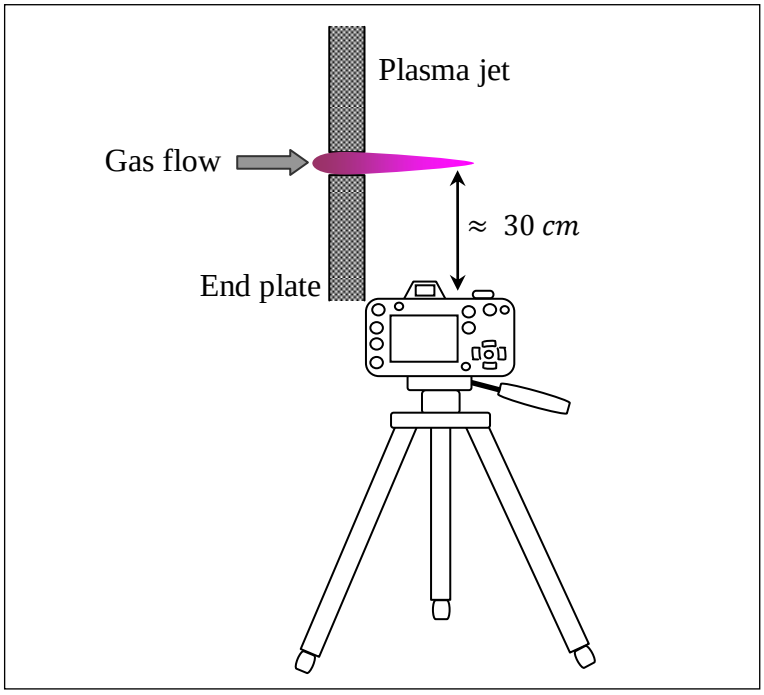


**Figure 3.11.** Position of camera to capture the image of DBD jet.

### 3.3.2 Spectral Emission Measurement

The emission lines of DBD jets were measured by using two spectrometers with different range of wavelength, the shorter wavelengths with Ocean Optics HR4000 high resolution spectrometer and the longer wavelengths with Avantes AvaSpec 3648 USB2 high resolution spectrometer.

### 3.3.2.1 Ocean Optics HR4000 Spectrometer

Ocean Optics HR4000 spectrometer covers the wavelengths from 200 nm - 662 nm. It is able to measure emission lines in the UV-VIS region. The optical resolution for this spectrometer is 0.5 nm Full Width Half Maximum (FWHM). This value is estimated from the product of dispersion (nm/pixel) and pixel resolution with particular slit installed. It also depends on the groove density of the grating and the width of the slit. Better optical resolution can be achieved when smaller slit is chosen. H2 grating with groove density of 600 $mm^{-1}$ and slit of 10 micron width were installed for this spectrometer. It is most efficient at 400 nm while the best efficiency (>30%) can be obtained within 230 nm - 575 nm. The detector installed for this spectrometer is Toshiba TCD1304AP linear Charged Coupled Devices (CCD) array with 3648 detector elements such that sensitivity of 130 photons/count at 400 nm and 60 photons/count at 600 nm can be obtained.

The optical fibre to conduct light to this spectrometer is the solarization-resistant type (QP400-2-SR) with (400$\pm$ 8) µm core diameter, (20 $\pm$3) µm cladding thickness and (45 $\pm$21) µm buffer thickness. The solarization resistant fibre is assembled to resist UV degradation for wavelength below 300 nm (solarization occurs at the wavelength below 300 nm where this effect causes the increased of light absorption in the fibre, hence, the data obtained will be invalid below 300 nm). The relative transmission of the fibre for wavelength 200 nm - 1000 nm is given in Fig. A.1 of Appendix A. It is observed that the transmission loss is large for wavelength below 300 nm.

### 3.3.2.2 Avantes AvaSpec 3648 High Resolution Spectrometer

The useable wavelength for Avaspec spectrometer ranges from 500 nm to 1000 nm (VIS-NIR region). It is based on the Symmetrical Czerny-Turner design of 75 mm focal

length. The Toshiba CCD detector is similar to that described above. The integration time for this spectrometer can be varied from 10 μs to 10 min. The grating for this spectrometer has 600 lines/mm and it is most efficient at 750 nm. The spectral range is 500 nm and the slit size is 10 μm (≈2.33 pixels). Hence, the optical resolution is 0.32 nm FWHM.

### 3.3.2.3 Setup for Measurement of Spectral Emission

The setup of the spectral emission measurement using HR 4000/AvaSpec3648 Spectrometer is shown in Fig. 3.12. The fibre tip was placed at 2.0 mm away from the circular end plate, facing the jet stream head-on in order to collect sufficient level of light intensity. When viewed laterally, the light intensity was too dim for detection by the spectrometer even when the integration time was set to the highest. To avoid modification or contamination to the quartz fibre tip due to direct contact with the jet, the fibre tip was covered by a thin piece of borosilicate glass microscope coverslip (thickness 0.15 mm). This coverslip allows 10% transmission at 285 nm, rising to 50% transmission at 310 nm, then to 90% transmission at 360 nm, maintaining at the high transmission level up to 2200 nm. Hence, the UV radiation was still detectable. The other end of the optical fibre was connected to the entrance slit of the spectrometer through SMA 905 connector with numerical aperture of 0.22.

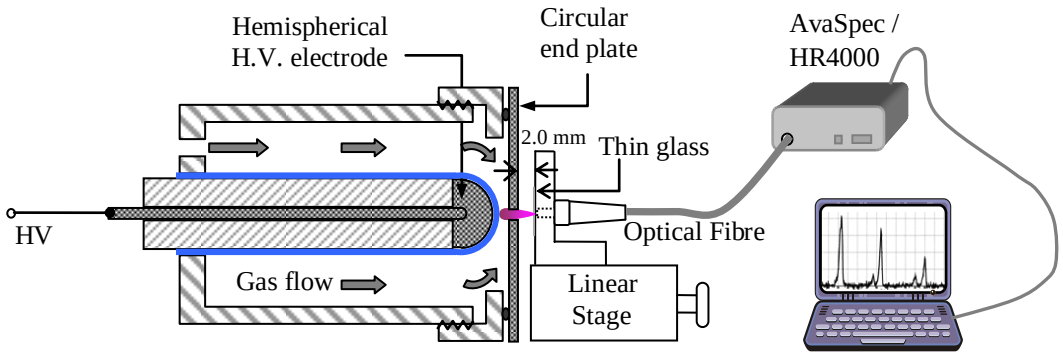


**Figure 3.12.** The arrangement of spectral emission measurement

The integration time was set at 200 ms. Increase in the integration time resulted in higher intensity obtained where more light is directed to the detector during a single scan. Saturation of the signal can be observed when the signal reaches the maximum counts. The emission spectrum was recorded by a computer through the Spectra Suite and AvaSoft 7.6 software packages for the respective spectrometers. The wavelength readings for both spectrometers were calibrated against a standard Hg lamp source.

## 3.4 Surface Treatment

### 3.4.1 Sample Preparation

The DBD jet was applied on a Mylar film or often referred to as plastic film. It is made from Polyethylene Terephthalate (PET) resin. PET was chosen for this study as it is easy to obtain, inexpensive, has good thermal resistance and high strength to weight ratio (Kostov et al., 2010). Due to the distinct properties of PET, it is widely used in packaging and various industrial processes. PET surfaces are usually difficult to wet and do not adhere to other material (poor adhesion) due to the low surface energy and weak chemical reactivity at the surface (Borcia, Anderson, & Brown, 2004). The poor wetting

and adhesion of PET surface can be improved by surface treatment using atmospheric pressure DBD jet.

The thickness of Mylar film chosen was 0.135 mm. The dimension of each Mylar film was 2 cm × 1 cm. Each Mylar film was cleaned with alcohol to ensure clean surface before treatment by DBD jet. Marking was made at the back of the Mylar film to indicate the location to be treated.

### 3.4.2 Sample Positioning

The clean Mylar film was positioned at 1.0 mm from the grounded electrode. It was aligned on the Perspex stand and fixed on a linear stage with vernier scale as depicted in Fig. 3.13.

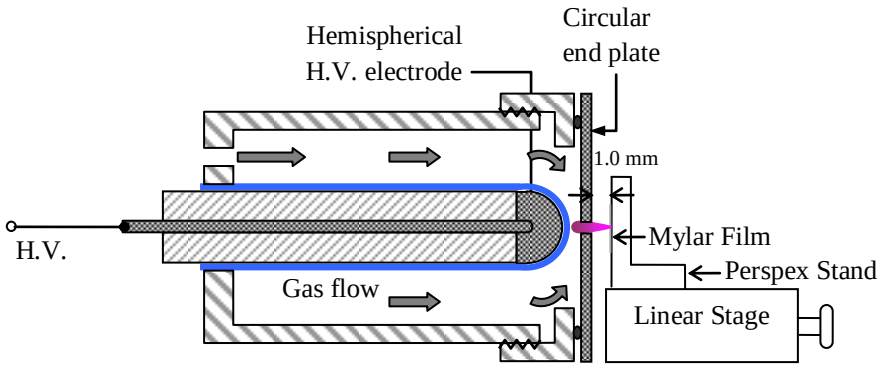


**Figure 3.13.** The setup of sample positioning. Sample was positioned at 1.0 mm from the grounded electrode.

### 3.4.3 Contact Angle Measurement

The observation of surface treatment was achieved by static contact angle measurement. It is based on the three phase contact point measurement method where the angle formed when the three phases (gas, liquid and solid) intersect (Shao, Zhang,

Zhan, & Xu, 2011). The surface wettability was studied by analyzing the changes of contact angle on Mylar film.

The Mylar film was placed on the horizontal base, resting as horizontal as possible to give the correct measurement of contact angle. Water contact angle, $\theta$ is the angle between the baseline of the water droplet and the tangent of the liquid/vapor boundary. The cross-sectional view of the water droplet and contact angle is illustrated in Fig. 3.14.

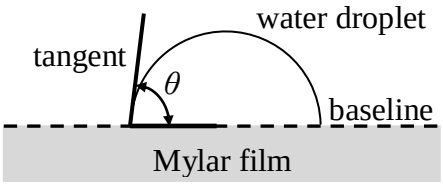


**Figure 3.14.** The contact angle, $\theta$ at the three-phase boundary.

The contact angle can be used to evaluate the wetting and adhesion of a solid by liquid. A smaller value of contact angle indicates a better wetting where the liquid spreads on the solid. The interaction force between solid and liquid is strengthened when wetting occurs and the surface has more adhesion to liquid. A higher value of $\theta$ indicates poor wetting of the solid where the interaction force between the solid and liquid is poor, resulting in lower surface energy. When the solid is completely wet, the contact angle is zero.

### 3.4.4 Surface Treatment Procedure

Mylar films were treated by DBD jets operating in $N_2$ and Ar gas, both were flowing at corrected rate of 6 LPM. At lower flow rate, the charges transported into the jet stream are low whereas at too high flow the consumption of gas is high which will increase the operating cost. The contact angle for Mylar film not exposed to plasma jet was determined for the conditions (a) without gas flow (discharge confined internally)

and (b) with gas flow (but no plasma excitation). These are the control conditions for the surface treatment.

The observation of the contact angle as a function of treatment time was carried out initially to determine the optimum treatment time for surface wetting. A 2 µL drop of Deionized (DI) water was dropped onto the surface of Mylar film by using an Eppendorf pipette (2-20 µL). DI water was used as it is free from contaminants. Treatment time was set at 15 s, 30 s, 60 s, 90 s and 120 s. The treatment time did not exceed 120 s to avoid over heating of the system especially with Ar as operating gas. The heating effect can induce minor cracks on the surface of the glass test tube and the discharge will transform to arc discharge. Heating is not so pronounced in $N_2$ DBD jet, hence, longer treatment time (>120 s) can be applied. The optimum treatment time of 120 s was determined by selecting the lowest contact angle obtained for treated Mylar film without overheating. Hence, fixing optimum treatment time at 120 s, the ageing test was next performed where the contact angle was measured up to 168 hours (7 days) at various intervals. A final measurement of contact angle was performed after 50 days of ageing to ascertain if full hydrophobic recovery is achieved.

For the ageing test, the Mylar film was stored in a Petri dish with cover after each treatment at room temperature to avoid dust in the atmosphere being deposited on the treated surface and affect the ageing process.

The image of each water droplet was captured by a digital camera (Sony NEX 3, 14.2 Mega Pixels) and the images were cropped into equal sizes in Adobe Photoshop CS3. The contact angles were measured by digital screen ruler (MB-Ruler). All the measurements were carried out manually without using commercial contact angle measuring software for calculation.

# CHAPTER 4

## Electrical and Optical Characteristics of DBD Jet

### 4.1 Electrical Characteristics of DBD Jet

#### 4.1.1 Ignition Voltage

The ignition voltage, $V_{ON}$ was obtained by increasing the applied voltage slowly until a threshold value when the discharge is initiated (i.e., at the instance when current filaments begin to appear). It is found to depend on the gap width, gas pressure and type of gas used. The ignition in Ar for fixed air gap of 0.5 mm is the easiest while $N_2$ requires the highest ignition voltage, with Ar:$N_2$ (47%:53%) mixture in-between as shown in Fig. 4.1. (All gas flow rates reported have been corrected for temperature, pressure and gas density). This is expected as Ar has much lower dielectric strength in comparison to $N_2$ (0.18 of that for $N_2$). $V_{ON}$ increases as the gas flow rate is increased. This dependence is due to the pressure that builds up inside the DBD jet reactor as the size of the outlet (1 mm diameter) is much smaller than the inlet (5 mm diameter). This pressure was measured immediately before the inlet with a Bourdon Tube Gauge. Fig. 4.2 shows the built-up pressure increases as flow rate is increased, hence the product of pressure and gap width, *pd*, increases and higher $V_{ON}$ is required.

To estimate the proportion of voltage effectively applied across the gap, we need to consider the dielectric, gap and total capacitances of the DBD jet arrangement. The dielectric capacitance, $C_d$ estimated from geometry is 21 pF and the measured total capacitance, $C_T$ from the *Q*-*V* Lissajous plot when discharge was off is 2 pF (refer Fig. 3.9). This gives a gap capacitance, $C_g$ of 2.2 pF from the relation,

$C_g = C_T C_d / (C_d - C_T)$. The breakdown is across the gap, hence the effective ignition voltage is actually the gap voltage which is 0.9 $V_{ON}$ calculated from capacitive voltage division. However, this effective ignition voltage is still twice as high as the 'sparking' potential reported for plane parallel plates in pure Ar (Kachickas & Fisher, 1953). Assuming atmospheric pressure (760 torr) and gap width 0.5 mm, the smallest value of *pd* in our arrangement is 38 Torr-cm and this rules out Townsend breakdown that leads to homogeneous/glow discharge occurring typically at $pd < 30$ Torr-cm (Massines et al., 2009).

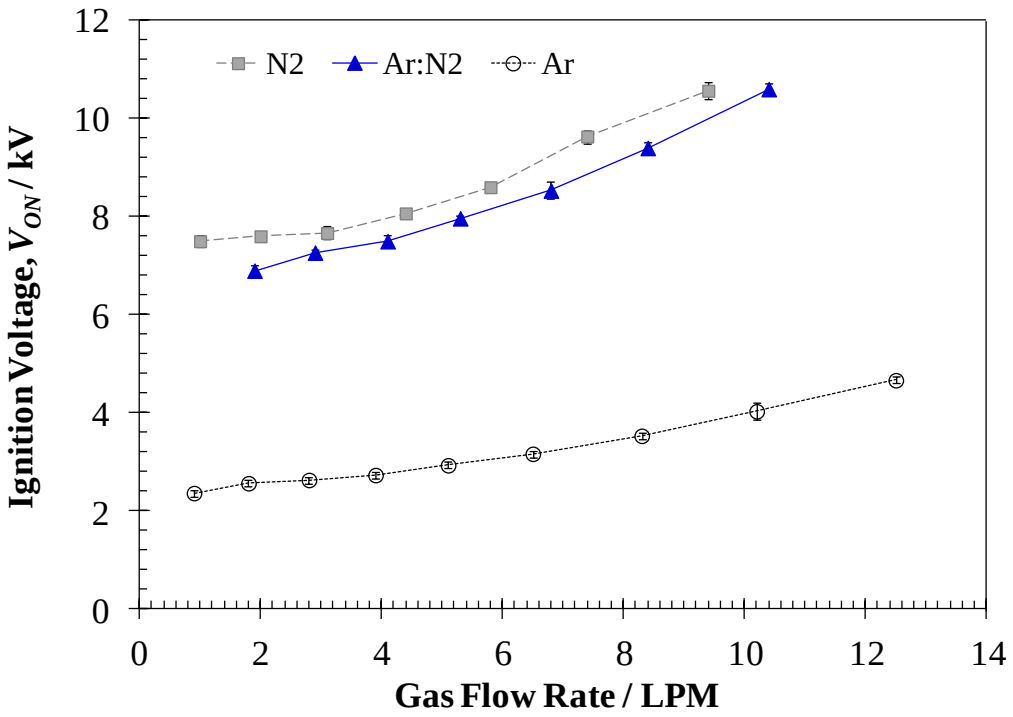


**Figure 4.1.** Ignition voltage (measured as peak AC voltage across the electrode) versus flow rate for different gas compositions.

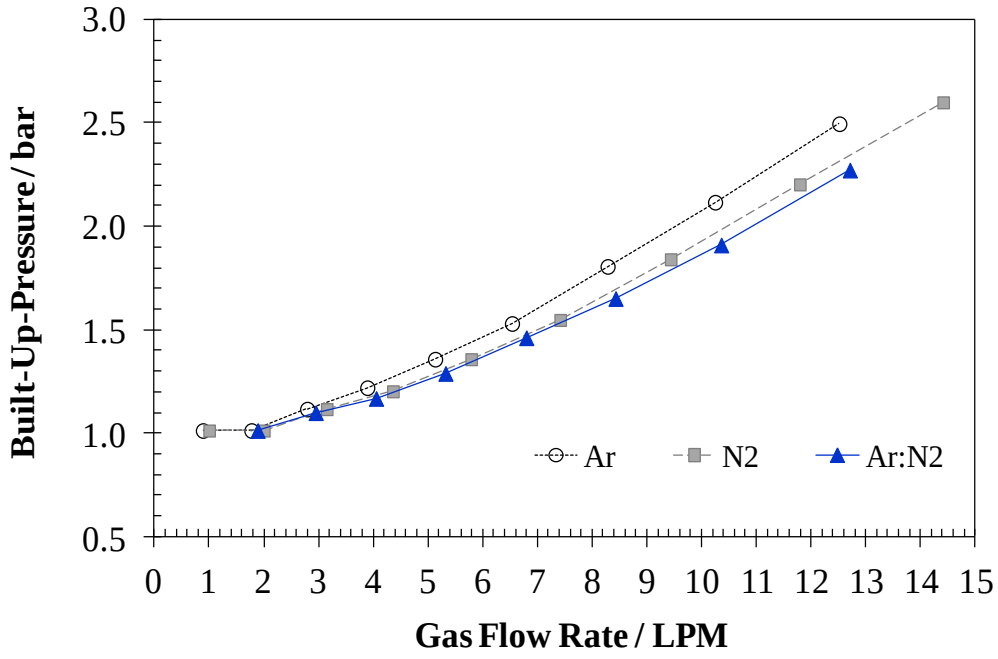


**Figure 4.2.** Dependence of built-up pressure in the reactor on gas flow rate for different gas compositions.

When the gap width widens, the ignition voltage increases for $N_2$, Ar and Ar:$N_2$ gas. Higher voltage is required for the electrons to bridge the gap and to sustain the discharge at wider gap width. For 0.5 mm gap width, the voltage required to ignite the discharge at 3 LPM for $N_2$, Ar and Ar:$N_2$ are 7.7 kV, 2.6 kV and 7.3 kV respectively whereas at 1.5 mm gap, the ignition voltages are 10.2 kV ($N_2$), 3.5 kV (Ar) and 7.9 kV (Ar:$N_2$). Ignition in $N_2$ gas shows a strong dependence on the gap width where the voltage difference of 2.5 kV was obtained between 0.5 mm and 1.5 mm gap at the gas flow of 3 LPM. In the case of Ar and Ar:$N_2$, the voltage difference was smaller, at 0.9 kV and 0.6 kV respectively. The results of the dependence of ignition voltage on gas flow rate of $N_2$ and Ar for different gap widths (0.5 mm, 1.0 mm, and 1.5 mm) are shown in Fig. 4.3.

The relation between RMS ignition voltage and *pd* is plotted as shown in Fig. 4.4. It can be seen that the ignition voltage rises as the *pd* increases for Ar and $N_2$ DBD jet at 0.5 mm, 1.0 mm and 1.5 mm gap widths. Comparing to the Paschen curves for Ar and

$N_2$ as reported in (Raizer, 1991, p.134), the ignition voltage measured for Ar DBD jet in this experiment exhibits similar trend except the value of ignition voltage is higher. It is noted that the discharge in the reported case was ignited in uniform field with bare electrodes, different from the DBD jet configuration. The ignition voltage for $N_2$ from experiment could not be compared with the reported values of which the data range was limited to <10 Torr-cm. Another comparison is made to the calculated ignition voltage for Ar and $N_2$ discharges based on principles of Paschen's Law with the assumption of uniform field (similar to the reported case above). The voltage when breakdown occurs were calculated using the following equations:

$$V_b = \frac{B\,(pd)}{C + \ln pd} \qquad (4.1)$$

$$C = ln\,\frac{A}{\ln(\frac{1}{\gamma} + 1)} \qquad (4.2)$$

where $V_b$ is the ignition voltage in V, $p$ is the pressure in Torr and $d$ is the gap width in cm. The electric field, $E$ for the DBD jet in this setup is approximately 8 kV-10 kV across gap width of 0.05 cm to 0.15 cm, yielding a reduced field $E/p$ of approximately 70-260 V/cm-torr (taking $p$ = 760 torr). Hence, the constants $A$ and $B$ chosen for Ar is 12 $cm^{-1}Torr^{-1}$ and 180 V/cm-Torr (valid for $E/p$ = 100-600 V/cm-torr) while for $N_2$, the constant $A$ is 8.8 $cm^{-1}Torr^{-1}$ and $B$ is 275 V/cm-Torr ( valid for $E/p$ of 27-200 V/cm-torr). Both constants $A$ and B depend upon the gas compositions and these values were obtained from (Raizer, 1991, p.56). The secondary emission coefficient, $\gamma$ was chosen to be 0.01 for Ar (Auday, Guillot, Galy, & Brunet, 1998) and 0.002 for $N_2$ (Jones, 1968).

The calculated Paschen curves for Ar (indicated in blue line) and $N_2$ (indicated in red line) are shown in Fig. 4.4. It is found that the data points from experiment for Ar at 0.5 mm gap width agree with calculated results whereas for Ar at 1.0 mm and 1.5 mm gap widths, the ignition voltages are lower than the calculated values. On the other hand, the ignition voltages for $N_2$ obtained from experiment are higher than the calculated

values. The difference between the calculated and measured ignition voltage is because the calculated values were estimated based on the parallel plate configuration with bare electrodes where the field is uniform. It is clear that Paschen law derived from Townsend ionization consideration cannot accurately predict the breakdown condition for the present geometry. In this setup, the dielectric field between the hemispherical electrode and ground plate is non-uniform with a dielectric barrier between them and the discharge is in filamentary mode. However, the trend of increasing ignition voltage with increase in *pd* is still observed.

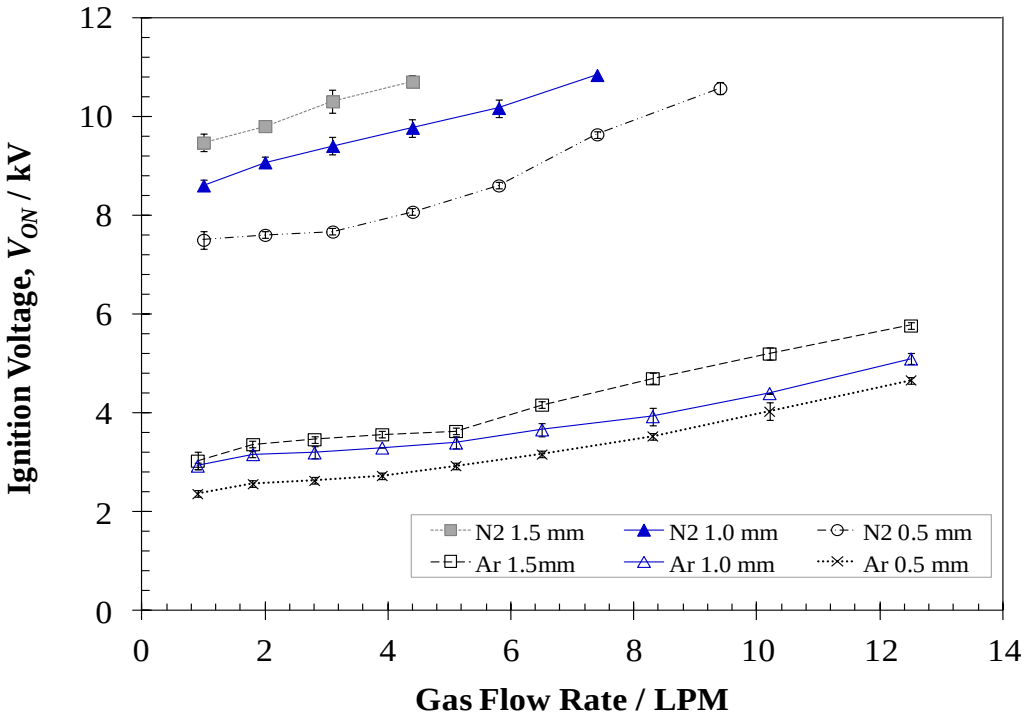


**Figure 4.3.** Dependence of ignition voltage on gas flow rate for Ar and $N_2$ gas at different gap widths.

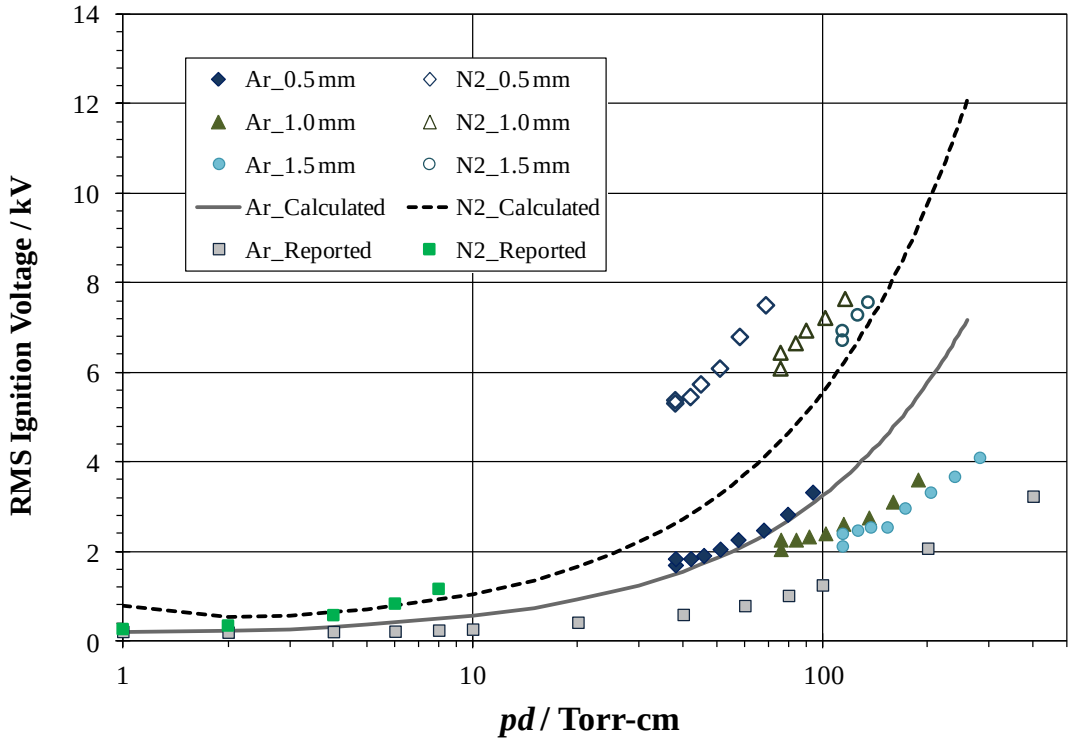


**Figure 4.4.** The dependence of RMS ignition voltage on *pd* (in Torr-cm) for Ar and $N_2$ gas at 0.5 mm, 1.0 mm and 1.5 mm gap width. The calculated Paschen curve is indicated in black line for Ar and dotted line for $N_2$ gas.

### 4.1.2 Voltage-Current Waveforms

The behaviour of the discharge is characterized by the current filaments of short rise time and narrow width formed between the electrodes, usually of the order of nanoseconds. The DBD jet shows a capacitive load when the discharge is not ignited where the current leads the voltage by 90°. This is shown in Fig. 4.5. The discharge occurs in the form of multiple short-lived current spikes, mostly at the 1st and 3rd quarter cycles of the AC voltage waveform as shown in Figs. 4.6 (a)-(c) typical of filamentary mode DBD (Gherardi, Gouda, Gat, Ricard, & Massines, 2000). The current spikes can be termed as current filaments or microdischarges. The current signal comprised of two components, a displacement current (due to capacitive impedance of the electric circuit of the discharge arrangement) and the ohmic plasma current arising from the discharge process (Reichen, Sonnenfeld, & von Rohr, 2010). The displacement

current consists of a sine wave that is out of phase with the voltage signal that does not lead to any discharge phenomenon while the ohmic plasma current consists of a series of current spikes with different amplitudes. The current filaments are randomly distributed over the surface of the dielectric, mostly near the round end of the glass test tube. They extinguish when the applied voltage reaches its peak (positive and negative half-cycles).

Ar discharge can sustain the highest number of current filaments and $N_2$ discharge the least. This corresponds to the lower voltage required for ignition in Ar (2.4 kV at 1 LPM to 4.7 kV at 12.5 LPM) compared to $N_2$ (7.5 kV at 1 LPM to 10.6 kV at 9.4 LPM) due to the lower dielectric strength in Ar. Adding Ar to $N_2$ in the proportion of 47%:53% promoted micro-discharge formation but not significantly (Fig. 4.6 (c)).

The behavior of the discharge depends on the gas mixture used. This was observed through the occurrence of the first positive and negative current spikes of each half-cycle. In Ar, they occur earlier before the voltage reversal but are still at the respective positive and negative voltage slopes reminiscent of a capacitive load. Charges deposited on the dielectric during the preceding cycle allow the current spikes to occur before the voltage reversal. This observation is similar to that reported in a configuration where the inter-electrode discharge in Ar is confined within a quartz capillary (Nikiforov, Sarani, & Leys, 2011).

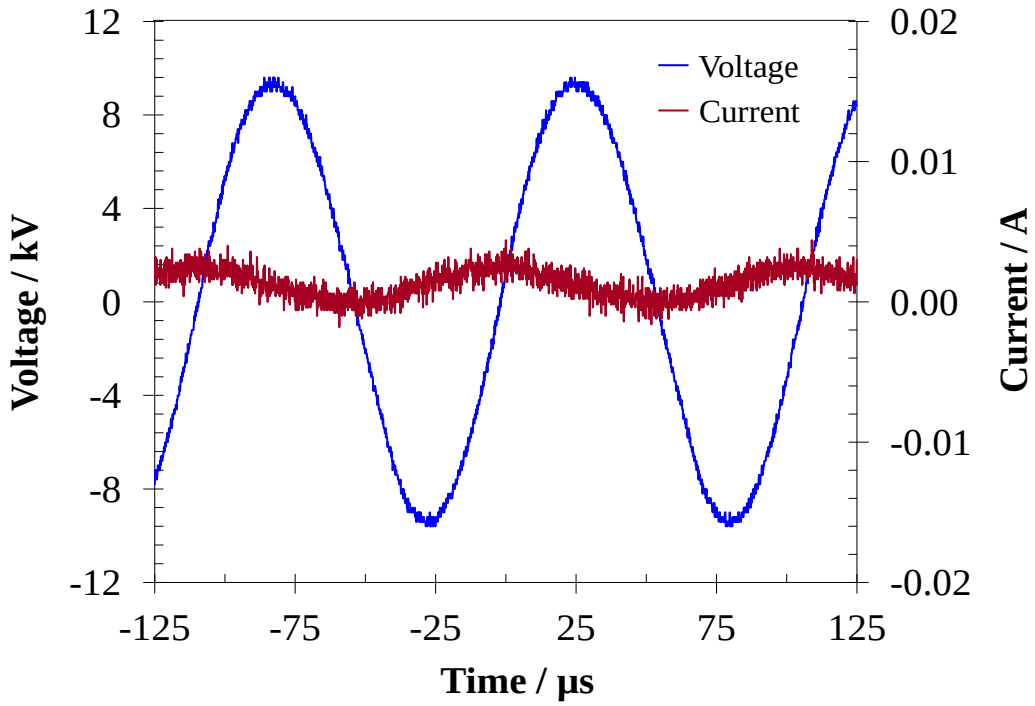


**Figure 4.5.** Voltage and current waveforms when the discharge is OFF.

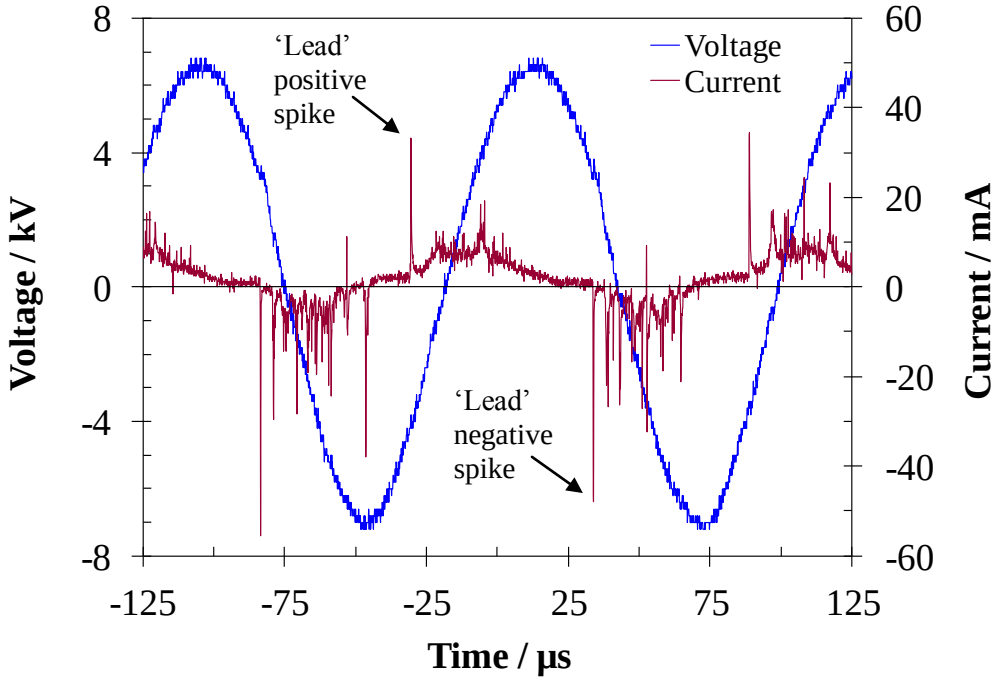


**Figure 4.6 (a).** Discharge voltage (14 kVp-p) and discharge current of the DBD jet with 0.5 mm gap in Ar at flow rate of 3 LPM.

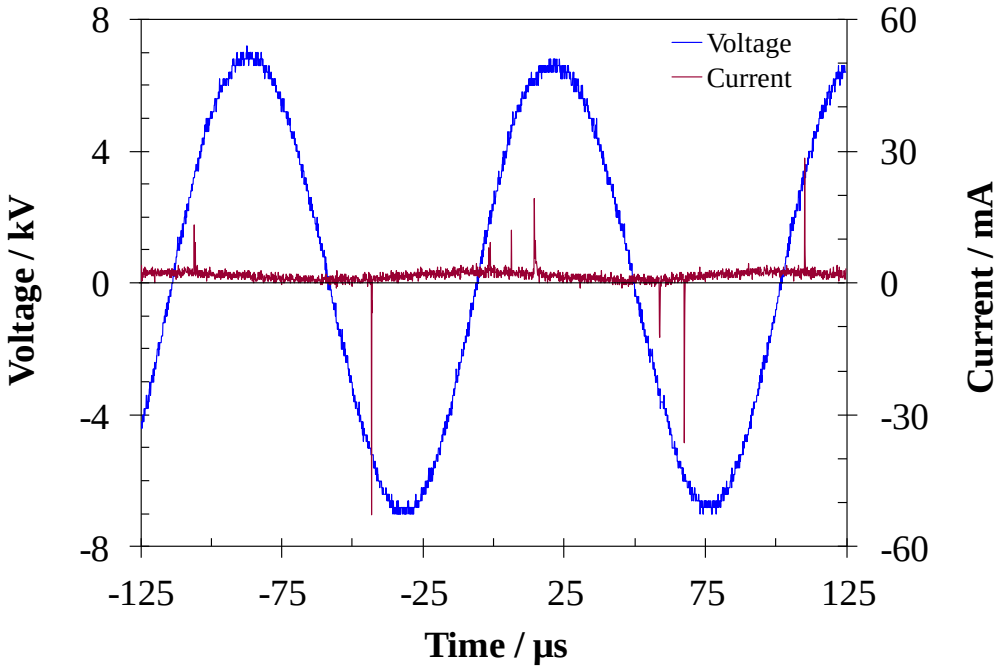


**Figure 4.6 (b).** Discharge voltage (14 kVp-p) and discharge current of the DBD jet with 0.5 mm gap in $N_2$ at flow rate of 3 LPM.

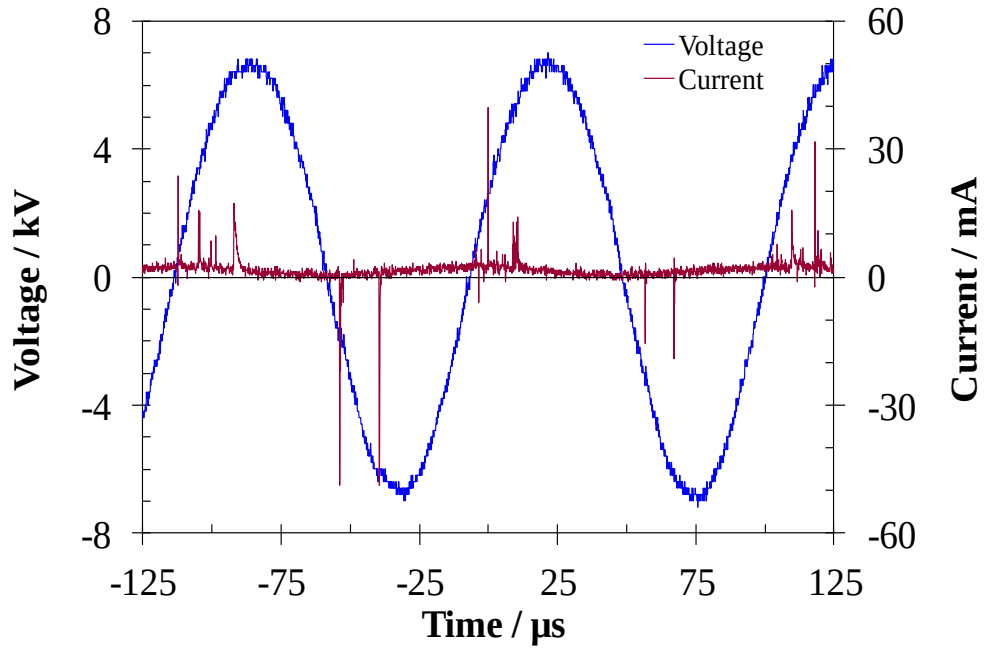


**Figure 4.6 (c).** Discharge voltage (14 kVp-p) and discharge current of the DBD jet with 0.5 mm gap in Ar:$N_2$ at total flow rate of 3 LPM.

### 4.1.3 Current Filaments

#### 4.1.3.1 Positive Current Filaments

At the rising edge of AC voltage, a series of current filaments were observed. The current filaments in Ar displays a distinct 'lead' current filament of duration 100-400 ns followed by a quiet interval of 4-6 μs before a subsequent series of multiple filaments appears as shown in Fig. 4.6 (a) and Figs. 4.7 (a)-(b). This feature is not observed in $N_2$ and Ar:$N_2$ current signals. It is likely to be attributed to Ar gas peculiarity as its occurrence was also reported in (Nikiforov et al., 2011). The 'lead' current spike could be a superposition of successive multiple filaments of shorter duration (≈ 20 ns each) (Fig. 4.7 (b)) and may overlap spatially, forming conducting streamer channels with larger radii that were observed in inert gases rather than $N_2$ or air (Kogelschatz, 2003). Multiple shorter peaks superimposed on longer duration current signal were also observed in Ar and Kr DBD by Radu et al (Radu, Bartnikas, Czeremuszkin, & Wertheimer, 2003). They attributed it to surface streamers over the periphery of the dielectric layer.

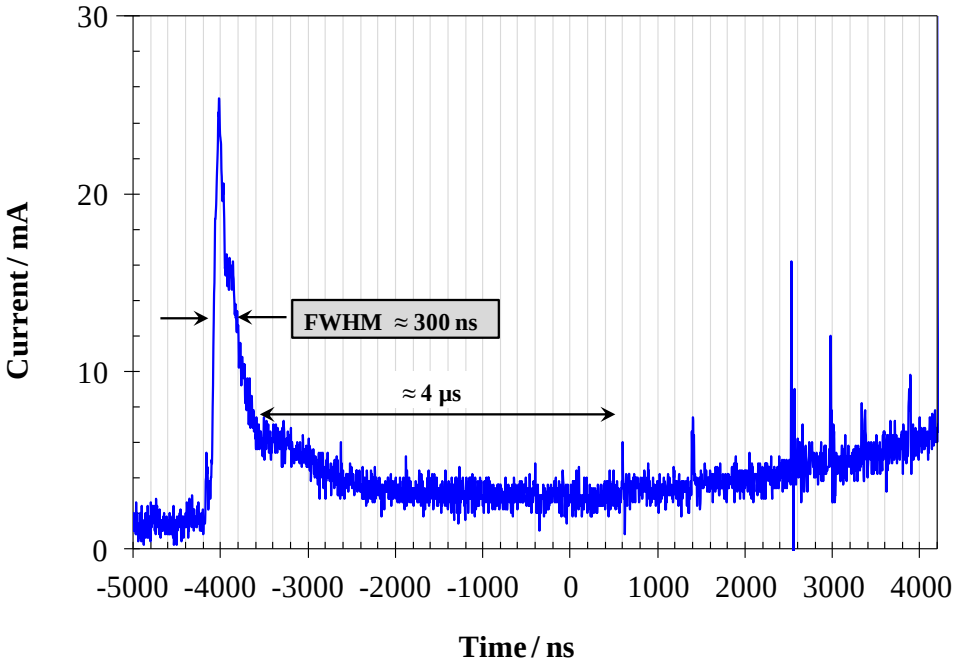


**Figure 4.7 (a).** The positive 'lead' current filament followed by a series of shorter duration current filaments after ≈ 4 µs in Ar DBD jet at 0.5 mm gap and 3 LPM of gas flow.

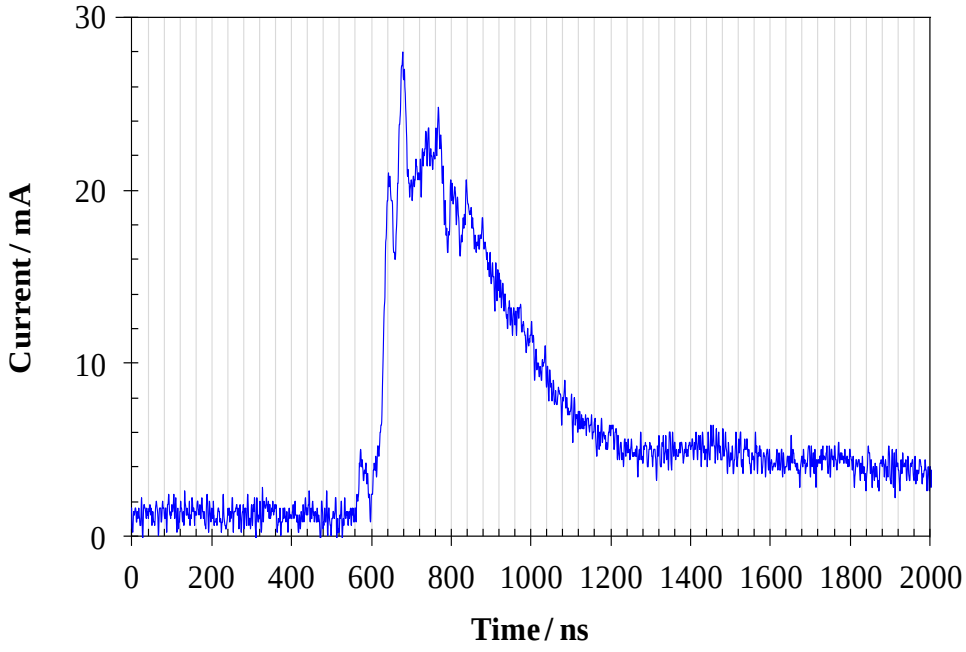


**Figure 4.7 (b).** The 'lead' current filament shown in Fig. 4.7 (a) displayed in expanded time.

The FWHM of single current filaments appearing after the 'lead' current spike in Ar discharge is approximately 10-20 ns, similar to those obtained from $N_2$ jet. The expanded time frame of these current filaments is shown in Figs. 4.8 (a)-(b). It is observed that they are under-damped and this feature is independent of gap width, applied voltage and gas flow rate. A series of positive current filaments over time interval of 10 μs for Ar and $N_2$ are shown in Figs. 4.9 (a)-(b). Both have similar features other than difference in the number of filaments.

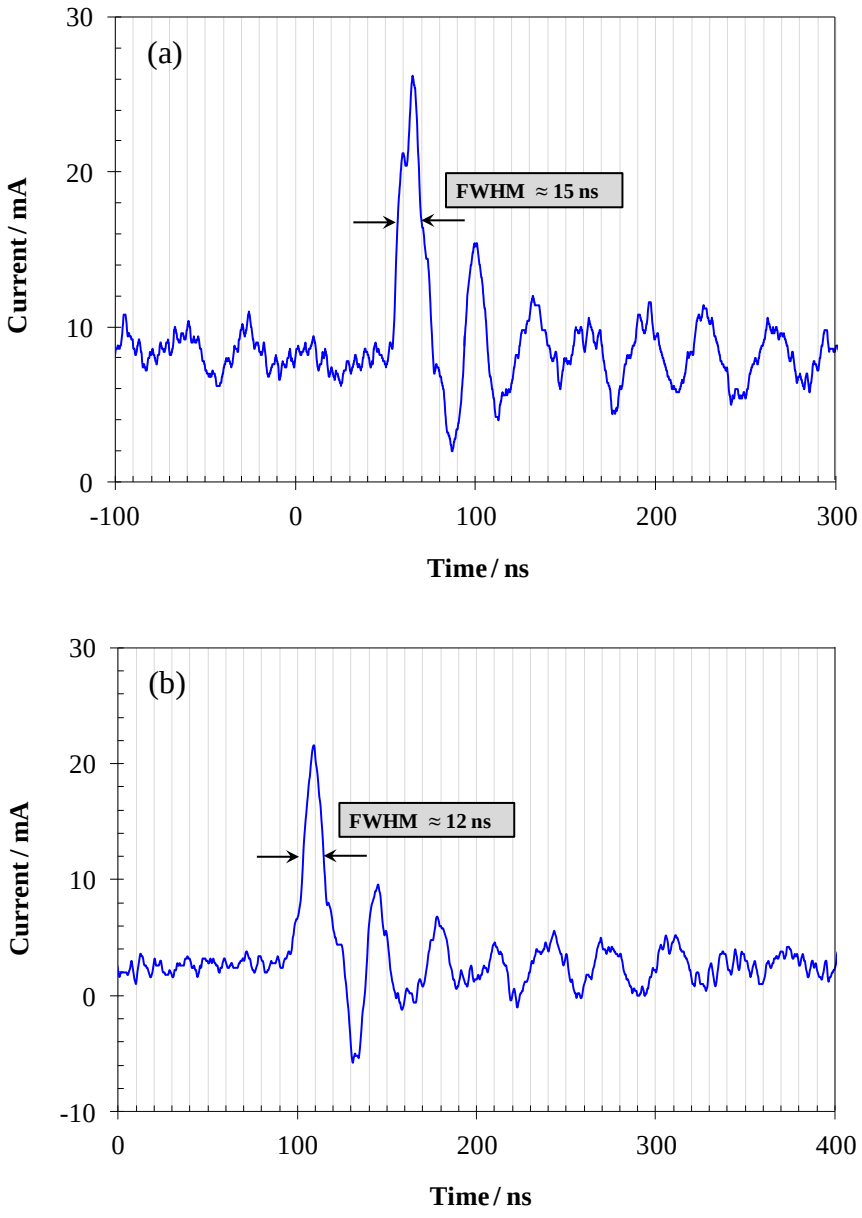


**Figure 4.8.** Typical current filaments of 10-20 ns for (a) Ar, and (b) $N_2$ DBD jet at 0.5 mm gap.

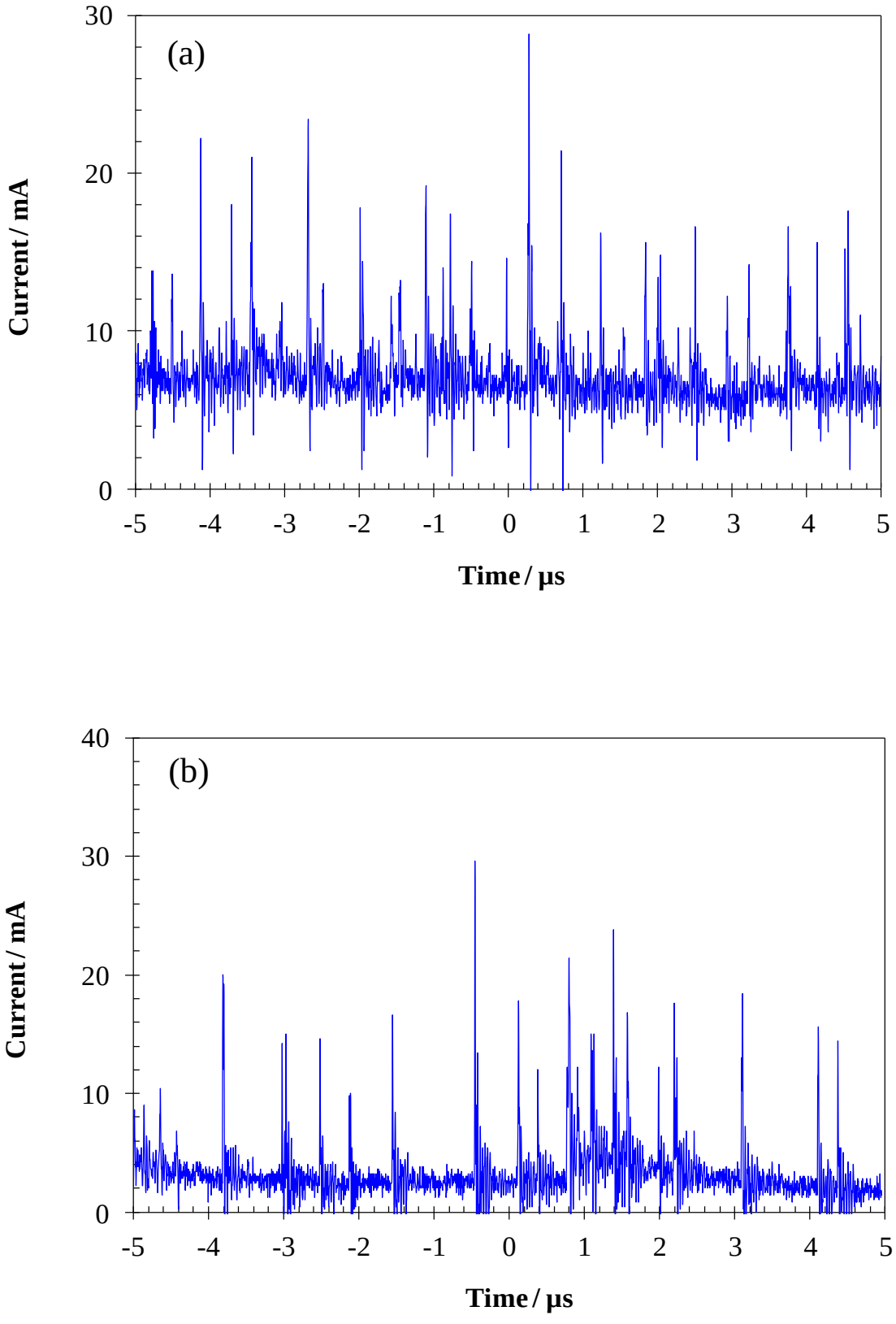


**Figure 4.9.** Series of positive current filaments over 10 µs across 0.5 mm gap for (a) Ar and (b) $N_2$ DBD jet at 3 LPM.

#### 4.1.3.2 Negative Current Filaments

Negative current filaments were observed when the AC voltage polarity changes that is, when H.V. hemispherical electrode is negative and grounded plate is positive. Electrons are moving from H.V. electrode to the grounded plate. A series of Ar and $N_2$ negative current filaments are shown in Figs. 4.10 (a)-(b). It is observed that the peak magnitude of negative current filament is larger than the peak magnitude of positive current filament (compare to Figs. 4.9 (a)-(b)). This feature is due to the difference in the surface conductivity when electrons come in contact with the surface. When the electrons bridge the air gap and reach the dielectric during the positive pulse, the higher surface resistance of the dielectric limits the discharge current. Some of the electrons are trapped at the dielectric surface, form an electric field opposite in direction to the external field between the electrodes. Hence, conductivity of the dielectric is reduced and smaller amplitude of current filaments was observed when H.V. hemispherical electrode is covered by the dielectric. In contrast, when the electrons reach the grounded plate (at positive polarity relative to the negative H.V. hemispherical electrode), they flow to the external circuit without being trapped at the surface, resulting in the formation of relatively larger current filament (Bartnikas, Radu, & Wertheimer, 2007).

The 'lead' current spike observed in positive current filament for Ar discharge was also observed in the negative current filament as shown in Fig. 4.11. However, the FWHM of the negative lead current is 100 ns - 200 ns, narrower than the positive 'lead' current spike shown in Fig. 4.7 (b). The expanded time frame of the negative lead current filament is presented in Fig. 4.11. The interval time between the 'lead' negative current and the subsequent series of multiple current filaments is about 3 μs, slightly less than that in the positive current. Both positive and negative 'lead' current spikes were not observed in $N_2$ discharge.

The magnitude of the ‘lead’ positive and negative currents increased with the gas flow rate. The magnitude of the subsequent series of current filaments after the ‘lead’ spike was lower and varied randomly. The tendency of two and more current filaments with lower magnitude to merge to one peak could be observed as each of the current filaments broadens. This broadening of current filaments was also observed by Reichen et al., when the channel velocity was increased (Reichen et al., 2010).

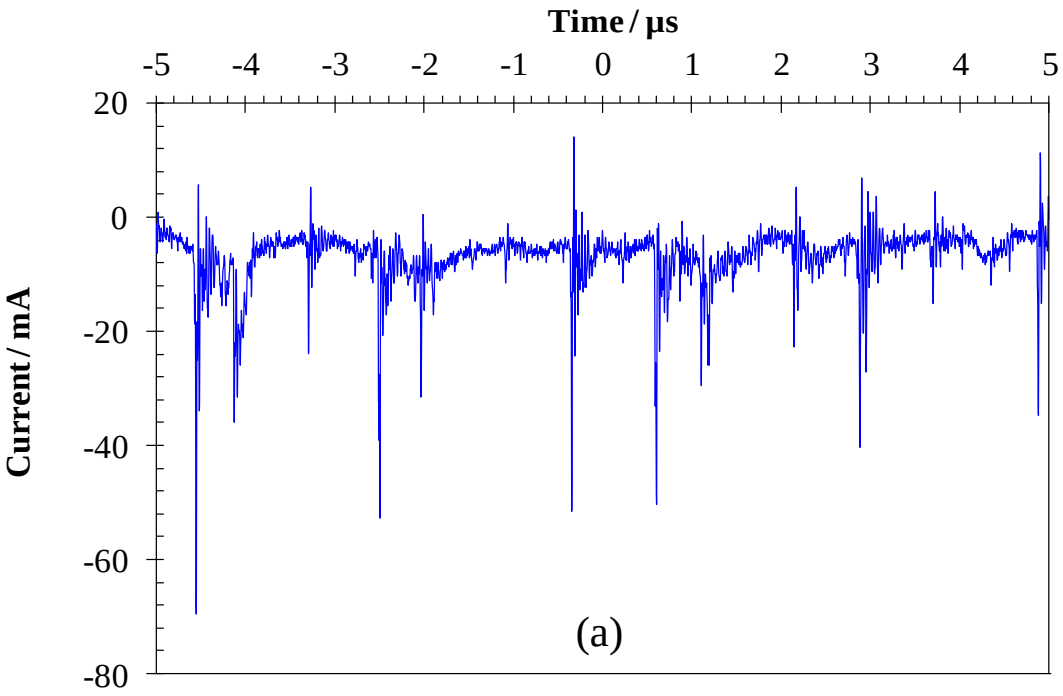

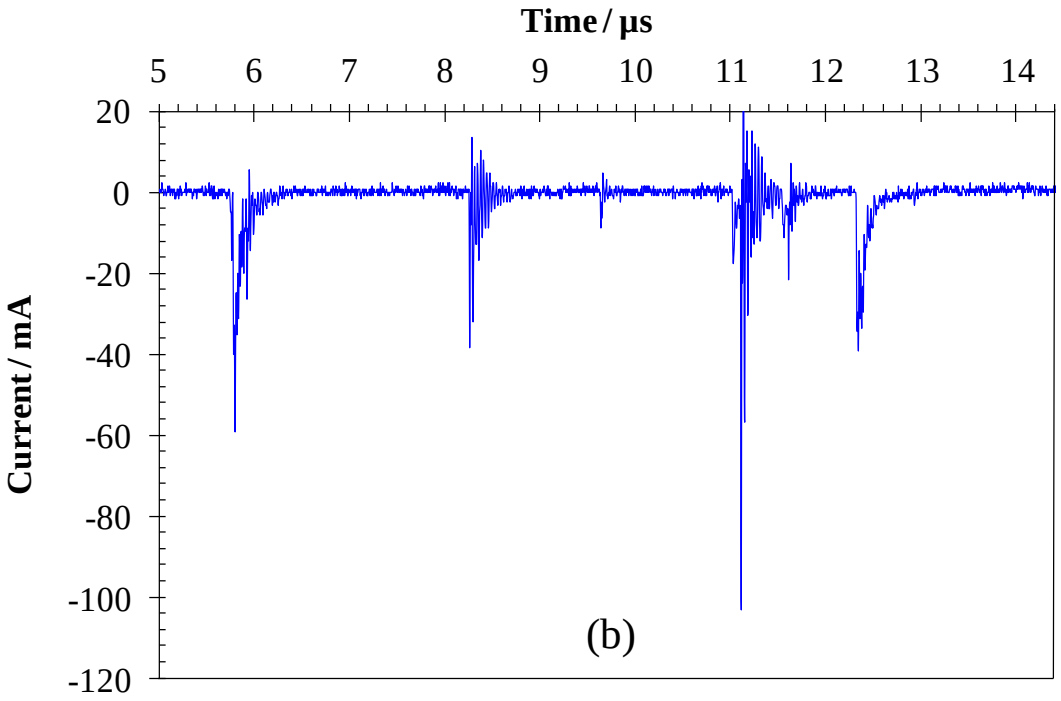


**Figure 4.10.** Series of negative current filaments over 10 µs across the 0.5 mm gap for (a) Ar and (b) $N_2$ DBD jet at 3 LPM.

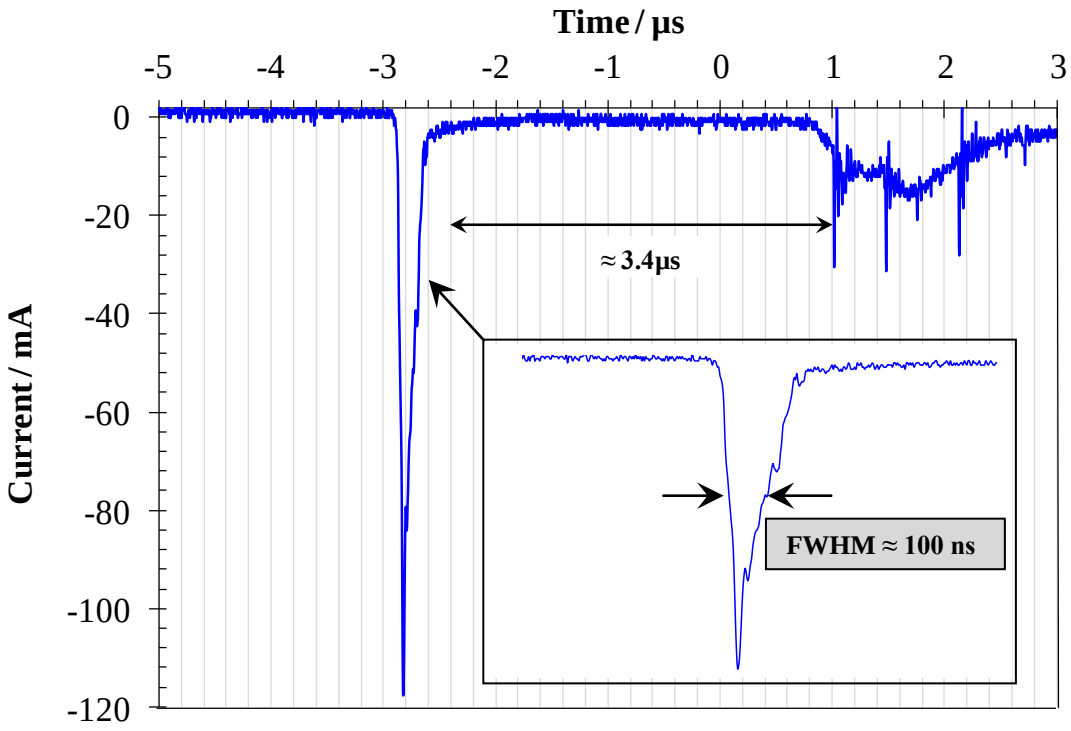


**Figure 4.11.** The time interval between the negative 'lead' current filament and series of current filaments for Ar DBD jet at 0.5 mm gap and 3 LPM of gas flow.

### 4.1.3.3 Number of Current Filaments

The counting of the number of positive current filaments was carried out for Ar and $N_2$ discharges to study the effect of gas flow rate and applied voltage on the number of current spikes for different gap width. The number of positive current filaments generally reduces as the gas flow rate is increased for 0.5 mm, 1.0 mm and 1.5 mm gap at fixed applied voltage as shown in Figs. 4.12 (a)-(b). The occurrence of the first current filament of each positive and negative cycle was delayed in time when the flow rate is increased and is shown in Figs. 4.13 (a)-(b) for $N_2$ discharge whereby the current signals at various gas flow rates were superimposed. The duration of occurrence, $\Delta t$ of current filaments within each half cycle or discharge duration, reduces at higher gas flow rate. The value of $\Delta t$ for Ar and $N_2$ discharges were given in Tables 4.1 (a)-(b). Increasing the gas flow rate retards the breakdown, thus, fewer number of current filaments were obtained at higher flow rate while lower flow rate sustains longer discharge duration. This is due to the higher pressure built up at higher gas flow rate (Fig. 4.2) whereby increased voltage is needed to cause breakdown. Higher voltage is required to compensate the larger number density at higher pressure so that more current filaments can be produced. Another factor which affected the number of current filaments at higher flow rate is the residence time, $\tau$ of the gas particles in the gap space between the electrodes. $\tau$ can be roughly estimated by dividing the discharge volume, $V_{discharge}$ with gas flow rate, $Q$ (Nwankire et al., 2010). It decreases with the increase of flow rate. Gas particles stayed longer between the electrodes at lower flow rate, and more current filaments is expected to be observed.

Ar discharge produced more current filaments compared to $N_2$ discharge. It was found that at 14 kV and 0.5 mm gap, the estimated number of positive current filaments per half cycle ranged from 96.3 at 1 LPM to 74.9 at 12.5 LPM. The estimated number of current filaments in $N_2$ discharge was much less than Ar current filaments even

though the voltage applied was higher. At applied voltage of 19 kV, the number of current filaments was 35.7 per half cycle at 1 LPM but the number reduced to 14.5 at 11.8 LPM. The reduction of current filaments in Ar is less sensitive to gas flow rate when compared to $N_2$. For example, the reduction was 20% for Ar flow rate that increased from 1 LPM to 12.5 LPM for all three gap widths investigated while in $N_2$, the reduction was steeper - 60% at flow rate increase from 1 to 11.8 LPM for 0.5mm gap, 80% at 1 to 9.4 LPM for 1.0 mm gap, and 45% at 1 to 4.4 LPM for 1.5mm gap.

**Table 4.1.** The duration of occurrence, $\Delta t$ per half cycle of positive current filaments for (a) Ar, 14 kVp-p (0.5 mm, 1.0 mm) and (b) $N_2$, 19 kVp-p (0.5mm, 1.0mm) DBD jets at various gas flow rate.

| Argon DBD jet (0.5 mm gap width) | | | | | | | | | |
|---|---|---|---|---|---|---|---|---|---|
| Gas flow / LPM | 0.9 | 1.8 | 2.8 | 3.9 | 5.1 | 6.5 | 8.3 | 10.2 | 12.5 |
| $\Delta t$ per half cycle / µs | 39.0 | 39.0 | 38.7 | 39.0 | 37.7 | 36.7 | 36.3 | 36.0 | 36.0 |
| Error in ( $\Delta t$) | 0.6 | 0.6 | 0.7 | 0.6 | 0.9 | 0.9 | 0.9 | 0.6 | 0.6 |
| Argon DBD jet (1.0 mm gap width) | | | | | | | | | |
| Gas flow / LPM | 0.9 | 1.8 | 2.8 | 3.9 | 5.1 | 6.5 | 8.3 | 10.2 | 12.5 |
| $\Delta t$ per half cycle / µs | 33.0 | 31.7 | 31.7 | 31.7 | 31.0 | 31.0 | 29.7 | 30.3 | 30.7 |
| Error in ( $\Delta t$) | 0.6 | 0.3 | 1.2 | 0.7 | 1.2 | 1.0 | 1.2 | 0.9 | 0.9 |

(a)

| $N_2$ DBD jet (0.5 mm gap width) | | | | | | | | |
|---|---|---|---|---|---|---|---|---|
| Gas flow / LPM | 1.0 | 2.0 | 3.2 | 4.4 | 5.8 | 7.4 | 9.4 | 11.8 |
| $\Delta t$ per half cycle / µs | 30.8 | 30.4 | 28.9 | 29.6 | 29.6 | 29.1 | 25.1 | 25.5 |
| Error in ( $\Delta t$) | 0.2 | 0.2 | 0.4 | 0.6 | 0.2 | 0.6 | 0.6 | 0.6 |
| $N_2$ DBD jet (1.0 mm gap width) | | | | | | | | |
| Gas flow / LPM | 1.0 | 2.0 | 3.2 | 4.4 | 5.8 | 7.4 | 9.4 | |
| $\Delta t$ per half cycle / µs | 22.4 | 22.8 | 22.4 | 23.2 | 22.5 | 22.1 | 19.9 | |
| Error in ( $\Delta t$) | 0.6 | 0.5 | 0.5 | 0.6 | 0.4 | 0.4 | 0.8 | |

(b)

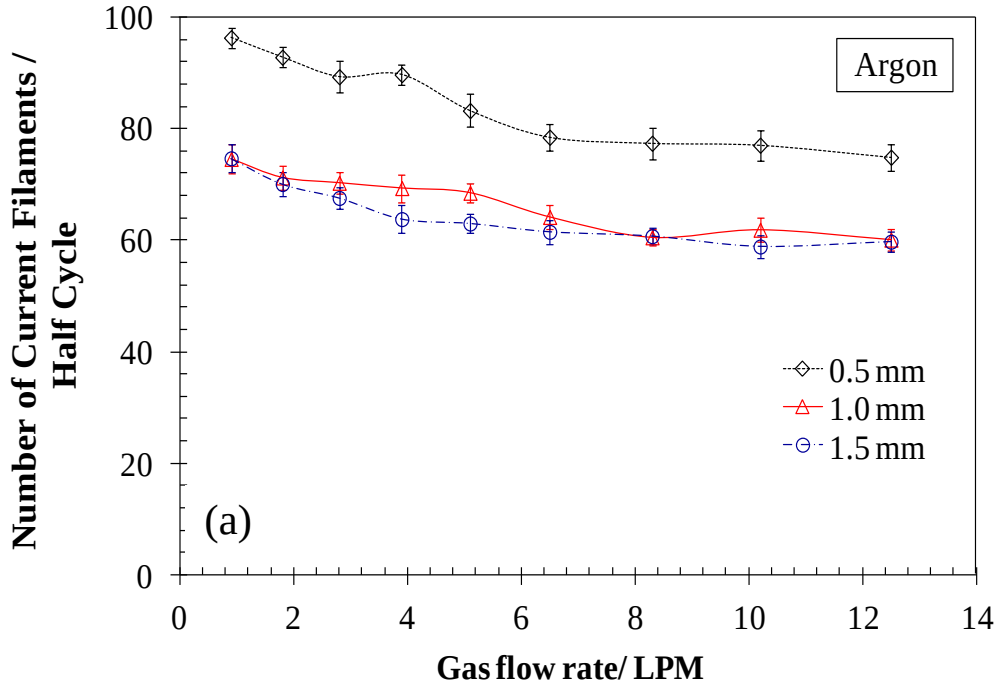


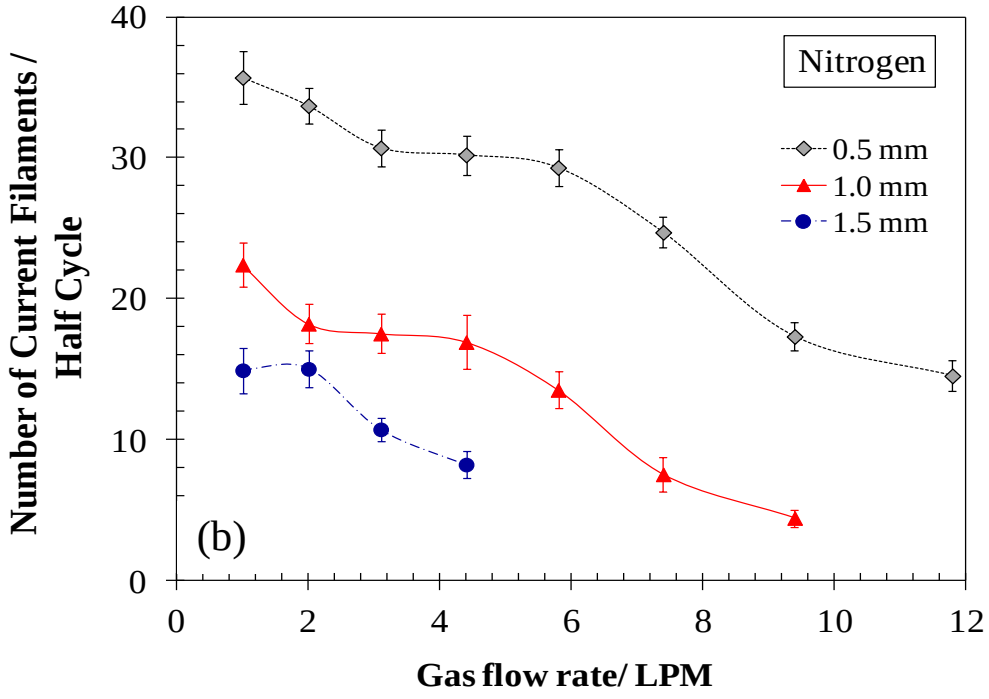


**Figure 4.12.** Variation of the number of positive current filaments per half cycle for (a) Ar, 14 kVp-p and (b) $N_2$, 19 kVp-p at 0.5 mm, 1.0 mm and 1.5 mm gap widths.

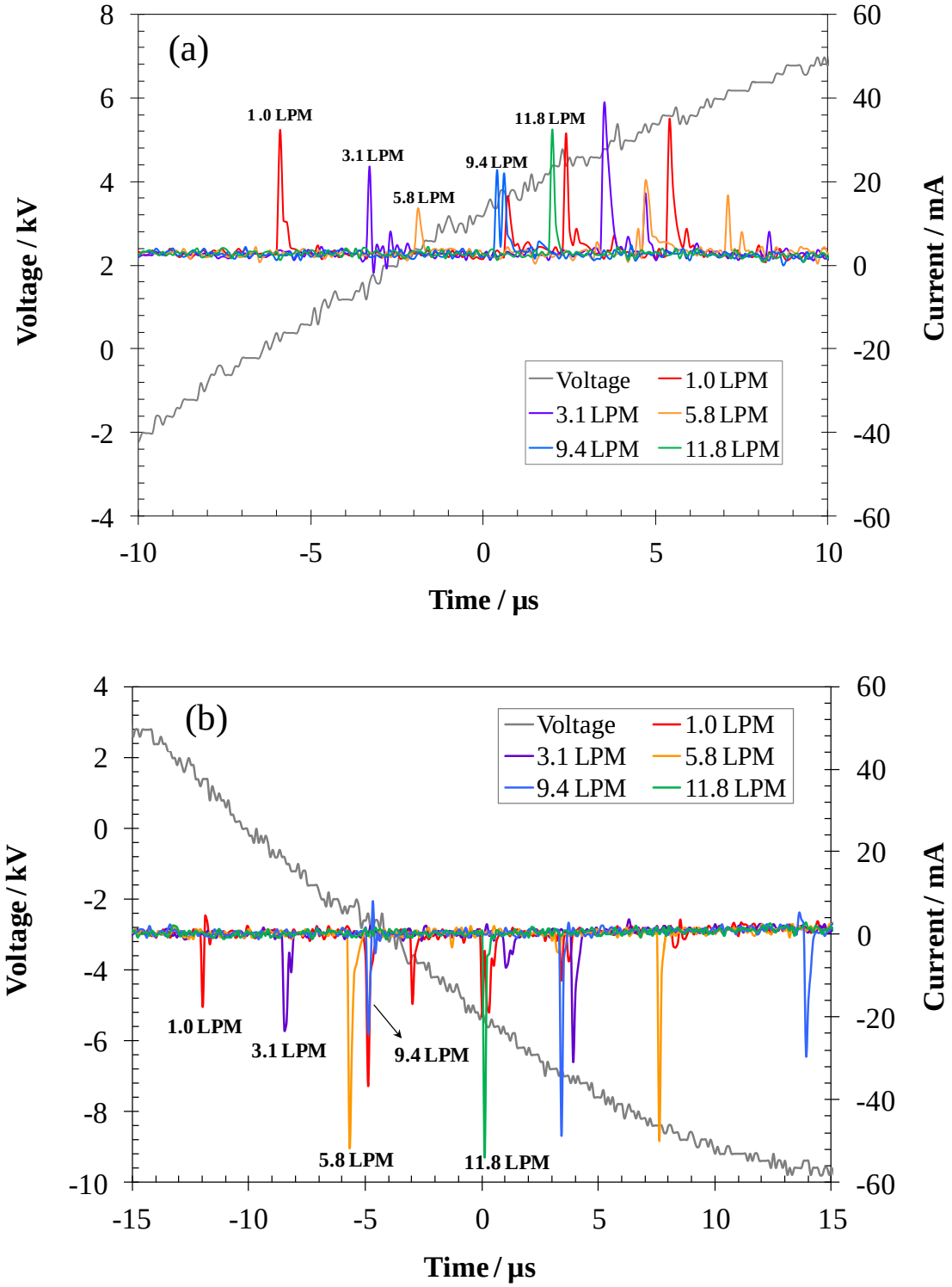


**Figure 4.13.** The occurrence of first current filament in $N_2$ at increasing gas flow rate for (a) positive and (b) negative polarity at 20 kVp-p.

The quantitative observation of the number of current filaments from Figs. 4.12 (a)-(b) revealed that smaller gap width produced more current filaments at constant applied voltage for both Ar and $N_2$ discharges. Ar discharge at 0.5 mm produced about 20% -

25% more current filaments than those obtained at 1.0 mm and 1.5 mm gaps. Likewise in $N_2$ discharge, about 40% - 70% more current filaments were produced at 0.5 mm than the 1.0 mm and 1.5 mm gap widths. At smaller gap width, the electric field strength between the electrodes is much higher, leading to enhancement of the ionization collision. Hence, the discharge ignited at lower voltage and the first current filament at each cycle occurred earlier than those at wider gap.

The study of applied voltage on the number of current filaments revealed increase in number when higher voltage was applied (Fig. 4.14). The duration of the current filaments formation, $\Delta t$, within half cycle (discharge phase) increases with applied voltage. Hence, more current filaments can occur. It is reasonable to say that the increase in applied voltage enhanced discharge conductivity of the DBD jet, leading to increase in the rates of electron impact ionization and other chemical reactions as well as the production of active species (radicals & excited states species). As a result, the density of the jet increases. This observation of increase in number of current filaments with voltage was also reported by (Zhang et al., 2010) using different types of dielectric barrier (PTFE & Epoxy).

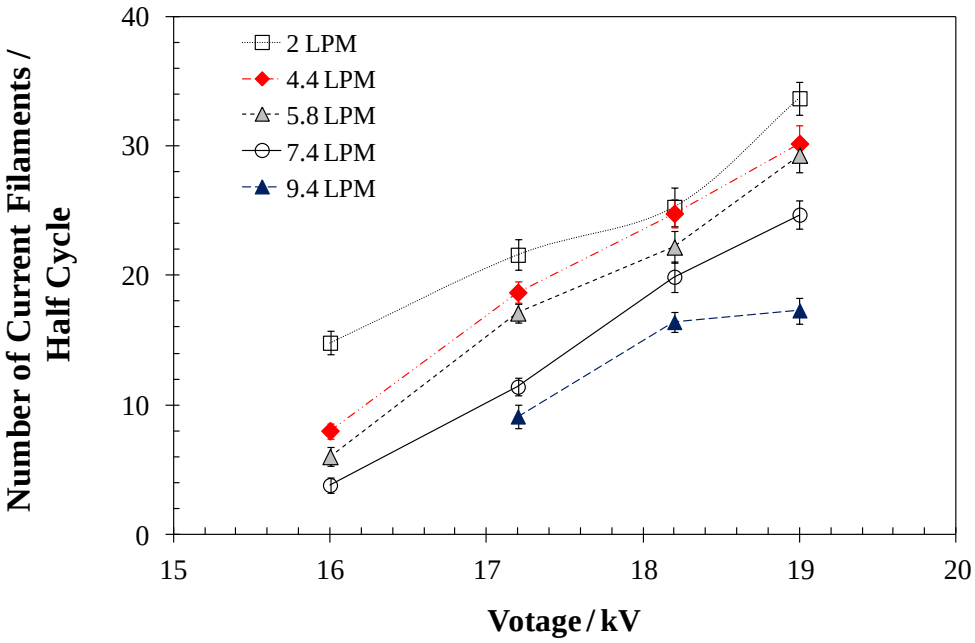


**Figure. 4.14** The number of positive current filament per half cycle against different voltage for $N_2$ discharge at 0.5 mm gap.

The total number of negative current filaments was not quantitatively counted as some of the negative current filaments consisted of superimposed multiple current filaments of 10-20 ns (FWHM), where one current filament can hardly be distinguished from the other (Fig. 4.15). The broadening of the width of this current filament may be due to the overlapping of multiple filaments and/or larger currents. This was also observed in $N_2$ discharge where the current filament obtained (not shown here) is similar to that shown in Fig. 4.15. Besides this, the time interval between consecutive broadened negative current filaments is larger compared to that for positive currents. Therefore, less negative "current peaks" was observed over the time frame of 10 μs for both Ar and $N_2$ discharges as portrayed in Figs. 4.10 (a)-(b).

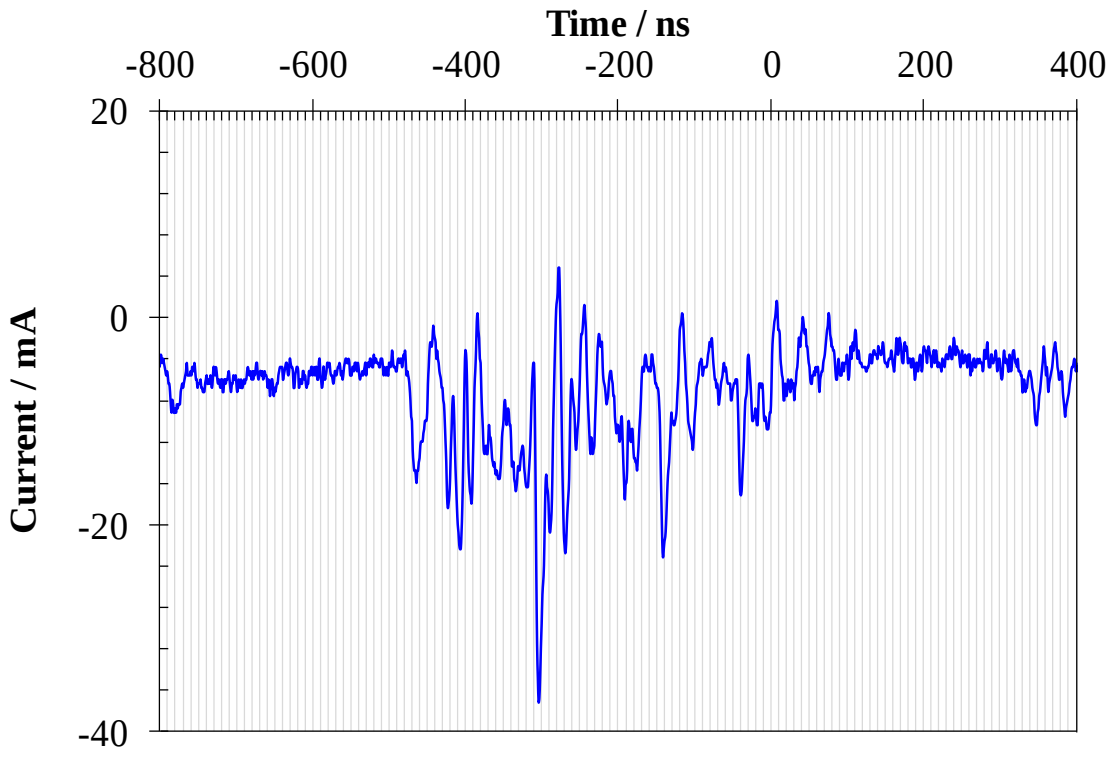


**Figure 4.15.** The enlarged negative current filament of Ar discharge at 3 LPM for 0.5 mm gap.

### 4.1.4 *Q-V* Lissajous Plots

DBD jet can be characterized through the study of charge transferred, energy deposited and power dissipated by the discharge between the electrodes. Influence of applied voltage, gas flow rate, gap width of different gas compositions (Ar, Ar:$N_2$ and $N_2$) on the charge transferred, energy deposited and power dissipated were studied based on *Q-V* Lissajous method.

#### 4.1.4.1 Influence of Applied H.V.

*Q-V* plots of Figs. 4.16 (a)-(c) show dependence on discharge voltage for Ar, $N_2$ and Ar:$N_2$ (47%:53%) at fixed gap of 0.5 mm with the flow rate of 6 LPM. The total charge transferred per half cycle monotonically, $\Delta Q_{1/2}$ deduced from these figures is given in Table 4.2. The charges transferred increases with discharge voltage corresponding to increase in number of current filaments built up across the electrodes at higher voltage. The prominent 'kink' on the top and bottom sides of the *Q-V* plot for Ar discharge corresponds to the 'lead' current spike in the positive and negative half-cycles of the current signal. It is obvious that by varying the discharge voltage, the *Q-V* parallelogram becomes significantly longer but not wider which is similar to the observation in (Manley, 1943). Therefore, the intercept of the left and right sides of the *Q-V* parallelogram with the horizontal axis which denote the breakdown voltage is almost constant as all conditions other than the discharge voltage were unchanged.

The total capacitance, $C_T$ when no charges were transported across the electrodes and dielectric capacitance, $C_d$, can be calculated from the *Q-V* plot obtained in Figs. 4.16 (a)-(c). $C_T$ calculated from *Q-V* plot is approximately 1.9 pF (± 0.2 pF), and agrees with that obtained when discharge was off (refer Fig. 3.9). Only the $C_d$ value deduced for Ar discharge (21.2 ± 2.7 pF) agrees with that computed from geometry, and $C_d$

deduced for $N_2$ discharge is 4.0 ± 0.6 pF (≈80% lower) whilst that for Ar:$N_2$ mixture is 5.0 ± 0.6 pF (≈76% lower). $C_d$ deduced from Figs. 4.16 (a)-(c) was almost constant at different applied voltage as $C_d$ is the physical property of the dielectric barrier and it depends on discharge area and gap distance. The discharge region in the *Q-V* plot where the gap is conducting can be considered to be equivalent to a configuration where both conductors are in direct contact with the dielectric. This condition was achieved in Ar discharge where the entire surface of the glass test tube in contact with Ar was observed to be covered in a corona glow (Fig. 4.17 (a)). *(To view the discharge inside the device, the copper end plate was replaced by a transparent plastic disc with a grounded copper disc of smaller diameter with a tube attached as the orifice.)* In contrast, $N_2$ discharge in Fig. 4.17 (b) shows a glow covering a much smaller area localized near the rounded end of the glass test tube resulting in a lower equivalent capacitance in $N_2$ discharge.

Though the charge transferred, $\Delta Q_{1/2}$ showed an increasing trend with applied voltage, the charges deposited on the dielectric would be independent of applied voltage. This is because not all the charges generated across the gap would be accumulated on the dielectric surface as some of the charges might be neutralized in the gap and some might have interacted with the surface charges on the dielectric and are neutralized (Jidenko et al., 2006).

The area enclosed by the *Q-V* parallelogram increases with discharge voltage. It follows that the mean energy deposited, and hence, the mean power dissipated per cycle in the discharge will increase proportionately with discharge voltage as shown in Fig. 4.18. Ar discharge can operate under lower voltage but with higher dissipated power. The dissipated power of Ar at 7.2 kVp-p is 1.22 W but this discharge voltage is insufficient to cause electrical breakdown in $N_2$ and Ar:$N_2$ gases. The higher the discharge voltage, the greater the power dissipated in the discharge under the same operating conditions for all the three gas compositions. This is correlated to the

increased number of current filaments at higher applied H.V. (Fig. 4.14) which dissipates more power. At fixed discharge voltage 12.4 kV, 0.5 mm gap and flow rate 3 LPM, the mean power dissipated in $N_2$ is 2.3% and in the mixture Ar:$N_2$ is 12% of that in Ar discharge. Production of charges through ionization collision is less complicated in atomic gas Ar in comparison to molecular gas $N_2$ in which more energy is required for dissociation of the molecules before direct or indirect ionization occurs.

Taking the input power to be equal to the rating of the transformer (36 VA) that drives the MOSFET and ignition coil, and the highest average power dissipated in Ar discharge estimated from the Lissajous plot to be equal to 7 W, the best efficiency of this DBD jet device is only 19%. This is low when compared to the RF excited Ar DBD in glow mode that achieved 90% as reported in (Li, Chen, & Liu, 2010).

**Table 4.2.** Measured total charge transferred per half cycle monotonically for 0.5 mm gap at 5 LPM flow rate.

| Ar | | Ar:$N_2$ | | $N_2$ | |
|---|---|---|---|---|---|
| Voltage / kVp-p | Charge / nC | Voltage / kVp-p | Charge / nC | Voltage / kVp-p | Charge / nC |
| 7.2 | 47 | 12.4 | 6 | 14.2 | 4 |
| 9.4 | 103 | 14.2 | 10 | 17.2 | 11 |
| 12.4 | 170 | 15.4 | 15 | 19.2 | 16 |

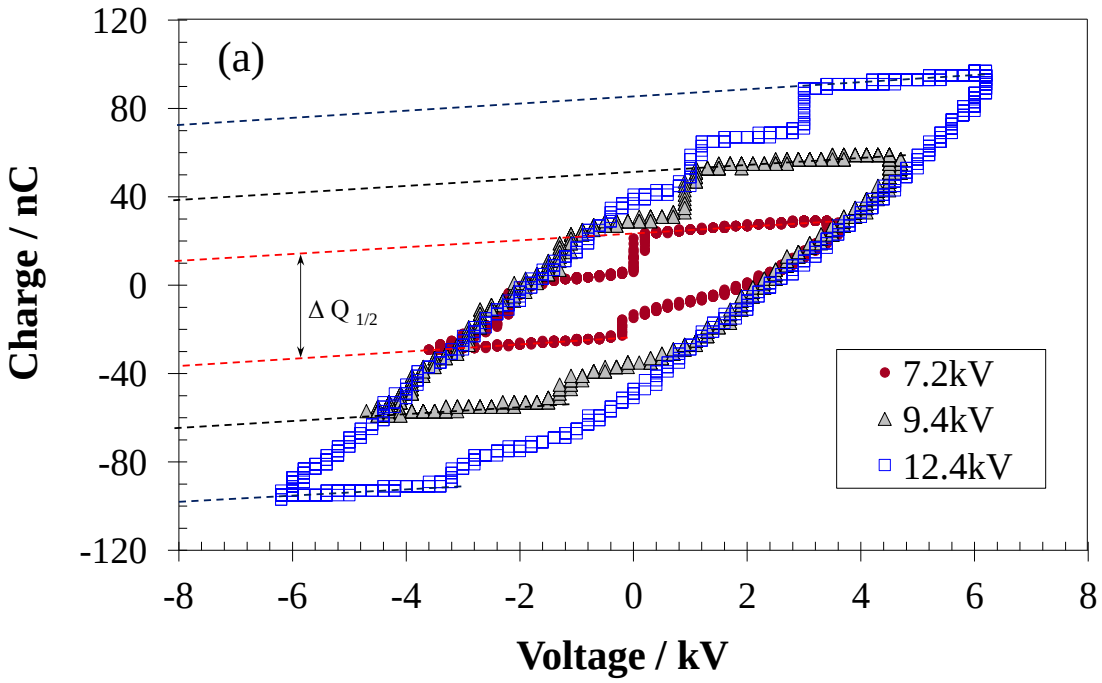
(a)
Charge / nC
Voltage / kV
ΔQ 1/2
7.2kV
9.4kV
12.4kV
120
80
40
0
-40
-80
-120
-8
-6
-4
-2
0
2
4
6
8

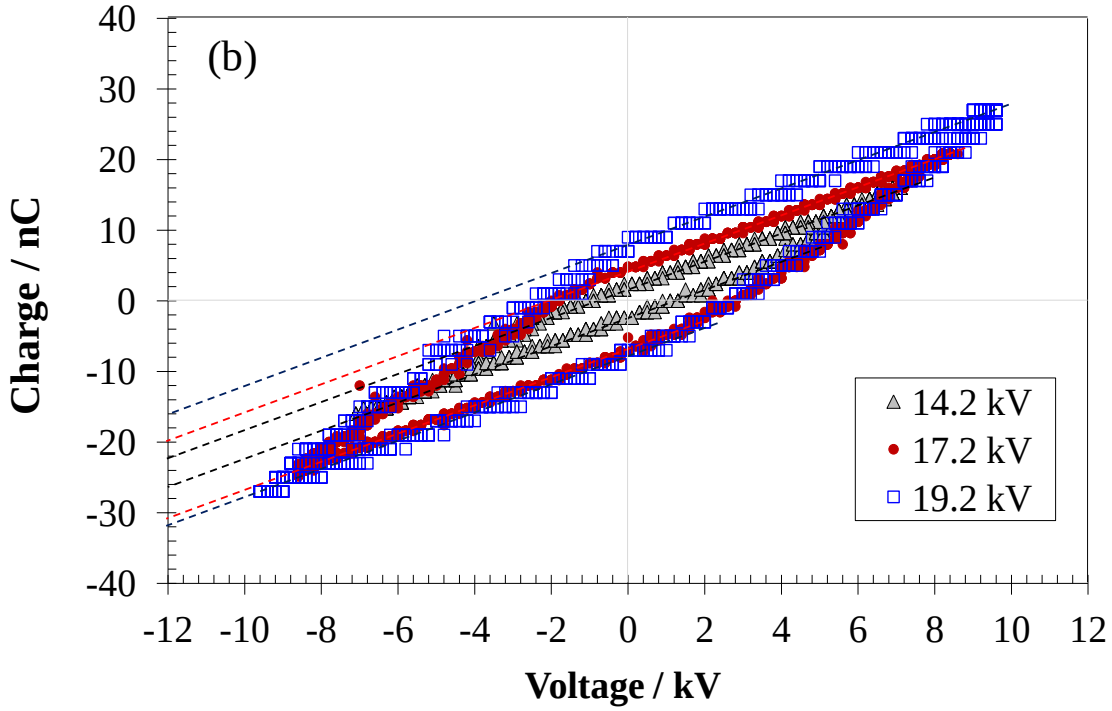
(b)
Charge / nC
Voltage / kV
14.2 kV
17.2 kV
19.2 kV
40
30
20
10
0
-10
-20
-30
-40
-12
-10
-8
-6
-4
-2
0
2
4
6
8
10
12

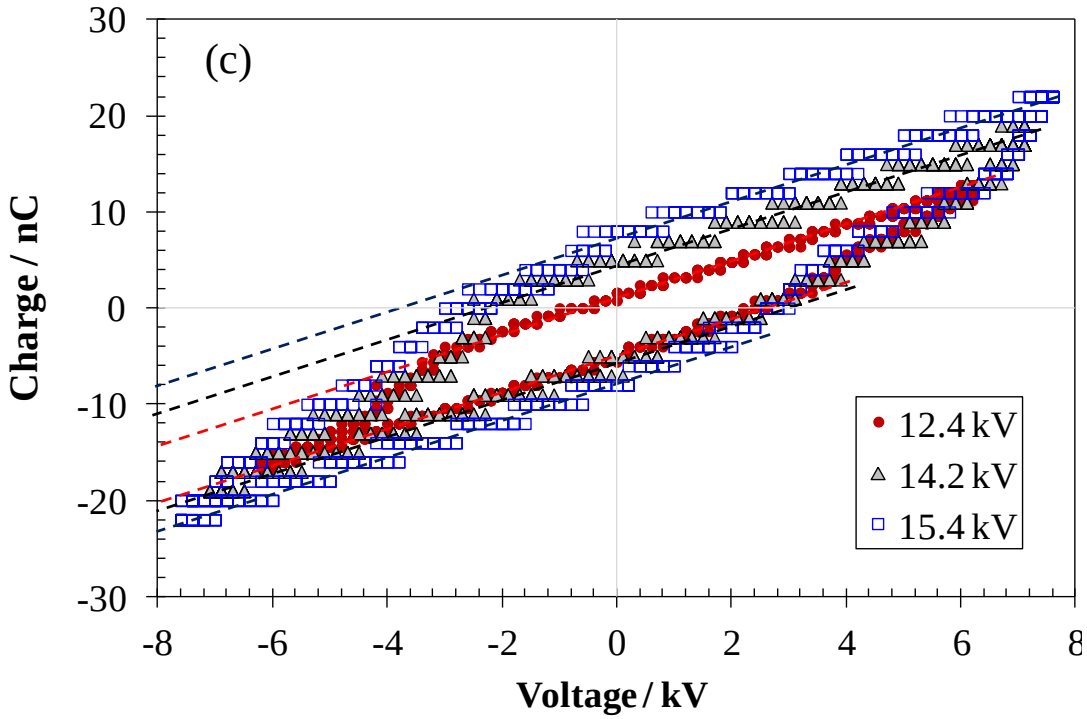


**Figure 4.16.** *Q-V* Lissajous plot for discharge in (a) Ar, (b) $N_2$ and (c) Ar:$N_2$ at 5 LPM with 0.5 mm gap at different voltage.

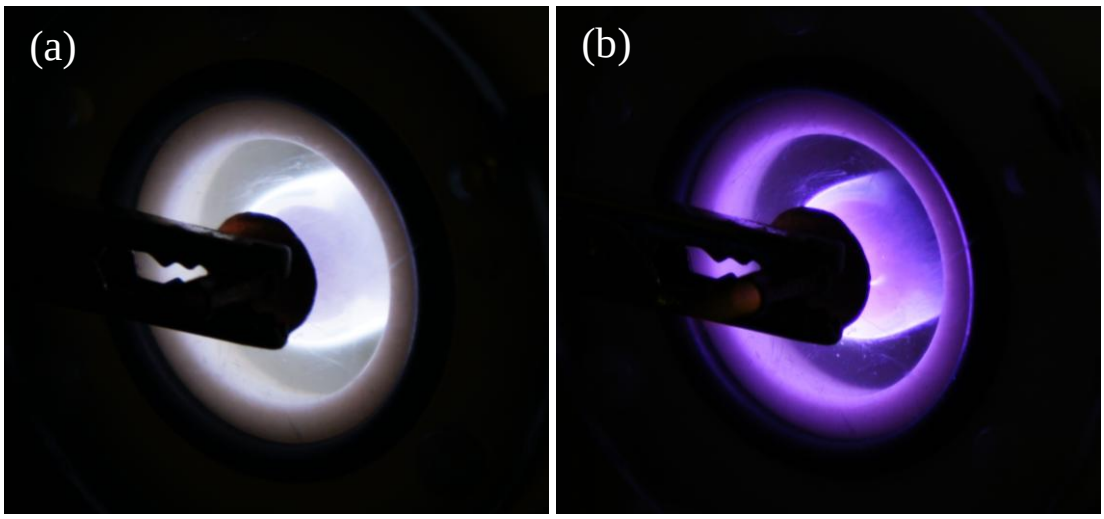


**Figure 4.17.** Glow covers the entire surface of the glass dielectric in (a) Ar discharge as compared to partial surface in (b) $N_2$ discharge. Camera settings: *f*/5.6, ISO 200, 0.5 s exposure time.

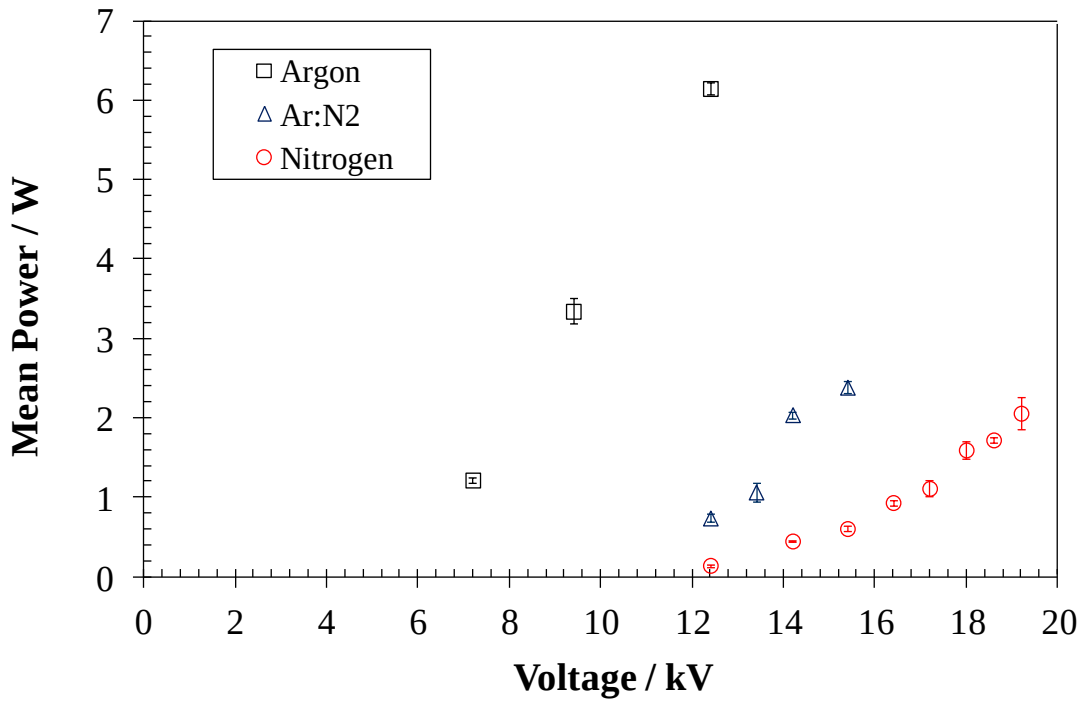


**Figure 4.18.** Mean power dissipated per cycle against various Vp-p at 0.5 mm gap, 3 LPM for Ar, Ar:$N_2$, and $N_2$ discharges.

### 4.1.4.2 Influence of Gas Flow

The mean power dissipated in a cycle (and also the mean energy) decreases with increase in flow rate for Ar:$N_2$ and $N_2$ discharges shown respectively in Figs. 4.19 (b) and 4.19 (c). As the micro-discharges/filaments become more difficult to ignite at higher pressures, the mean power dissipated decreases correspondingly in these two cases. Another factor is the increase in charges that escape through the exit hole to form the plasma jet at higher flow – this is evident as formation of longer jet (Figs. 4.22-4.24) and increase in net charges transported out (indicated by increase in potential of intercepting disc as shown in Fig. 4.27). However, for Ar discharge shown in Fig. 4.19 (a), it suggests that the gas flow rate is an independent parameter of the mean power dissipated per cycle. Though the pressure still builds up at higher flow rate in Ar, the over-voltage applied is comparatively at much higher level than the other two gas compositions and the corona glow still envelops the entire glass test tube surface. The

large surface area of charge deposition can act as a reservoir of charges and the amount of charges transported to the ground plate becomes relatively insignificant, resulting in its insensitivity to flow rate. This is reflected in the capacitance of the dielectric computed from the slope of *Q-V* plots for Ar discharge (Fig. 4.20) that did not change with flow rate where the amount of charges accumulated on the glass remains almost constant. The capacitance of the dielectric for Ar:$N_2$ and $N_2$ generally decreased with the increasing of gas flow rate where this trend is similar to the mean power dissipated shown in Figs. 4.19 (b) and 4.19 (c).

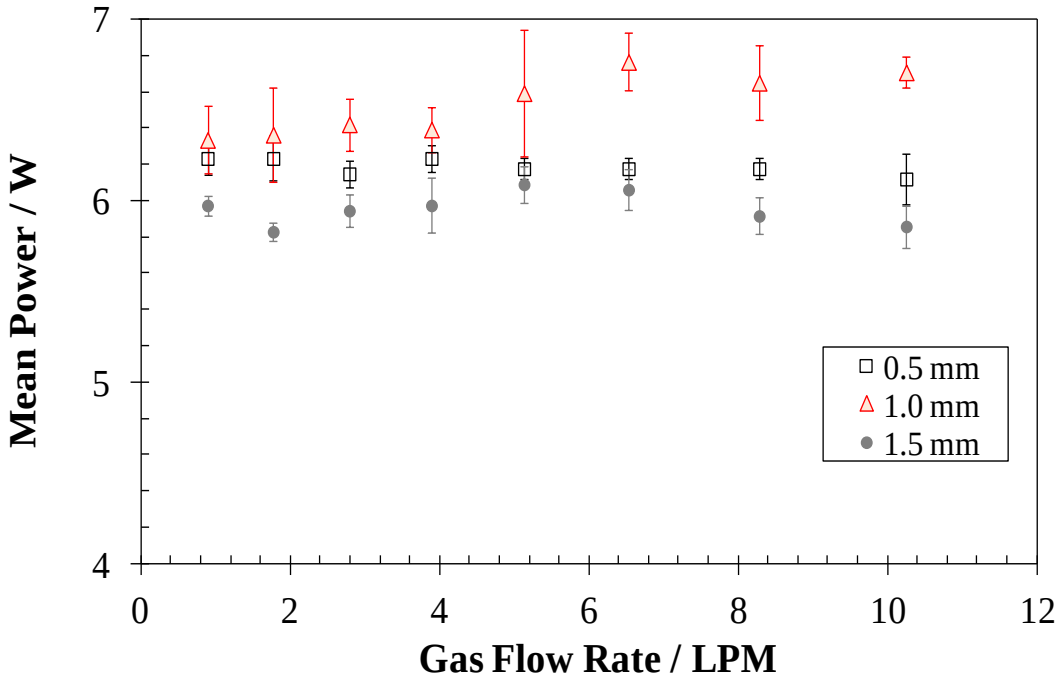


**Figure 4.19 (a).** Mean power dissipated per cycle against gas flow rate in Ar discharge at 12.4 kV for 0.5 mm, 1.0 mm and 1.5 mm gaps.

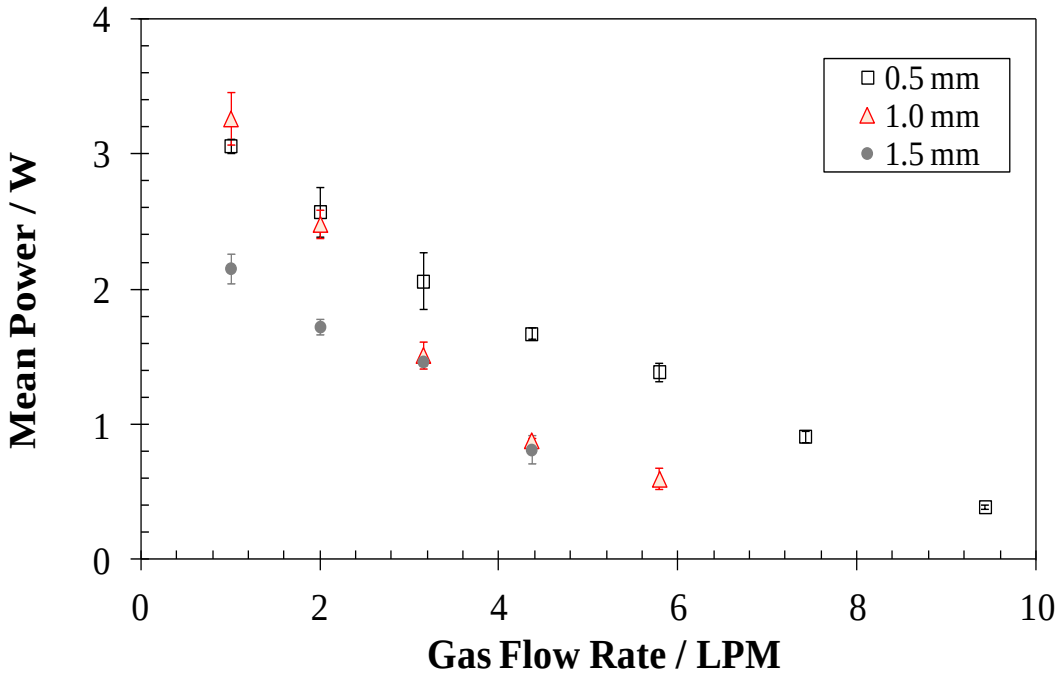


**Figure 4.19 (b).** Mean power dissipated per cycle against gas flow rate in $N_2$ discharge at 19.4 kV for 0.5 mm, 1.0 mm and 1.5 mm gaps.

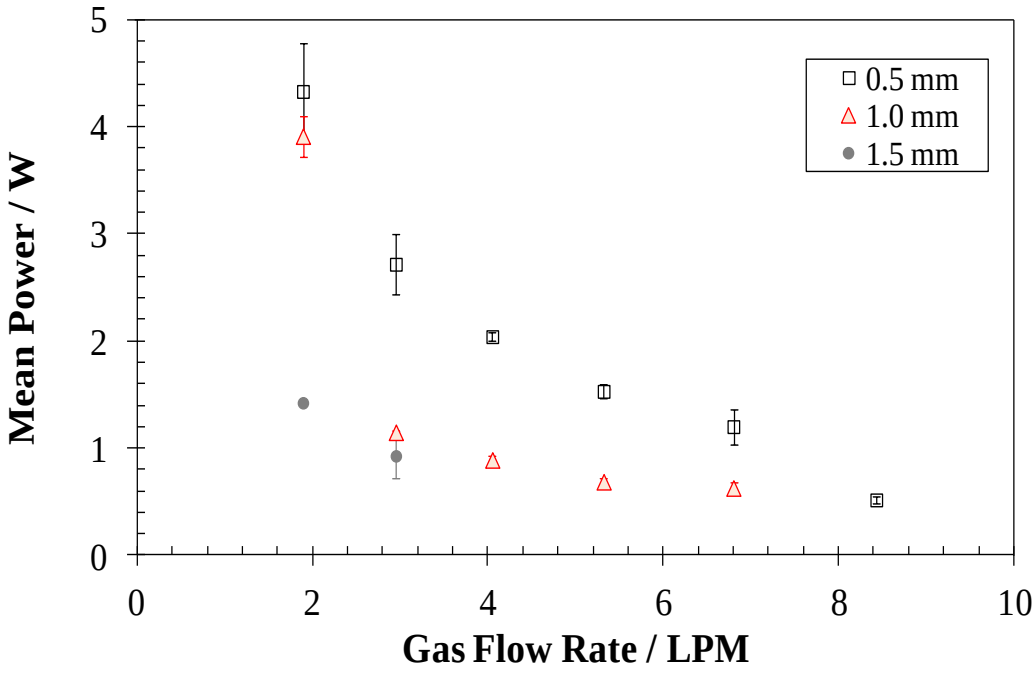


**Figure 4.19 (c).** Mean power dissipated per cycle against gas flow rate in Ar:$N_2$ discharge at 14.2 kV for 0.5 mm, 1.0 mm and 1.5 mm gaps.

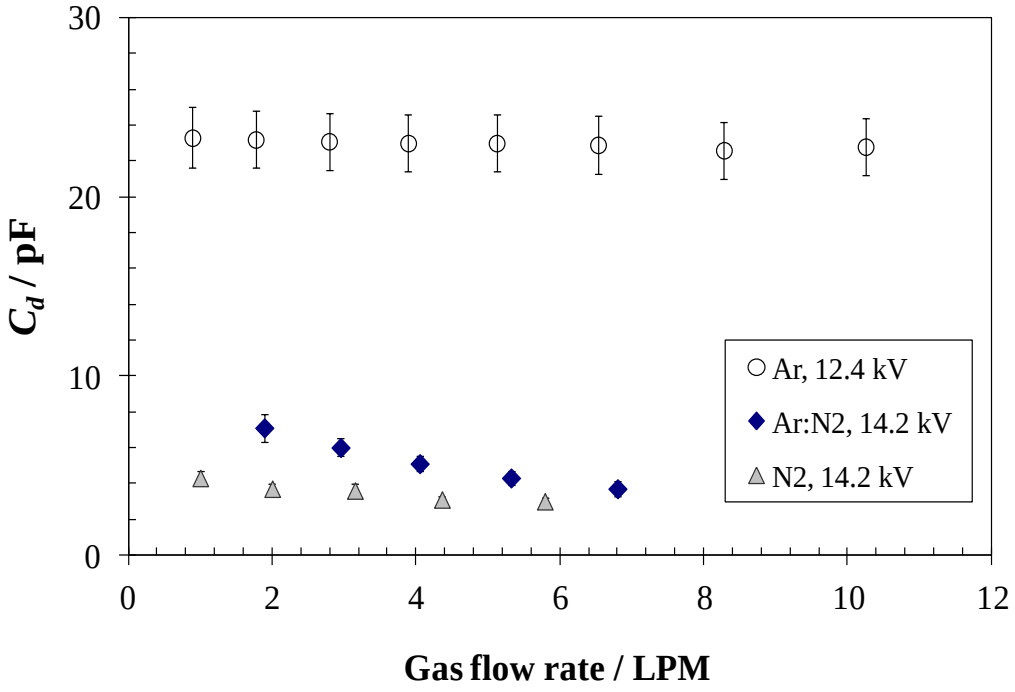


**Figure 4.20.** The variation of dielectric capacitance against gas flow rate deduced from *Q-V* plot for Ar, Ar:$N_2$ and $N_2$ discharges at 0.5 mm gap.

### 4.1.4.3 Influence of Gap Width

When the gap width increased from 0.5 mm to 1.5 mm, decrease in mean power dissipated was observed for both Ar:$N_2$ and $N_2$ discharges respectively in Figs. 4.19 (b)-(c). In the case of Ar discharge in Fig. 4.19 (a), mean power dissipated is highest at 1 mm gap and lowest at 1.5 mm gap but the range of variation is small when compared to that in Ar:$N_2$ and $N_2$ discharges. As mentioned in the preceding section, the large surface area for charge deposition in Ar resulted in its insensitivity to variation in gap width above.

The $C_d$ slope except for Ar, changes significantly for different gap widths. The *Q-V* plot of $N_2$ at 19 kV for 0.5 mm and 1.5 mm gaps is shown in Fig. 4.21. Slope of 0.5 mm gap was steeper than the slope of 1.5 mm gap, inferring that $C_d$ is greater at 0.5 mm gap. In the case of greater $C_d$ (narrower gap) for all the gas compositions, the discharge

consumes more power and charge transported was higher than the situation in wider gap. This result is consistent with the study of number of current filaments above where more current filaments can be obtained at lower gap width with lower ignition voltage.

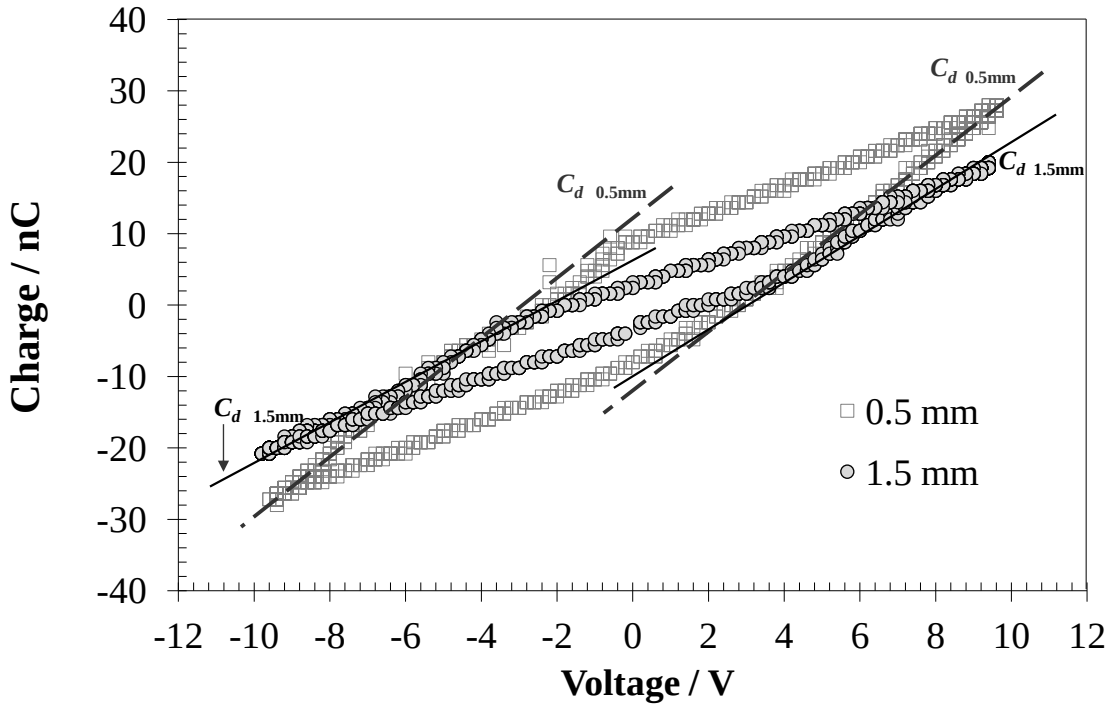


**Figure 4.21.** The slope of the dielectric capacitance of $N_2$ DBD jet at 0.5 mm and 1.5 mm gaps.

## 4.2 Physical Structure of the DBD Jet

Images of the plasma jets in the three gas compositions are shown in Figs. 4.22-4.24. The formation of the jet is due to expansion of the flux of charges that are transported through the nozzle which is similar to that in radio frequency expanding plasmas reported in (Dinescu & Ionita, 2008). The expansion is aided by the pressure gradient as the pressure in the inter-electrode space can build up to 2.5 bar at 12.5 LPM (in Ar), 2.3 bar at 12.7 LPM (in Ar:$N_2$) and 2.6 bar at 14.4 LPM (in $N_2$) due to the disparity in the size of the nozzle to the gas inlet, the ratio being 0.23. This can push the flow through the nozzle to subsonic speed. The brightness of the plasma jet is very low when

compared to the inter-electrode discharge. It is therefore reasonable to infer that most of the heat is dissipated in the inter-electrode discharge and very little is transferred to the effluent plasma (Lu et al., 2008). The high voltage region is also confined within the inter-electrode space, and hence, the effluent plasma jet can safely be applied to living tissues and heat-sensitive objects.

The dimension of the plasma jet is dependent on gas flow rate. The width is confined by the nozzle size, and it grows wider and longer when the gas flow rate was increased. The dimension of the jet is given in Table 4.3. The best jet (widest and longest) was obtained at highest gas flow and applied voltage for each of the gas compositions. It was found that the jet length increases very little in Ar:$N_2$ with the longest length measured to be 5.0 mm, compared to 6.0 mm and 6.2 mm for $N_2$ and Ar DBD jets respectively. The jet length generally increases but the increase was little even at high flow rate (flow speed at nozzle of > 100 m/s). The expansion of the gas at high speed through the nozzle could have resulted in very rapid mixing in small volume with the ambient air and hence, limiting the jet length (Teschke, Kedzierski, Finantu-Dinu, Korzec, & Engemann, 2005). In contrast, the plasma jets produced in gas flow 'guided' along dielectric and capillary tubes with very little or no constriction (under laminar mode) are longer as reported in (Zhang et al., 2006; Xiong et al., 2008).

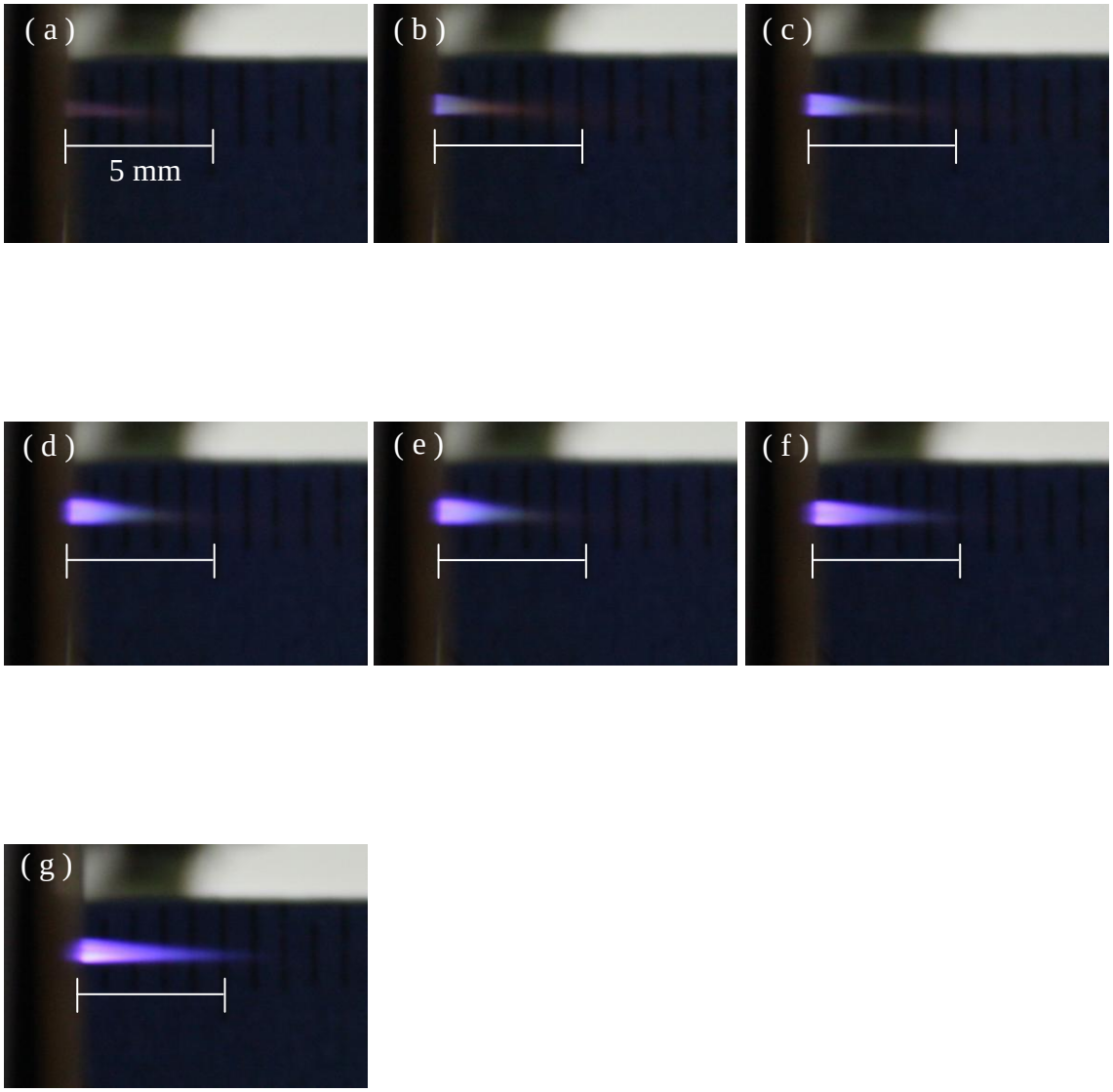


**Figure 4.22.** Images of plasma jet formed in $N_2$, 20 kVp-p at (a) 1 LPM, (b) 2 LPM, (c) 3.2 LPM, (d) 4.4 LPM, (e) 5.8 LPM, (f) 7.4 LPM and (g) 9.4 LPM. Camera settings: *f*/5.6, 4 s, ISO 400.

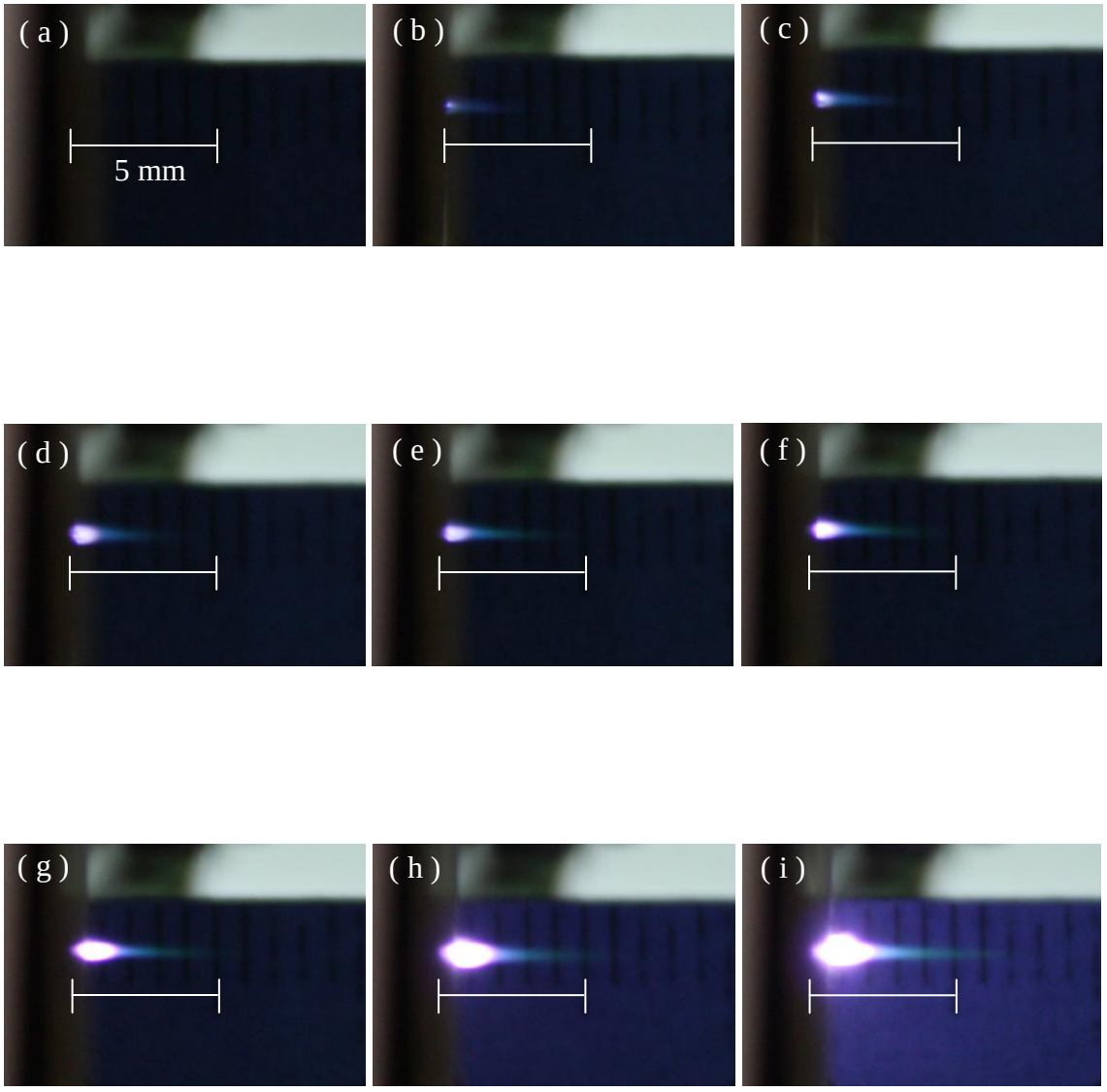


**Figure 4.23.** Images of plasma jet formed in Ar, 14 kVp-p at (a) 0.9 LPM, (b) 1.8 LPM, (c) 2.8 LPM, (d) 3.9 LPM, (e) 5.1 LPM, (f) 6.5 LPM and (g) 8.3 LPM, (h) 10.3 LPM and (i) 12.5 LPM. Camera settings: *f*/5.6, 4 s, ISO 400.

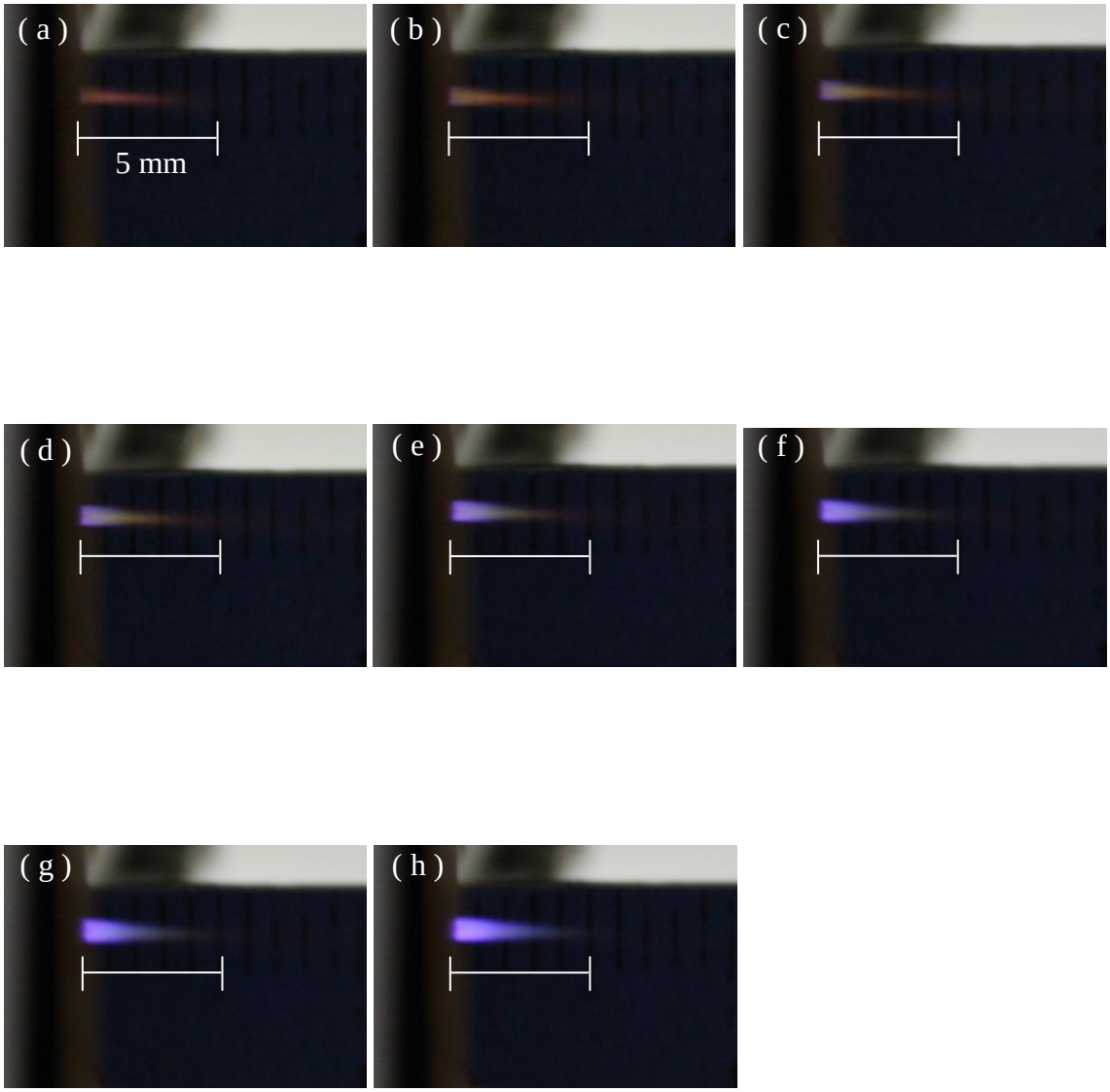


**Figure 4.24.** Images of plasma jet formed in Ar:$N_2$, 17 kVp-p at (a) 1.9 LPM, (b) 3.0 LPM, (c) 4.0 LPM, (d) 5.3 LPM, (e) 6.8 LPM, (f) 8.4 LPM, (g) 10.4 LPM, and (h) 12.7 LPM. Camera settings: *f*/5.6, 4 s, ISO 400.

**Table 4.3.** The dimensions of the jet for (a) Ar, 14 kVp-p, (b) $N_2$, 20 kVp-p and (c) Ar:N2, 17 kVp-p at 0.5 mm gap.

| (a) Ar ( 14 kVp-p) | | | | | | | | | |
|---|---|---|---|---|---|---|---|---|---|
| Gas flow / LPM | 0.9 | 1.8 | 2.8 | 3.9 | 5.1 | 6.5 | 8.3 | 10.3 | **12.5** |
| Width / mm | 0 | 0.4 | 0.7 | 0.9 | 0.9 | 0.9 | 1.1 | 1.3 | **1.4** |
| Length / mm | 0 | 2.0 | 2.8 | 3.0 | 3.7 | 4.0 | 5.0 | 5.2 | **6.2** |

| (b) $N_2$ ( 20 kVp-p) | | | | | | | | | |
|---|---|---|---|---|---|---|---|---|---|
| Gas flow / LPM | 1.0 | 2.0 | 3.2 | 4.4 | 5.8 | 7.4 | **9.4** | | |
| Width / mm | 0.4 | 0.7 | 0.9 | 1.1 | 1.1 | 1.1 | **1.1** | | |
| Length / mm | 3.0 | 3.7 | 4.0 | 4.1 | 4.3 | 5.0 | **6.0** | | |

| (c) Ar : $N_2$ ( 17 kVp-p) | | | | | | | | | |
|---|---|---|---|---|---|---|---|---|---|
| Gas flow / LPM | 1.9 | 3.0 | 4.1 | 5.3 | 6.8 | 8.4 | 10.4 | **12.7** | |
| Width / mm | 0.4 | 0.7 | 0.7 | 0.7 | 0.9 | 0.9 | 1.0 | **1.1** | |
| Length / mm | 3.0 | 4.0 | 4.0 | 4.5 | 4.5 | 4.8 | 4.8 | **5.0** | |

The length of DBD jet obtained in this work is in the millimetre range which is short compared to the atmospheric plasma plume presented by Laroussi et al. In their work, with high voltage pulses at repetition rates of 1-10 kHz applied between the electrodes and gas flow of 1-10 LPM, the plume length generated was able to reach up to several centimetres in the surrounding (Laroussi & Lu, 2005). These operating parameters are close to the parameters used in our system but the jet length obtained in our work was one order shorter, which is due to the design of our system that limits the jet length. Their electrodes were attached to a perforated glass disk where gas was flowing easily through it with little constriction/obstruction. In our setup (Fig. 3.1), the glass tube covered the electrode completely, and the small sized nozzle constricted the gas flow greatly, thus, limiting the jet length. To confirm the influence of constriction of the gas flow on the jet length, the copper end plate was replaced by a transparent plastic disc with a small grounded copper disc attached with a tube of diameter 2 mm which acted as the nozzle (Fig. 4.25 (a)). The $N_2$ jet length observed grew longer as shown in Fig. 4.25 (b). This agrees with the assumption of flow constriction that limits the jet

length mentioned above and strongly indicates that the flow rate and flow type are important factors for controlling the jet length.

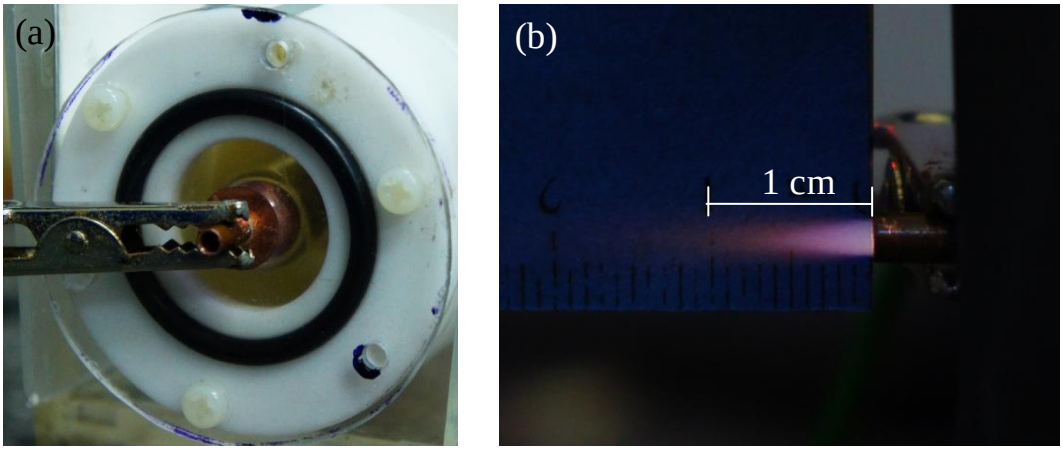


**Figure 4.25.** (a) The construction of DBD jet with bigger tube diameter and (b) the physical structure of the jet with bigger tube diameter.

The dependence of the applied voltage on the dimension of the jet is shown for $N_2$ jet at 7.4 LPM in Fig. 4.26. The width of the jet is 0.9 mm and did not grow when the peak-to-peak voltage increased from 15 kV to 20 kV. However, the jet length grew when the applied voltage was increased. The increase was gradual, reaching 4 mm at 15 kVp-p to 4.3 mm at 16 kVp-p, and attaining maximum length of 5 mm at 17.2 kVp-p. Further increase in the applied voltage above 17.2 kVp-p showed no further expansion in the jet length. This may suggest that the electrical energy supplied was used for the excitation of air molecules diffused into the jet as described by (Xiong et al., 2009). More excitation of air molecules would result in increase in the luminosity of the jet. The observed increase of the jet length at higher gas flow and applied voltage agrees with those studied by (Jiang et al., 2009; Xiong et al., 2009).

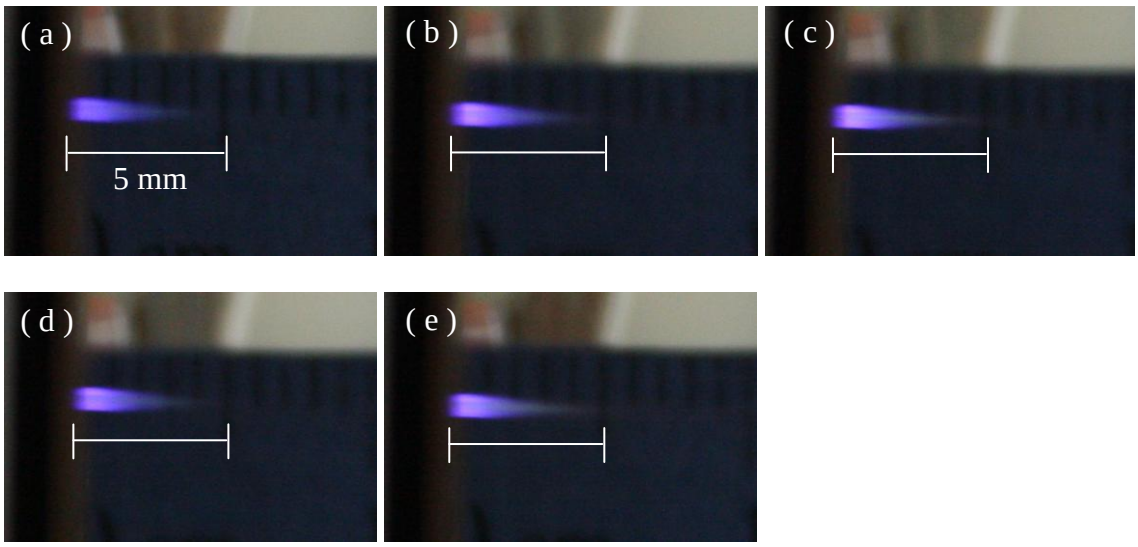


**Figure 4.26.** Images of plasma jet formed in $N_2$ at different Vp-p (a) 15 kVp-p, (b) 16 kVp-p, (c) 17.2 kVp-p, (d) 18.2 kVp-p, (e) 20 kVp-p. Camera settings: *f*/5.6, 4 s, ISO 400.

The brightness of the jet also increased with flow rate. As the luminosity can be indicative of plasma density, it is inferred that the plasma density increases with flow rate. Figs. 4.27 (a)-(b) shows the amount of net charges collected at different position of the jet increases with flow rate and it concurs with the inference above. Ar plasma jets display the highest charge density (brightest), especially at the region immediate to the nozzle, but adding Ar to $N_2$ in the proportion of 43%:57% did not improve the charge density in the plasma jet. Correlating to the current and mean power dissipated in DBD ignited in different gases, it is shown that stronger barrier discharge produces longer jet of higher charge density. Similarly, the jet also increases in length and intensity at higher applied voltage as larger amount of charges is dissipated in the gap, hence, more charges can be transferred into the jet stream.

Fig. 4.27 (a) shows the net charges transferred by the $N_2$ plasma jet are positive and decreases as the intercepting disc is placed further from the nozzle. In the case of $N_2$ DBD jet, the intercepting disc gets positively charged. This is probably because the heavier positive charges could stay along the jet direction while the lighter electrons get easily scattered away upon collision with heavier particles in the jet as well as ambient

air, hence resulting in a net positive charge on the disc. As the flow rate increases, the net charge on the disc increases but it decreases at further distance from the nozzle. In the case of Ar, especially at 2 mm from the nozzle (Fig. 4.27 (b)), negative DC voltage shift was recorded. On close inspection of Fig. 4.23, Ar DBD jet seems to be composed of 2 distinct regions of different luminosity, unlike the $N_2$ jet. There exists a central bright core immediate to the nozzle while a less luminous diffuse region surrounds it. The central bright core has width of approximately 0.2-1.0 mm and length 0.3-2.3 mm indicating a much higher plasma density (possibly a highly conducting column of current filament). At 2 mm, the metal disc is in contact with this bright core and many electrons of higher mobility reach it more rapidly, charging it negatively. At 4 mm and further, the disc is in contact with the diffuse region of the jet and the situation is similar to that in $N_2$ jet. However, the results above are not conclusive of the particle composition of the jet. Mericam-Bourdet et al. had applied an electric field perpendicular to the axis of the jet plume and the resulting deflection showed that the long plasma jet (up to 70 mm) in helium consisted of net negative charges (electrons and negatively charged ions such as $O_2^-$) (Mericam-Bourdet, Laroussi, Begum, & Karakas, 2009). However, this method could not be applied to our DBD jet as it is too short to show any observable deflection.

Relating the net charges transferred in the jet to the mean power dissipated per cycle in the DBD for $N_2$ shown in Fig. 4.19 (b), the reduction in mean power dissipated between the electrodes at higher flow rate seems to be translated to more charges being transported out of the nozzle. This is not obvious in the case of Ar plasma jet due to the comparatively large amount of charges dissipated in the gap.

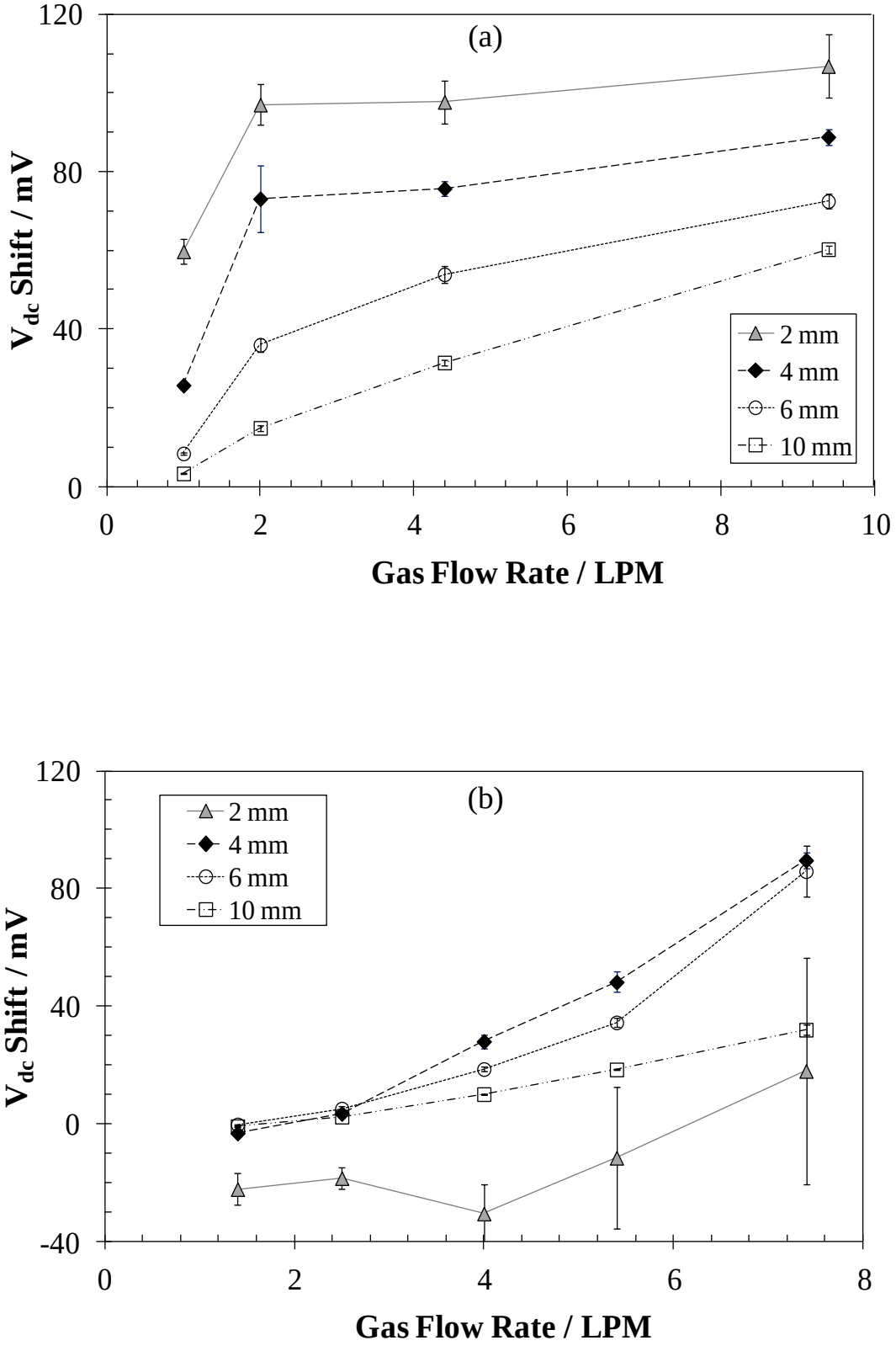


**Figure 4.27.** DC voltage shift measured by the intercepting disc versus flow rate at jet positions 2, 4, 6 and 10 mm for (a) $N_2$, 18.8 kVp-p and (b) Ar, 14.5 kVp-p discharges.

## 4.3 Optical Characteristics of the DBD Jet

The Ocean Optics HR 4000 and Avantes AvaSpec 3648 USB2 high resolution mini-spectrometers were employed for recording the emission spectra. The gas gap is fixed at 0.5 mm and the fibre tip is positioned 2.0 mm away from the hole of the grounded plate (refer Fig. 3.12). The applied voltage for Ar discharge is 14 kVp-p at resonance frequency of 8.5 kHz and for $N_2$ discharge it is 20 kVp-p at resonance frequency of 9.25 kHz.

### 4.3.1 $N_2$ Emission Spectra

From the emission spectra of the $N_2$ discharge obtained from HR 4000, the spectrum is dominated by the emission of second positive system (SPS) of $N_2$, which can be easily obtained for discharge in nitrogen or air. The $N_2$ SPS emission lines ranged from 268 nm to 546 nm (visible range), produced by $C^3\Pi u—B^3\Pi g$ transition. The transition is due to the excitation of vibrational and rotational states of $N_2$ SPS. Emission line with highest intensity was obtained at 337.13 nm. The emission lines between 300 nm to 440 nm are shown in Fig. 4.28. No emission was obtained in UV range lower than 300 nm. The identification of the $N_2$ SPS band heads were obtained from Table 29 in (Lofthus & Krupenie, 1977).

Besides the above mentioned $N_2$ SPS emission lines of higher intensity, numerous lines at higher wavelength (440 nm - 650 nm) with intensity less than 200 counts were detected when HR 4000 was employed as shown in Appendix Fig. B.1 (a)-(b). Those lines included atomic and ionic lines of oxygen (O I, O II, O III), ionic molecular $O_2^+$ lines and $N_2$ SPS lines (Pearse & Gaydon, 1976). The reactive atomic oxygen produced through the dissociation by electron collisions leads to the production of ozone, $O_3$, which is the typical reactive species found in atmospheric DBD and well known as

disinfecting agent. Ozone is unstable and it decomposes slowly back to oxygen molecule through collision with atomic oxygen and electron (Morgan, 2009). Ozone detector was not available to measure the amount of ozone present in the DBD jet but we could smell the odour of the ozone indicating the presence of ozone in the discharge. The atomic oxygen not only reacts with oxygen molecules to form ozone in a three body reaction, it can also play a major role in the surface treatment which will be discussed in the next chapter.

The first negative system of $N_2^+$ ( $B^2 \Sigma_u^+ - X^2 \Sigma_g^+$) can be obtained at the band head 391.4 nm. The intensity of this line is very weak compared to the strong $N_2$ SPS lines detected. This is expected in filamentary DBD where emission of $N_2^+$ usually occurs at low pressure.

The observation of the intensities of selected lines with gas flow rate was obtained and shown in Fig. 4.29. Three intense $N_2$ SPS lines were chosen for this study. The band heads of the selected lines are 337.13 nm, 357.69 nm and 380.49 nm. It is found that the intensity of these lines increase with gas flow rate. The increase is slow beyond 7.4 LPM for all three lines. The intensity of the jet is low at low flow rate as most of the particles are confined between the electrodes. As the flow rate was slowly increased, the discharge propagates out into the ambient air, excited and charged particles created during the discharge were flushed out of the nozzle resulting in the enhance of jet luminosity. The results from study of the physical structure of DBD jet are consistent with the results from study of emission intensity with various gas flow rate. It can be assumed that the particle density of the jet formed externally increases with increasing gas flow rate due to the higher production of the excited molecular nitrogen.

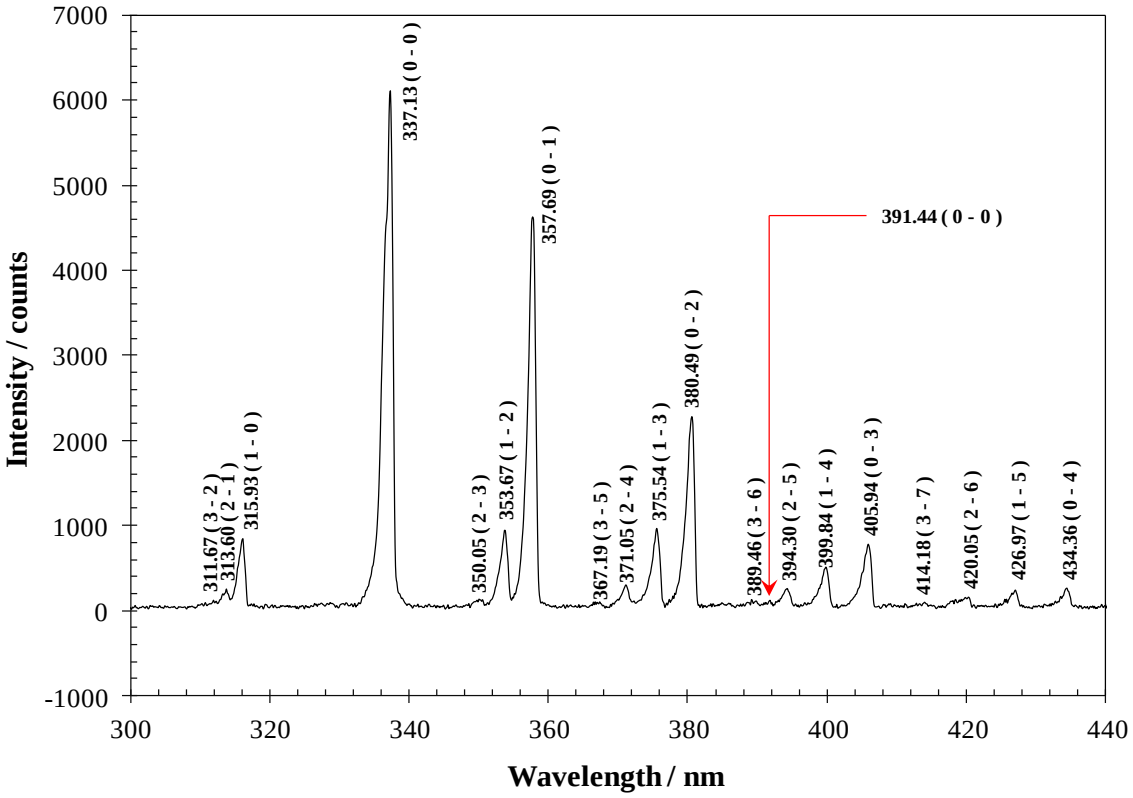


**Figure 4.28.** The emission spectrum of $N_2$ SPS in the region from 300 nm - 440 nm at flow rate of 6 LPM. Numbers in the bracket (v-v') denote the vibrational transitions where v is upper electronic states and v' is lower electronic states. Spectrometer was set at 200 ms integration time.

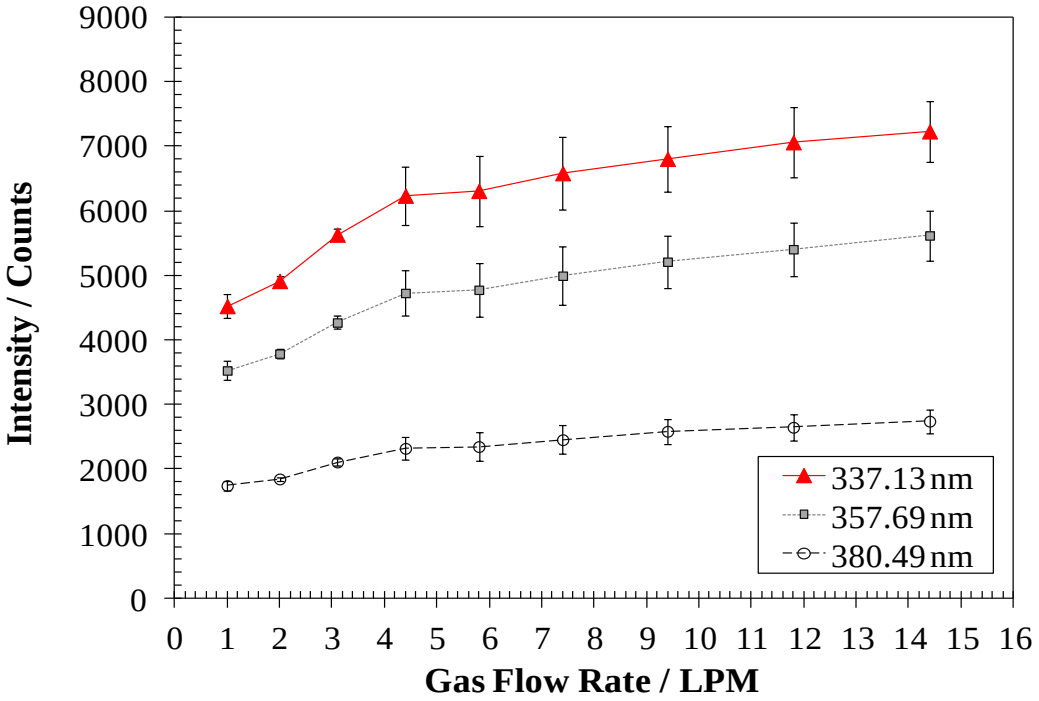


**Figure 4.29.** Intensity of $N_2$ SPS emission lines (337.13 nm, 357.69 nm and 380.49 nm) as a function of $N_2$ gas flow rate at applied voltage of 20 kVp-p and 0.5 mm gap width.

The optical emission of $N_2$ DBD jet for wavelength range 650 nm - 1000 nm is depicted in Fig. 4.30. The intensity within this range is weak. The $N_2$ first positive system (FPS, $B^3\Pi_g - A^3\Sigma_u^+$) and the Herman's IR system dominated at this range. The atomic O and N (obscured by the $N_2$ molecular systems above) can be obtained when the nitrogen and oxygen molecules were dissociated by energetic electrons during the discharge. Presence of atomic oxygen in $N_2$ discharge is possible due to $O_2$ in ambient air mixing with the atmospheric discharge jet stream.

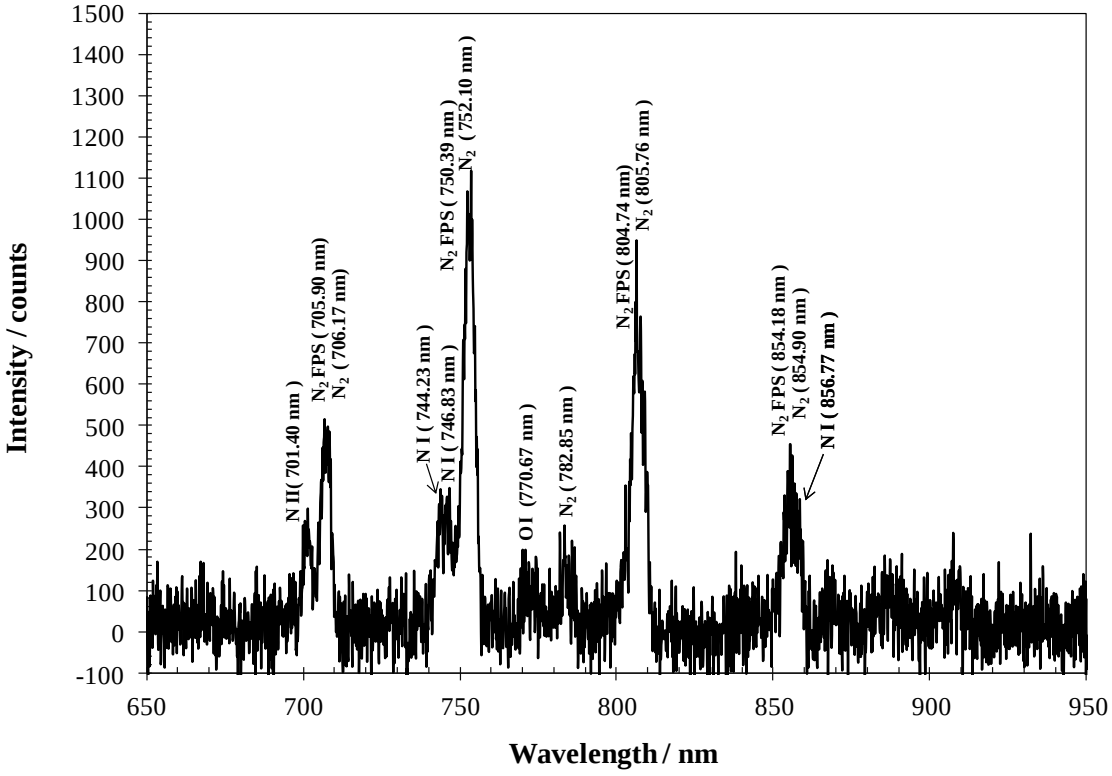


**Figure 4.30.** The emission spectra of $N_2$ DBD jet for 650 nm - 950 nm range at flow rate of 6 LPM. The first positive system (FPS) and Herman's IR system in $N_2$ are observed. Spectrometer was set at 200 ms integration time.

### 4.3.2 Ar Emission Spectra

In Ar DBD jet, the emission spectrum obtained for the range 650 nm - 1000 nm is dominated by Ar atomic lines from transition 4p → 4s as shown in Fig. 4.31. These lines were either the atomic Ar I or ionic Ar II. In Ar discharge, energetic electrons make collisions with the atomic Ar in the ground state and the ground state Ar can be ionized or excited to higher state. The excited state Ar will return to ground state or lower excited state by emitting photon. Possible reactions that occur can be described as follows (Wagenaars, Brandenburg, Brok, Bowden, & Wagner, 2006):

$$Ar + e \rightarrow Ar^{+} + 2e \quad \text{-------- Ionization}$$

$$\left.\begin{array}{l} Ar + e \rightarrow Ar^{*} + e \\ Ar + e \rightarrow Ar^{**} + e \end{array}\right\} \text{ Excitation}$$

$$\left.\begin{array}{l} Ar^{*} \rightarrow Ar + h\nu \\ Ar^{**} \rightarrow Ar^{*} + h\nu \end{array}\right\} \text{ Relaxation}$$

Additionally, weak emission of O radical was obtained at 777.4 nm, showing the diffusion of $O_2$ in the atmospheric air into the Ar jet stream.

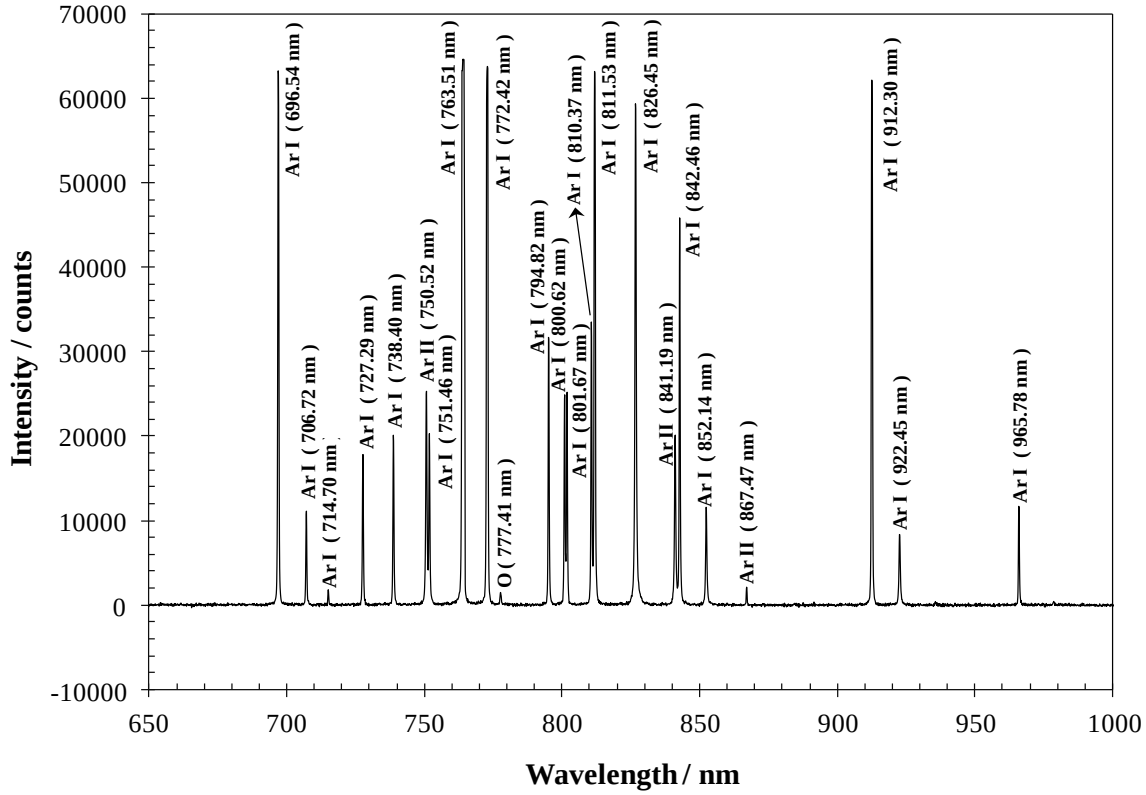


**Figure 4.31.** The emission spectra of Ar DBD jet in the region from 650 nm - 1000 nm at corrected flow of 6 LPM.

Fig. 4.32 depicts the spectrum of Ar discharge measured from HR 4000 spectrometer in UV range. Atomic Ar I and ionic Ar II lines at shorter wavelength (320 nm - 420 nm) are identified but the intensity is very low. The wavelength of all the atomic and ionic Ar lines detected and its configurations are shown in Table B.1 in Appendix. Besides that, the spectrum from HR 4000 revealed the existence of excited $N_2$ SPS and OH band (transition $A^2\Sigma^+$ (v=0) $\rightarrow X^2\ \Pi$ (v=0)). Two peaks of OH band in Ar discharge were observed at 307.8 nm ($Q_2$) and 308.9 nm ($Q_1$). Both are (0, 0) transition. In the $N_2$ discharge, the OH peaks was not detected. The OH band is probably due to the impurity (3 ppm moisture) in the gas where the reaction is given as follows (Xiong, Nikiforov, Lu, & Leys, 2010):

$$H_2O + e \rightarrow OH + H + e$$

$$H2O + Ar^* \rightarrow OH + H + Ar$$

The emission spectrum of Ar DBD jet which was dominated by Ar (4p→4s & 5p→4s ), $N_2$ SPS and OH bands was similar to that reported in open air argon plasma plume by Xiong et al.(Xiong et al., 2010) and room temperature atmospheric argon plasma jet by Walsh et al. (Walsh & Kong, 2007)

The variation of the intensity of Ar DBD jet with gas flow rate is depicted in Fig. 4.33. Five intense Ar I lines 772.42 nm, 811.53 nm, 826.45 nm, 842.46 nm and 912.30 nm were selected for this study. The analysis can be separated into three regions: low gas flow region (1 LPM - 4 LPM), moderate gas flow region (4 LPM - 9.5 LPM), and high gas flow region (9.5 LPM - 12 LPM). For the low gas flow region, the intensity generally increases, showing the increase of excited atomic Ar. The increase slowed down and became quite constant or decreased slightly from 4 LPM - 9.5 LPM. Further increase in the gas flow rate resulted in a decrease of intensity for all the selected Ar lines. At high gas flow region, the jet extended longer into the surrounding air, which causes the nitrogen molecules or oxygen molecules in the air to diffuse into the jet stream and the excited Ar species were quenched by the $N_2$ or $O_2$ during the interaction. The concentration of atomic Ar decreases due to the electron attachment by oxygen which has electronegative behaviour, hence, the intensity of Ar lines was reduced. This is consistent with the physical structure of the Ar DBD jet as discussed in the previous section. The jet appeared very bright at the exit of the nozzle (district bright core region) but the luminosity reduced at regions further away from the nozzle, probably due to the quenching process by the molecules in the air and restricted the growth of jet length.

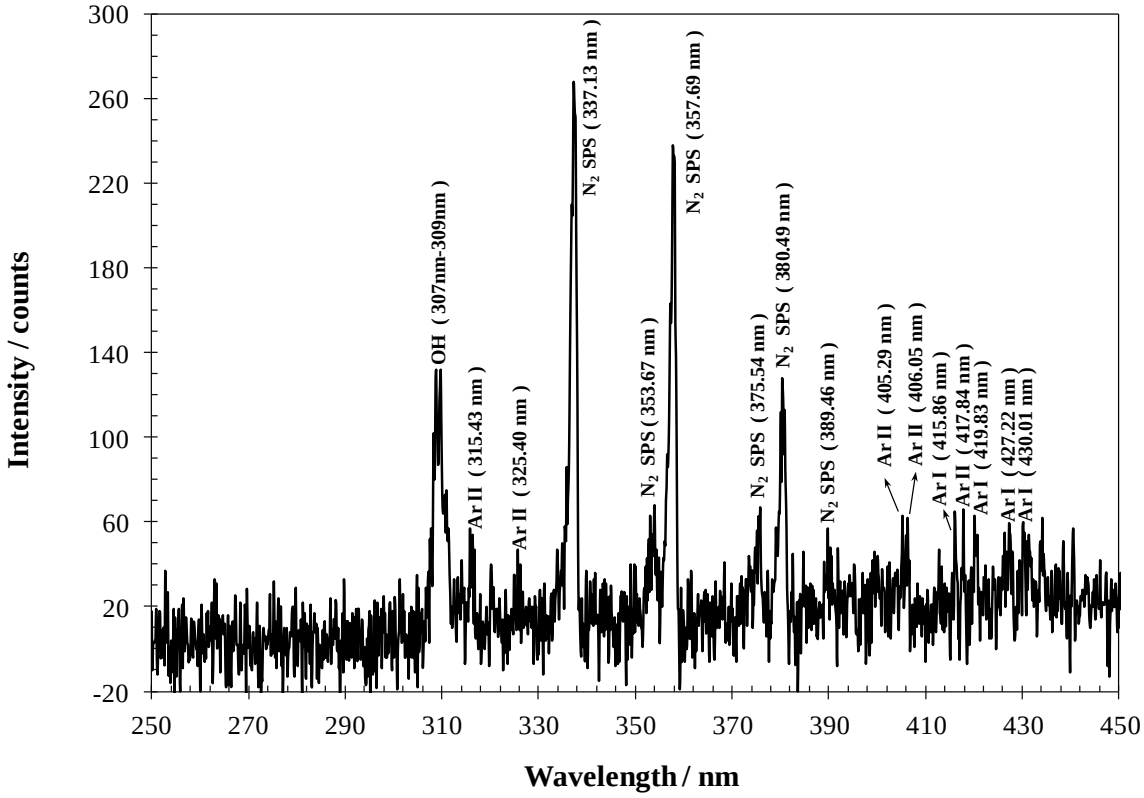


**Figure 4.32.** The emission spectra of Ar DBD jet in the region of 250 nm - 450 nm at flow rate of 6 LPM.

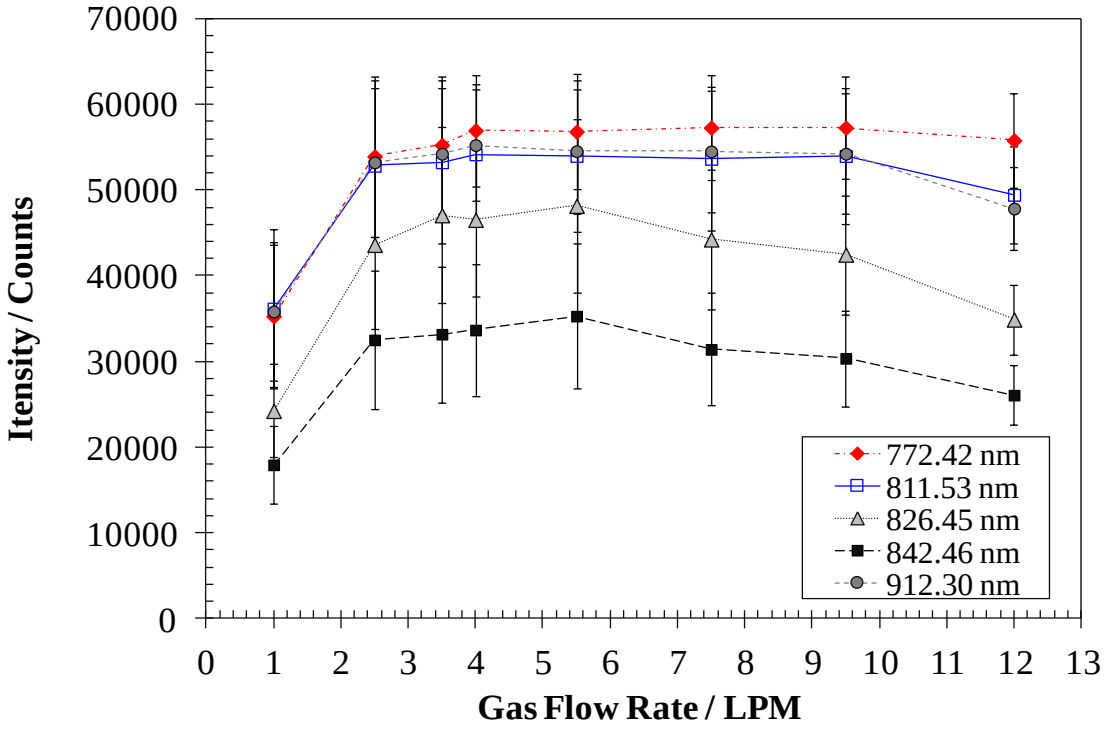


**Figure 4.33.** Intensity of atomic Ar lines (772.42 nm, 811.53 nm and 826.45 nm, 842.46 nm, 912.30 nm) as a function of Ar gas flow rate at applied voltage of 14 kVp-p and 0.5 mm gap width.

# CHAPTER 5

## Surface Treatment

DBD jet treatment on Mylar film was carried out by examining the influence of different types of gases and the duration of treatment time to obtain a better understanding of the relationships between the operating parameters and treated sample. These relationships will allow optimization of the operating parameters chosen for surface treatment under atmospheric pressure.

### 5.1 Influence of Treatment Time

The pictures of the changes of water droplet on the treated and untreated Mylar film with various treatment time are shown in Figs. 5.1 (a)-(g) for $N_2$ DBD jet and Figs. 5.2 (a)-(g) for Ar DBD jet. The $N_2$ and Ar flow rate were fixed at (6.0 ± 0.2) LPM while the peak-to-peak voltage for $N_2$ is 20 kV and for Ar is 14.4 kV. Contact angles for the treated films compared to the contact angles of untreated films were measured and reduction of contact angles was observed as treatment time increases. The contact angle for the control conditions when the discharge is not ignited without gas flow is (73.3 ± 0.3)° and (73.7 ± 0.5)° for $N_2$ gas and Ar gas respectively while with gas flow is about (73 ± 0.6)° for $N_2$ gas and (73.5 ± 0.4)° for Ar gas. Contact angles at both conditions did not show a significant difference, which means the bombardment of the neutral gas particles on the surface is unable to modify the Mylar surface. The surface adhesion of this Mylar film before being treated is poor as the contact angle is large, indicating surface energy is low.

After 15 s of treatment, the contact angle is found to reduce to about 50% of that before treatment for both $N_2$ and Ar DBD jets. 60% in reduction of contact angle was achieved if the treatment time was prolonged until 120 s for $N_2$ and Ar DBD jets. The contact angle of various treatment times for $N_2$ and Ar treatment is presented in Table 5.1 and plotted in Fig. 5.3. The contact angle does not reduce significantly for treatment time longer than 30 s and seems to stabilize/saturate for both $N_2$ and Ar jet treatment. The further increase of the treatment time with no further surface modification was also observed by Borcia et al. on different kinds of polymer samples (Borcia et al., 2004). The reduction of contact angle revealed that the surface wettability is increased after the plasma treatment. It is obvious that $N_2$ & Ar DBD jets are able to increase the hydrophilicity of the Mylar surface, that is, surface wetting and adhesion was improved.

**Table 5.1.** Contact angle of 2 µl water droplet on Mylar sheet at different treatment time with peak-to-peak voltage of (a) 20 kV for $N_2$ and (b) 14 kV for Ar DBD jets.

| Treatment Time / s | Contact Angle / ° | Error / ± ° | % in Reduction |
|---|---|---|---|
| 0 | 73.3° | 0.3 | 0 |
| 15 | 34.2° | 0.2 | 53.3 |
| 30 | 31.0° | 0.6 | 57.7 |
| 60 | 30.4° | 0.7 | 58.5 |
| 90 | 29.4° | 0.6 | 59.9 |
| 120 | 28.4° | 0.3 | 61.3 |

(a)

| Treatment Time / s | Contact Angle / ° | Error / ± ° | % in Reduction |
|---|---|---|---|
| 0 | 73.7° | 0.5 | 0 |
| 15 | 35.8° | 0.3 | 51.3 |
| 30 | 33.0° | 0.2 | 55.3 |
| 60 | 32.6° | 0.2 | 55.8 |
| 90 | 31.0° | 0.2 | 58.0 |
| 120 | 29.8° | 0.4 | 59.5 |

(b)

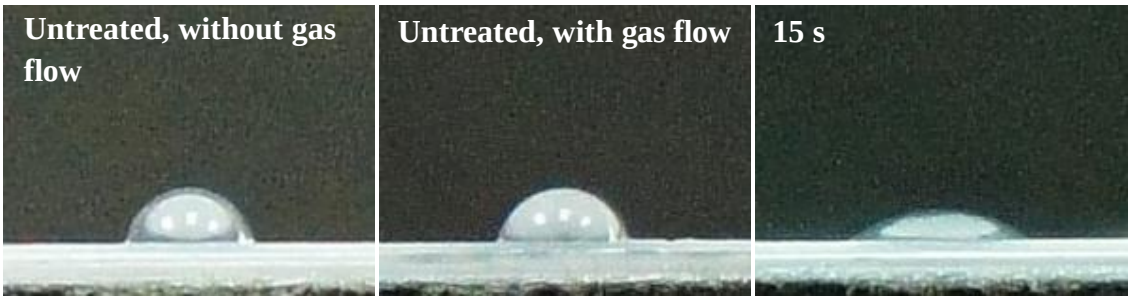


(a) (b) (c)


(d) (e) (f)


(g)

**Figure 5.1 (a)-(g).** Water droplet on untreated and treated Mylar film by $N_2$ DBD jet at 20 kVp-p, gas flow rate of 6 LPM for various treatment times.

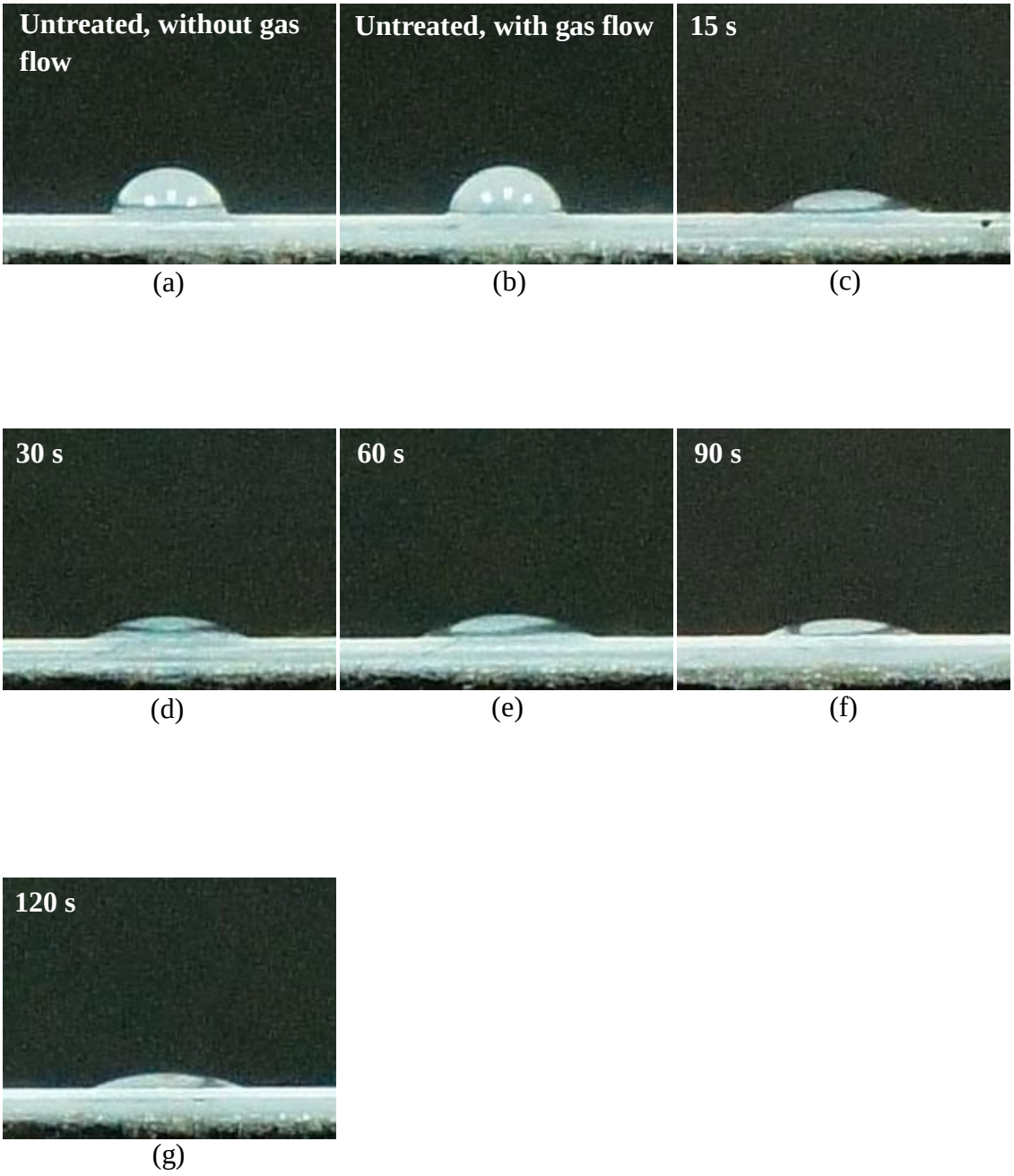


**Figure 5.2 (a)-(g).** Water droplet on untreated and treated Mylar film by Ar DBD jet at 14.4 kVp-p, gas flow rate of 6 LPM for various treatment times.

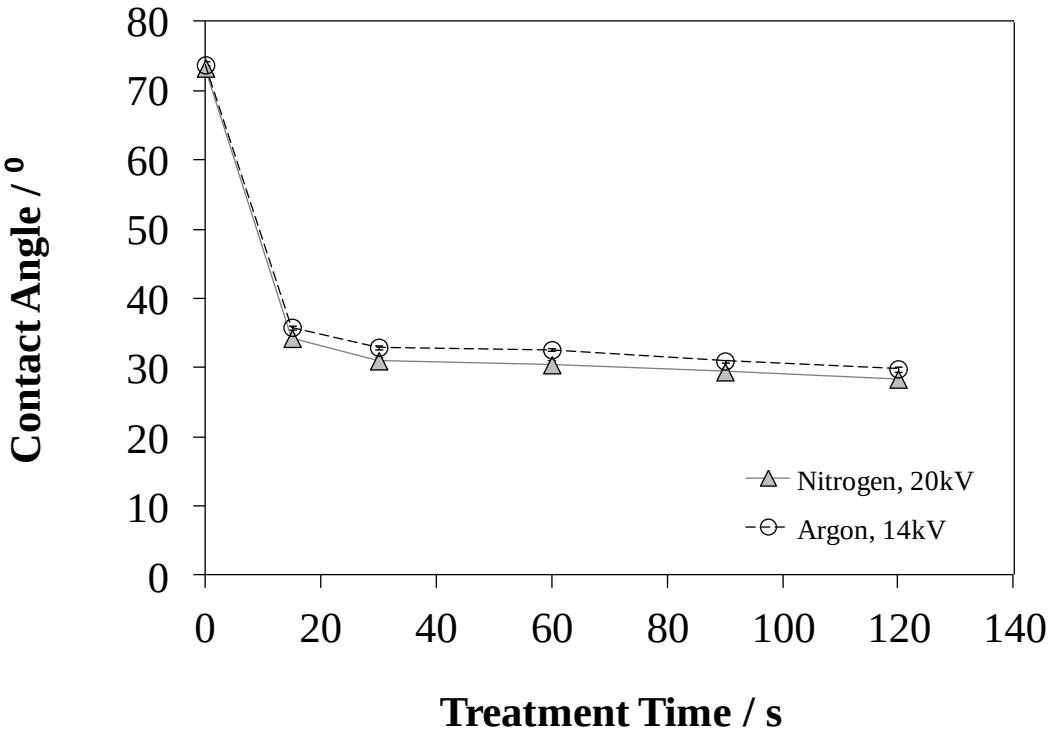


**Figure 5.3.** The water contact angle value as a function of various treatment times for Nitrogen and Argon treatment with peak-to-peak voltage of 20 kV and 14.4 kV respectively.

## 5.2 Ageing Effect

The ageing effect on the treated surface was investigated for 168 hours. We chose the samples treated for 120 s where the smallest contact angle was obtained for this investigation. The treated films were stored in a Petri dish at room temperature. The plot of the water contact angle of $N_2$ and Ar treated Mylar film against the ageing time is depicted in Figs. 5.4 (a)-(b). A rapid increase in the water contact angle was observed during the first 3 hours as shown in Fig. 5.4(b). The recovery slowed down after 3 hours of storage and reached saturation when the ageing time $\geq$ 72 hours. The reduction in contact angle is 16.8% and 15.2% for $N_2$ and Ar DBD jets treatment respectively, compared to the untreated surface after ageing for 168 hours. The hydrophobic recovery is not 100% where the treated film did not fully recover to the untreated state even after 50 days of ageing. This phenomenon where the hydrophobic recovery is observed with

the increase of ageing time is in agreement with the findings as reported in many literatures (Kim et al. 2003; Cheng, Liye, & Zhan, 2006; Ren, Wang, & Qiu, 2008). Factors which have influence on the ageing process include the ambient conditions such as relative humidity, temperature and storage pressure as examined by De Geyter et al. Their results showed that the increasing relative humidity and temperature accelerate the hydrophobic recovery while the storage pressure exerts no influence on the ageing process (De Geyter, Morent, & Leys, 2008). Although the test regarding to the influence of ambient conditions on the treated sample was not carried out in this work, but this influence cannot be neglected.

The contact angle is related to the surface energy. Surface energy increases after plasma treatment. Similar results on the surface treatment for polyethylene and polypropylene in atmospheric pressure glow discharge using typical DBD arrangement with two planar electrodes was described by Sira et al. The group reported the surface free energy increased after the treatment and reached a constant value at 7 s and longer time for polyethylene and polypropylene surface by using pure $N_2$ gas (Sira et al., 2005).

DBD is a plasma source which is able to produce highly reactive species. This is revealed from the study of emission spectra in Chapter 4. Radicals O and OH were observed in Ar DBD jet (Figs. 4.31 & 4.32) while radicals O and N were observed in $N_2$ DBD jet (Figs. 4.20 & Fig. B.1 in Appendix B). It is believed that these reactive species have strong influence on the surface activation. According to Massines et al., the reactive species such as photons, OH radicals, electrons and metastables are able to break the C-C or C-H bonds of the polymer to create polymer radicals (Massines et al., 1998). These polymer radicals will either recombine between each other leading to cross-linking or they can easily react with the active radicals produced from the jet stream (O•, N•) and oxygen ($O_2$) from the air which is possible to introduce new oxygen containing functional groups or nitrogen containing functional groups on the polymer

surface (Massines, Gouda, Gherardi, Duran, & Croquesel, 2001). The presence of new functional groups such as o−c=o, c−o, c=o on the treated surface depend on the type of the surface being treated and this groups cause the increase of surface energy (De Geyter, Morent, Leys, Gengembre, & Payen, 2007). As a result, smaller contact angle was obtained and the surface changes its property from hydrophobic to hydrophilic.

The polar functional groups did not remain on the treated surface as it decreases after treatment resulting in the hydrophobic recovery where increase of contact angle was observed as shown in Fig. 5.4 (a). This is due to the reduction of surface energy where the polar functional groups migrated from the treated surface to the polymer bulk by rotational and translational motions. The treated surface will be replaced by non-polar groups as reported by Chatelier et al. (Chatelier, Xie, Gengenbach, & Griesser, 1995). This surface reorientation is incomplete where some of the polar functional groups are attached to the immobile chain segments on the surface, preventing them from migrating to the bulk of the treated surface. Hence, the contact angle of the treated sample does not revert to the initial condition of untreated surface (Griesser, Youxian, Hughes, Gengenbach, & Mau, 1991).

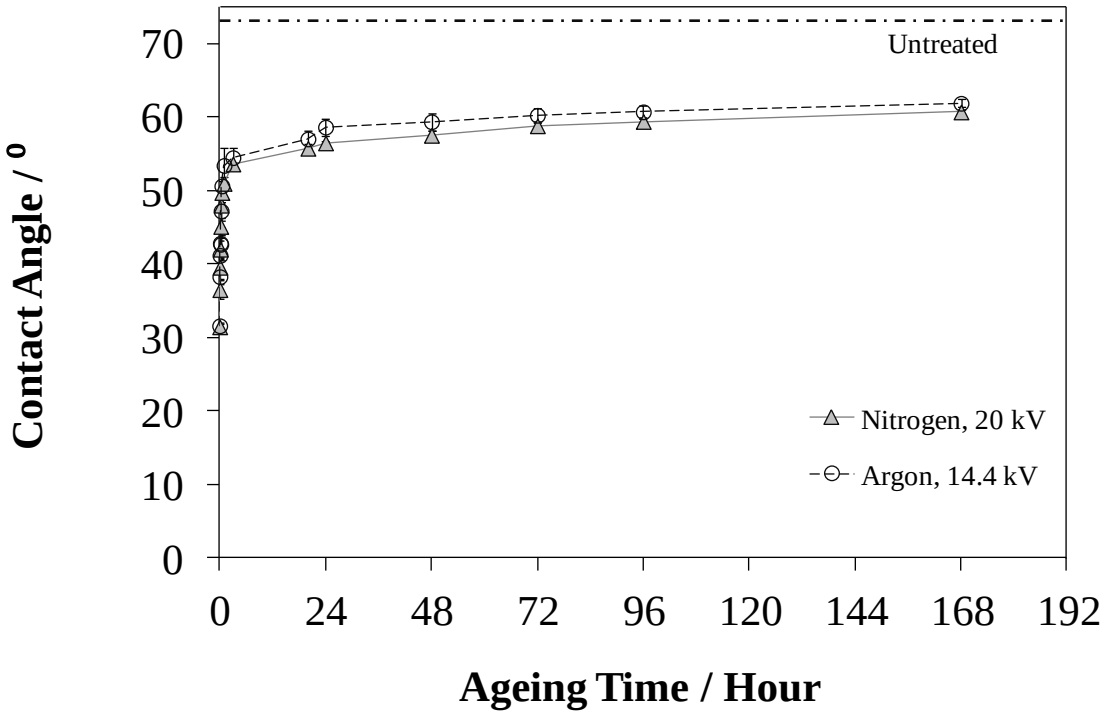


**Figure 5.4 (a).** The water contact angle of $N_2$ and Ar DBD jets treated films against ageing time at room temperature.

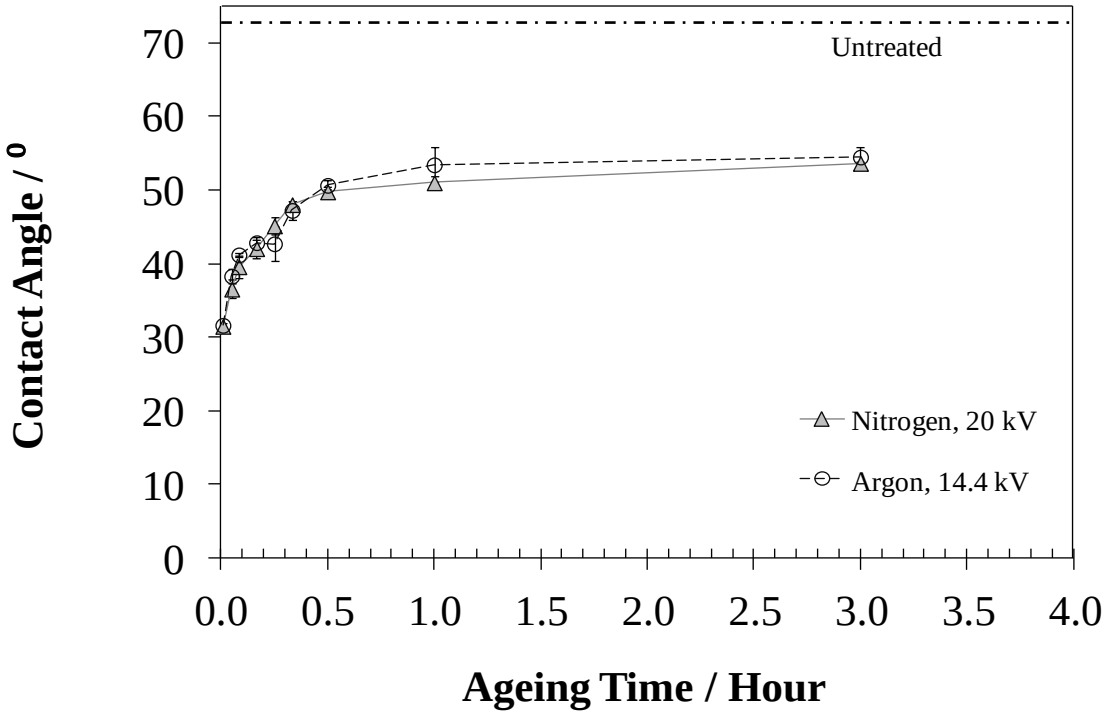


**Figure 5.4 (b).** The water contact angle of $N_2$ and Ar DBD jets treated films for the first 3 hours of ageing time.

# CHAPTER 6

## Conclusion and Suggestions

### 6.1 Conclusion

#### 6.1.1 Electrical Characteristics

A plasma jet system was constructed utilizing DBD to generate a discharge and the jet was extruded from a nozzle with applied gas flow. The ignition voltage was found to be lowest for Argon and highest for Nitrogen gas as Argon has lower dielectric strength; and it increased with increasing gas flow rate. Increased flow rate resulted in pressure built-up within the discharge enclosure, hence, requiring more energy for discharge ignition.

The discharge was operated in filamentary mode with presence of multiple current filaments (spikes in the current waveform). Ease of breakdown in Ar gas led to the highest number of positive current filaments recorded for Ar DBD jet. The number of positive current filaments was found to increase with applied voltage but decrease with increasing gas flow rate and gap width for both Ar and $N_2$ DBD jets. A 'lead' positive and negative current filament of longer duration (100-400 ns) compared to typical single current filament (10-20 ns) was peculiarly observed only in Ar DBD jet. This may be attributed to the corona glow present along the entire length of the glass test-tube (in contrast to $N_2$, the discharge was confined to the rounded end of the test-tube near the nozzle grounded plate).

The charge transferred, energy and mean power dissipated per cycle in the DBD depend strongly on the operating parameters such as gas composition, gas flow rate,

applied voltage, and gap width. The amount of charge transferred, energy and mean power dissipated follow the trend, Ar > Ar:$N_2$ > $N_2$. Fewer charges were transferred in the DBD at higher gas flow rate, as were the mean energy and power dissipated. These are consistent with less current filaments observed. The increase in pressure built-up (at higher gas flow) within the inter-electrode region inhibited ionization processes but contributed effectively to more charge being transported out in the effluent plasma jet (though not obvious in the Ar discharge due to the large discharge area). Increase in the charges transported out in the plasma jet resulted in brighter and longer jets. Higher applied voltage also produced brighter and longer jets in all gas compositions. In this comparative study, the optimum conditions to form the brightest and longest DBD jet are: applied voltage of 14 kV (peak-to-peak) at12.5 LPM in Ar gas.

### 6.1.2 Optical Characteristics

Typical $N_2$ second positive system with the highest peak at 337.13 nm was observed from the study of emission spectra from $N_2$ DBD jet at the shorter wavelength range whilst $N_2$ first positive system and Herman's IR system dominated at the longer wavelength range. Emission lines of lower intensity including those of atomic oxygen and nitrogen (O, N) were also identified. The production of O and N might have further interacted with $O_2$ in ambient air, leading to ozone formation.

From the measured emission spectra from Ar DBD jet, typical Ar I and Ar II lines with transition from $4p \rightarrow 4s$ were present. Other species such as O, OH as well as $N_2$ second positive system were also produced in the jet due to interaction of the jet with ambient air and water vapour impurity in the gas.

Intensity of selected lines demonstrated increase with flow rate. This could indicate that the density of the plasma jets in both $N_2$ and Ar gases increases with flow rate. The

existence of reactive species such as O, N and OH showed the potential of DBD jet in surface treatment.

### 6.1.3 Surface Treatment

The $N_2$ and Ar DBD jets were employed for treatment of the surface of Mylar film. The effect was measured through contact angle measurement. Both $N_2$ and Ar DBD jets showed ability to improve the hydrophilic property of the Mylar film. The contact angle on the treated surface was significantly reduced even for a short treatment time of 15 s. The surface wettability was enhanced with increased treatment time, but tending to saturate after 30 s. Increase in surface wettability leads to increase of surface energy. This might be due to changes of surface chemical compositions where oxygen or nitrogen containing polar functional groups could be incorporated onto the treated surface. Presence of reactive species (OH, O and N) was evident from the measured emission spectra. However, the enhanced hydrophilic surface was time-dependent as it recovered to 80% of its original hydrophobic nature after 1 day of storage.

## 6.2 Suggestions for Further Work

To enhance understanding of the physical processes in the DBD jet and to improve the jet formation, the following suggestions are proposed:

a) The length of the DBD jet obtained in the present configuration is short as most of the charges were confined within the inter-electrode space due to the constriction of the nozzle. Hence, the design of DBD jet should allow smooth (unobstructed and laminar) flow to produce longer jet with enhanced uniformity.
b) Though the plasma jet obtained is safe to be touched (no pain was felt when in contact with the finger), the gas temperature should be measured to avoid

damage to the surface being treated especially thermally sensitive surface. This can be done through actinometric spectroscopy.

c) The lack of discharge homogeneity by DBD jet in the present system (filamentary) needs to be improved to enhance stability of the jet under a variety of gas compositions. Homogeneous DBD will increase the efficiency of surface treatment in addition to uniformity over area to be treated. Higher percentage of reactive species is able to reach the treated surface resulting in enhancement of the hydrophilic property of the surface.

d) An electrical model (equivalent electrical circuit) of the DBD jet should to be simulated to compare with experimental results. This study will lead to deeper understanding of the electrical characteristics of the DBD jet.

e) The treated surface should be analyzed by AFM (atomic force microscopy) and XPS (X-ray photoelectron spectroscopy) to determine the chemical composition of the treated surface as well as to obtain the surface morphology to enhance understanding of the interaction of the species produced in the jet with the treated surface.

# APPENDIX A

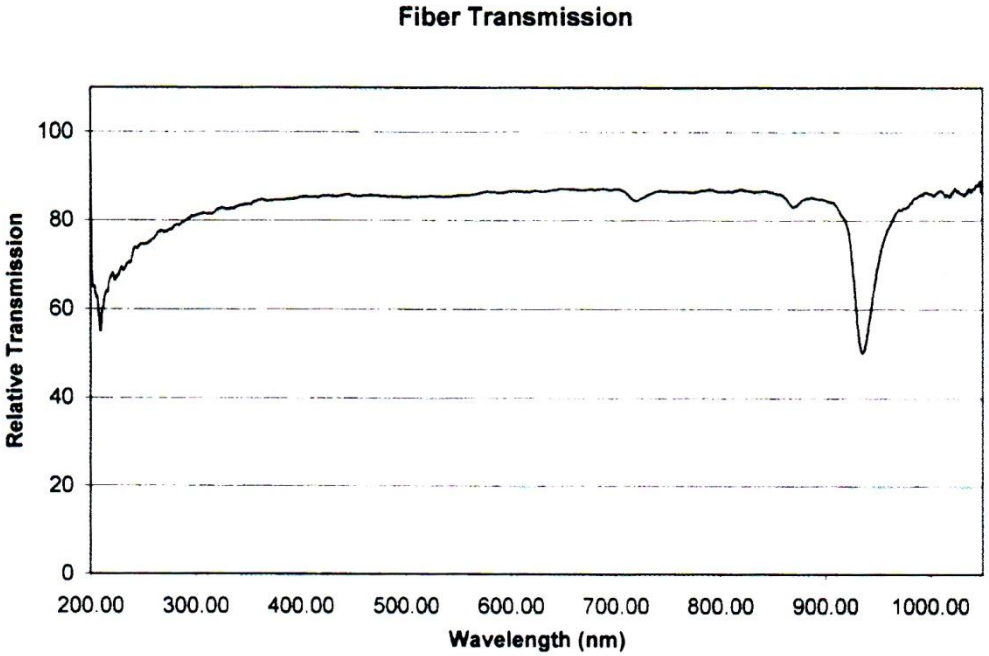


**Figure A.1.** The relative transmission curve of the optical fibre used with HR 4000 spectrometer for wavelength 200 nm - 1000 nm.

# APPENDIX B

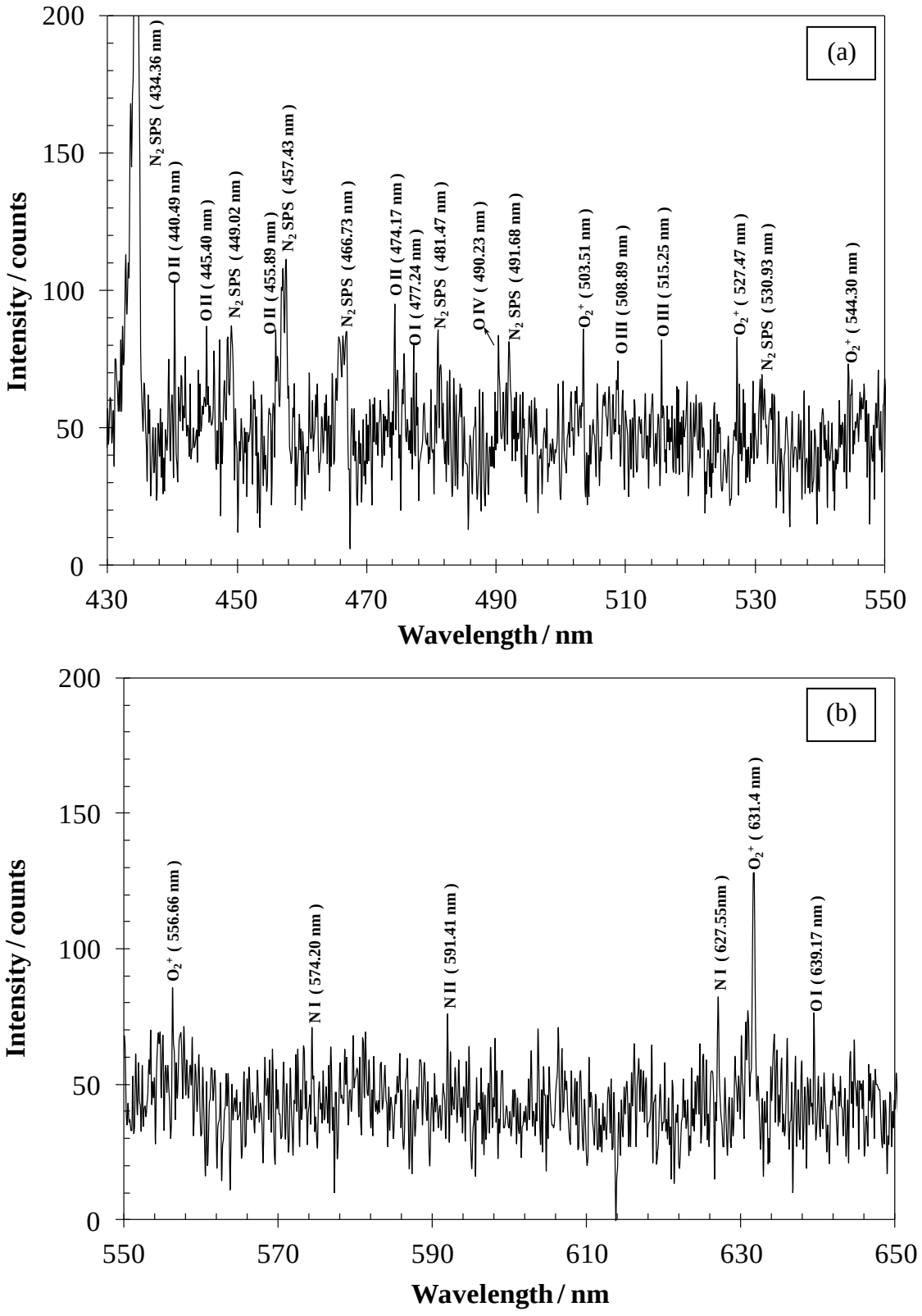


**Figure B.1.** The emission lines of DBD jet at lower intensity (< 200 counts) for the wavelength ranging from (a) 440 nm - 550 nm and (b) 550 nm - 650 nm.

| Ion | Observed wavelength (nm) | Lower level configuration – Upper level configuration | Term |
|---|---|---|---|
| Ar II | 315.43 | $3s^2 3p^4(^1D)3d$ - $3s^2 3p^4(^3P_1)5f$ | $^2P$ - $^2[2]°$ |
| Ar II | 315.82 * | $3s^2 3p^4(^1S)3d$ - $3s^2 3p^4(^3P_1)6f$ | $^2D$ - $^2[2]°$ |
| Ar II | 316.14 * | $3s^2 3p^4(^3P)4p$ - $3s^2 3p^4(^3P)4d$ | $^2S°$ - $^2D$ |
| Ar II | 316.35 * | $3s^2 3p^4(^1D)4p$ - $3s^2 3p^4(^3P)5d$ | $^2P°$ - $^2D$ |
| Ar II | 319.89 * | $3s^2 3p^4(^1D)4p$ - $3s^2 3p^4(^3P)5d$ | $^2F°$ - $^4P$ |
| Ar II | 324.75 * | $3s^2 3p^4(^1D)3d$ - $3s^2 3p^4(^3P_2)5f$ | $^2P$ - $^2[1]°$ |
| Ar II | 325.40 | $3s^2 3p^4(^3P)4p$ - $3s^2 3p^4(^3P)4d$ | $^4P°$ - $^4F$ |
| Ar II | 325.93 * | $3s^2 3p^4(^1D)3d$ - $3s^2 3p^4(^1D)5p$ | $^2D$ - $^2P°$ |
| Ar II | 373.34 * | $3s^2 3p^4(^3P)4p$ - $3s^2 3p^4(^3P)4d$ | $^2D°$ - $^4P$ |
| Ar II | 375.67 * | $3s^2 3p^4(^1D)4p$ - $3s^2 3p^4(^3P)5d$ | $^2D°$ - $^4D$ |
| Ar II | 382.33 * | $3s^2 3p^4(^1D)3d$ - $3s^2 3p^4(^3P)5p$ | $^2F$ - $^4D°$ |
| Ar II | 384.54 * | $3s^2 3p^4(^3P)4s$ - $3s^2 3p^4(^3P)4p$ | $^4P$ - $^2P°$ |
| Ar II | 405.29 | $3s^2 3p^4(^1S)4s$ - $3s^2 3p^4(^1S)4p$ | $^2S$ - $^2P°$ |
| Ar II | 406.05 | $3s^2 3p^4(^3P)4s$ - $3s^2 3p^4(^3P)4p$ | $^4P$ - $^2P°$ |
| Ar I | 415.86 | $3s^2 3p^5(^2P°_{3/2})4s$ - $3s^2 3p^5(^2P°_{3/2})5p$ | $^2[^3/_2]°$ - $^2[^3/_2]$ |
| Ar II | 417.84 | $3s^2 3p^4(^3P)4s$ - $3s^2 3p^4(^3P)4p$ | $^4P$ - $^4D°$ |
| Ar I | 419.83 | $3s^2 3p^5(^2P°_{3/2})4s$ - $3s^2 3p^5(^2P°_{3/2})5p$ | $^2[^3/_2]°$ - $^2[^1/_2]$ |
| Ar I | 427.22 | $3s^2 3p^5(^2P°_{3/2})4s$ - $3s^2 3p^5(^2P°_{3/2})5p$ | $^2[^3/_2]°$ - $^2[^3/_2]$ |
| Ar I | 430.01 | $3s^2 3p^5(^2P°_{3/2})4s$ - $3s^2 3p^5(^2P°_{3/2})5p$ | $^2[^3/_2]°$ - $^2[^5/_2]$ |
| Ar I | 696.54 | $3s^2 3p^5(^2P°_{3/2})4s$ - $3s^2 3p^5(^2P°_{1/2})4p$ | $^2[^3/_2]°$ - $^2[^1/_2]$ |
| Ar I | 706.72 | $3s^2 3p^5(^2P°_{3/2})4s$ - $3s^2 3p^5(^2P°_{1/2})4p$ | $^2[^3/_2]°$ - $^2[^3/_2]$ |
| Ar I | 714.70 | $3s^2 3p^5(^2P°_{3/2})4s$ - $3s^2 3p^5(^2P°_{1/2})4p$ | $^2[^3/_2]°$ - $^2[^3/_2]$ |
| Ar I | 727.29 | $3s^2 3p^5(^2P°_{3/2})4s$ - $3s^2 3p^5(^2P°_{1/2})4p$ | $^2[^3/_2]°$ - $^2[^1/_2]$ |
| Ar I | 738.40 | $3s^2 3p^5(^2P°_{3/2})4s$ - $3s^2 3p^5(^2P°_{1/2})4p$ | $^2[^3/_2]°$ - $^2[^3/_2]$ |
| Ar II | 750.52 | $3s^2 3p^4(^3P)4p$ - $3s^2 3p^4(^1D)3d$ | $^2S°$ - $^2P$ |
| Ar I | 751.46 | $3s^2 3p^5(^2P°_{3/2})4s$ - $3s^2 3p^5(^2P°_{3/2})4p$ | $^2[^3/_2]°$ - $^2[^1/_2]$ |
| Ar I | 763.51 | $3s^2 3p^5(^2P°_{3/2})4s$ - $3s^2 3p^5(^2P°_{3/2})4p$ | $^2[^3/_2]°$ - $^2[^3/_2]$ |
| Ar I | 772.42 | $3s^2 3p^5(^2P°_{1/2})4s$ - $3s^2 3p^5(^2P°_{1/2})4p$ | $^2[^1/_2]°$ - $^2[^1/_2]$ |
| Ar I | 794.82 | $3s^2 3p^5(^2P°_{1/2})4s$ - $3s^2 3p^5(^2P°_{1/2})4p$ | $^2[^1/_2]°$ - $^2[^3/_2]$ |
| Ar I | 800.62 | $3s^2 3p^5(^2P°_{3/2})4s$ - $3s^2 3p^5(^2P°_{3/2})4p$ | $^2[^3/_2]°$ - $^2[^3/_2]$ |
| Ar I | 801.67 | $3s^2 3p^5(^2P°_{1/2})4p$ - $3s^2 3p^5(^2P°_{3/2})6s$ | $^2[^3/_2]$ - $^2[^3/_2]°$ |
| Ar I | 810.37 | $3s^2 3p^5(^2P°_{3/2})4s$ - $3s^2 3p^5(^2P°_{3/2})4p$ | $^2[^3/_2]°$ - $^2[^3/_2]$ |
| Ar I | 811.53 | $3s^2 3p^5(^2P°_{3/2})4s$ - $3s^2 3p^5(^2P°_{3/2})4p$ | $^2[^3/_2]°$ - $^2[^5/_2]$ |
| Ar I | 826.45 | $3s^2 3p^5(^2P°_{1/2})4s$ - $3s^2 3p^5(^2P°_{1/2})4p$ | $^2[^1/_2]°$ - $^2[^1/_2]$ |
| Ar II | 841.19 | $3s^2 3p^4(^3P)4d$ - $3s^2 3p^4(^3P_1)4f$ | $^4D$ - $^2[2]°$ |
| Ar I | 842.46 | $3s^2 3p^5(^2P°_{3/2})4s$ - $3s^2 3p^5(^2P°_{3/2})4p$ | $^2[^3/_2]°$ - $^2[^5/_2]$ |
| Ar I | 852.14 | $3s^2 3p^5(^2P°_{1/2})4s$ - $3s^2 3p^5(^2P°_{1/2})4p$ | $^2[^1/_2]°$ - $^2[^3/_2]$ |
| Ar II | 867.47 | $3s^2 3p^4(^3P)5p$ - $3s^2 3p^4(^3P)5d$ | $^2P°$ - $^4F$ |
| Ar I | 912.30 | $3s^2 3p^5(^2P°_{3/2})4s$ - $3s^2 3p^5(^2P°_{3/2})4p$ | $^2[^3/_2]°$ - $^2[^1/_2]$ |
| Ar I | 922.45 | $3s^2 3p^5(^2P°_{1/2})4s$ - $3s^2 3p^5(^2P°_{3/2})4p$ | $^2[^1/_2]°$ - $^2[^3/_2]$ |
| Ar I | 965.78 | $3s^2 3p^5(^2P°_{3/2})4s$ - $3s^2 3p^5(^2P°_{3/2})4p$ | $^2[^3/_2]°$ - $^2[^1/_2]$ |

**Table B.1.** The configurations and terms for the atomic (Ar I) and ionic (Ar II) Ar lines detected from 300 nm - 1000 nm. All the lines are shown in Figs. 4.31 & 4.32 except lines with low intensity (marked with *). (Kramida et al.,2012)

# REFERENCES


Anghel, S. D., & Simon, A. (2007). An alternative source for generating atmospheric pressure non-thermal plasmas. *Plasma Sources Sci. Technol.*, *16*(3), B1-B4.

Auday, G., Guillot, P., Galy, J., & Brunet, H. (1998). Experimental study of the effective secondary emission coefficient for rare gases and copper electrodes. *J. Appl. Phys.*, *83*(11), 5917-5921.

Babayan, S. E., Jeong, J. Y., Schütze, A., Tu, V. J., Moravej, M., Selwyn, G. S., & Hicks, R. F. (2001). Deposition of silicon dioxide films with a non-equilibrium atmospheric-pressure plasma jet. *Plasma Sources Sci. Technol.*, *10*(4), 573-578.

Babayan, S. E., Jeong, J. Y., Tu, V. J., Park, J., Selwyn, G. S., & Hicks, R. F. (1998). Deposition of silicon dioxide films with an atmospheric-pressure plasma jet. *Plasma Sources Sci. Technol.*, *7*(3), 286-288.

Banik, I., Kim, K. S., Yun, Y. I., Kim, D. H., Ryu, C. M., Park, C. S., … Park, C. E. (2003). A closer look into the behavior of oxygen plasma-treated high-density polyethylene. *Polymer*, *44*(4), 1163-1170.

Bartnikas, R. (1968). Note on discharges in helium under a.c. conditions. *J. Phys. D: Appl. Phys.*, *1*, 659-661.

Bartnikas, R., Radu, I., & Wertheimer, M. R. (2007). Dielectric electrode surface effects on atmospheric pressure glow discharges in helium. *IEEE Trans. Plasma Sci.*, *35*(5), 1437-1447.

Benedikt, J., Focke, K., Yanguas-Gil, A., & von Keudell, A. (2006). Atmospheric pressure microplasma jet as a depositing tool. *Appl. Phys. Lett.*, *89*(25), 251504.

Bertrand, P., Ignatiev, M., Flamant, G., & Smurov, I. (2000). Pyrometry applications in thermal plasma processing. *Vacuum*, *56*, 71-76.

Boeuf, J. P. (2003). Plasma display panels: physics, recent developments and key issues. *J. Phys. D: Appl. Phys.*, *36*(6), R53-R79.

Bonizzoni, G., & Vassallo, E. (2002). Plasma physics and technology; industrial applications. *Vacuum*, *64*(3-4), 327-336.

Borcia, G., Anderson, C. A., & Brown, N. M. D. (2004). The surface oxidation of selected polymers using an atmospheric pressure air dielectric barrier discharge. Part I. *Appl. Surf. Sci.*, *221*(1-4), 203-214.

Boulos, M. I. (1991). Thermal plasma processing. *IEEE Trans. Plasma Sci.*, *19*(6), 1078-1089.

Braun, D., Gibalov, V., & Pietsch, G. (1992). Two-dimensional modelling of the dielectric barrier discharge in air. *Plasma Sources Sci. Technol.*, *1*(3), 166-174.

Cao, Z., Walsh, J. L., & Kong, M. G. (2009). Atmospheric plasma jet array in parallel electric and gas flow fields for three-dimensional surface treatment. *Appl. Phys. Lett.*, *94*(2), 021501.

Chae, J. O. (2003). Non-thermal plasma for diesel exhaust treatment. *J. Electrostat.*, *57*(3-4), 251-262.

Chan, C. M., Ko, T. M., & Hiraoka, H. (1996). Polymer surface modification by plasmas and photons. *Surf. Sci. Rep.*, *24*(1-2), 1-54.

Chang, J. S. (2001). Recent development of plasma pollution control technology: a critical review. *Sci. Technol. Adv. Mater.*, *2*, 571-576.

Chatelier, R. C., Xie, X., Gengenbach, T. R., & Griesser H. J. (1995). Quantitative analysis of polymer surface restructuring. *Langmuir*, *11*(7), 2576-2584.

Chen, G., Chen, S., Zhou, M., Feng, W., Gu, W., & Yang, S. (2006). The preliminary discharging characterization of a novel APGD plume and its application in organic contaminant degradation. *Plasma Sources Sci. Technol.*, *15*(4), 603-608.

Chen, Z., & Mathur, V. K. (2002). Nonthermal plasma for gaseous pollution control. *Ind. Eng. Chem. Res.*, *41*(9), 2082-2089.

Cheng, C., Liye, Z. & Zhan, R. J. (2006). Surface modification of polymer fibre by the new atmospheric pressure cold plasma jet. *Surf. Coat. Technol.*, *200*(24), 6659-6665.

Chiang, M. H., Wu, J. Y., Li, Y. H., Wu, J. S., Chen, S. H., & Chang, C. L. (2010). Inactivation of E. coli and B. subtilis by a parallel-plate dielectric barrier discharge jet. *Surf. Coat. Technol.*, *204*(21-22), 3729-3737.

Chirokov, A., Gutsol, A., & Fridman, A. (2005). Atmospheric pressure plasma of dielectric barrier discharges. *Pure Appl. Chem.*, *77*(2), 487-495.

Cho, G., Lim, H., Kim, J. H., Jin, D. J., Kwon, G. C., Choi, E. H., & Uhm, H. S. (2011). Cold plasma jets made of a syringe needle covered with a glass tube. *IEEE Trans. Plasma Sci.*, *39*(5), 1234-1238.

Choi, J. H., Han, I., Baik, H. K., Lee, M. H., Han, D. W., Park, J. C., … Lim, Y. S. (2006). Analysis of sterilization effect by pulsed dielectric barrier discharge. *J. Electrostat.*, *64*(1), 17-22.

Corrosionist. (n.d.). *Why does Copper turn green?* Retrieved 10 April 2012 from http://www.corrosionist.com/why_does_copper_turn_green.htm

De Geyter, N., Morent, R. & Leys, C. (2008). Influence of ambient conditions on the ageing behaviour of plasma-treated PET surfaces. *Nucl. Instrum. Methods Phys. Res. Sect. B-Beam Interact. Mater. Atoms.*, *226*(12-13), 3086-3090.

De Geyter, N., Morent, R., Leys, C., Gengembre, L., & Payen, E. (2007). Treatment of polymer films with a dielectric barrier discharge in air, helium and argon at medium pressure. *Surf. Coat. Technol.*, *201*(16-17), 7066-7075.

De Geyter, N., Morent, R., Van Vlierberghe, S., Dubruel, P., Leys, C., Gengembre, L., … Payen, E. (2009). Deposition of polymethyl methacrylate on polypropylene substrates using an atmospheric pressure dielectric barrier discharge. *Prog. Org. Coat.*, *64*(2–3), 230-237.

Dinescu, G., & Ionita, E. R. (2008). Radio frequency expanding plasmas at low, intermediate, and atmospheric pressure and their applications. *Pure Appl. Chem.*, *80*(9), 1919-1930.

Dobrynin, D., Fridman, G., Friedman, G., & Fridman, A. (2009). Physical and biological mechanisms of direct plasma interaction with living tissue. *New J. Phys.*, *11*, 115020.

Dong, L., Yin, Z., Wang, L., Fu, G., He, Y., Chai, Z., & Li, X. (2003). Square pattern formation in a gas discharge system. *Thin Solid Films*, *435*(1-2), 120-123.

Dudek, D., Bibinov, N., Engemann, J., & Awakowicz, P. (2007). Direct current plasma jet needle source. *J. Phys. D: Appl. Phys.*, *40*(23), 7367-7371.

Ehlbeck, J., Schnabel, U., Polak, M., Winter, J., von Woedtke, T., Brandenburg, R., . . . Weltmann, K D. (2011). Low temperature atmospheric pressure plasma sources for microbial decontamination. *J. Phys. D: Appl. Phys.*, *44*, 013002.

Eliasson, B., & Kogelschatz, U. (1991a). Modeling and applications of silent discharge plasmas. *IEEE Trans. Plasma Sci.*, *19*(2), 309-323.

Eliasson, B., & Kogelschatz, U. (1991b). Nonequilibrium volume plasma chemical processing. *IEEE Trans. Plasma Sci.*, *19*(6), 1063-1077.

Falkenstein, Z., & Coogan, J. J. (1997). Microdischarge behaviour in the silent discharge of nitrogen-oxygen and water-air mixtures. *J. Phys. D: Appl. Phys.*, *30*(5), 817-825.

Fang, Z., Qiu, Y., & Luo, Y. (2003). Surface modification of polytetrafluoroethylene film using the atmospheric pressure glow discharge in air. *J. Phys. D: Appl. Phys.*, *36*(23), 2980-2985.

Fang, Z., Yang, H., & Qiu, Y. (2010). Surface treatment of polyethylene terephthalate films using a microsecond pulse homogeneous dielectric barrier discharges in atmospheric air. *IEEE Trans. Plasma Sci.*, *38*(7), 1615-1623.

Fauchais, P., & Vardelle, A. (1997). Thermal plasmas. *IEEE Trans. Plasma Sci.*, *25*(6), 1258-1280.

Foest, R., Kindel, E., Ohl, A., Stieber, M., & Weltmann, K. D. (2005). Non-thermal atmospheric pressure discharges for surface modification. *Plasma Phys. Control. Fusion*, *47*, B252-B536.

Fridman, G., Peddinghaus, M., Ayan, H., Fridman, A., Balasubramanian, M., Gutsol, A., … Friedman G. (2006). Blood coagulation and living tissue sterilization by floating-electrode dielectric barrier discharge in air. *Plasma Chem. Plasma Process.*, *26*(4), 425-442.

Gherardi, N., Gouda, G., Gat, E., Ricard, A., & Massines, F. (2000). Transition from glow silent discharge to micro-discharges in nitrogen gas. *Plasma Sources Sci. Technol., 9*(3), 340-346.

Gibalov, V. I., & Pietsch, G. J. (2000). The development of dielectric barrier discharges in gas gaps and on surfaces. *J. Phys. D: Appl. Phys., 33*(20), 2618-2636.

Griesser, H. J., Youxian, D., Hughes, A. E., Gengenbach, T. R., & Mau, A. W. H. (1991). Shallow reorientation in the surface dynamics of plasma-treated fluorinated ethylene-propylene polymer. *Langmuir, 7*(11), 2484-2491.

Hong, Y. C., & Uhm, H. S. (2006). Microplasma jet at atmopsheric pressure. *Appl. Phys. Lett., 89*(22), 221504.

Hoult, A. P., Pashby, I. R., & Chan, K. (1995). Fine plasma cutting of advanced aerospace materials. *J. Mater. Process. Technol., 48*(1-4), 825-831.

Hubicka, Z., Cada, M., Sicha, M., Churpita, A., Pokorny, P., Soukup, L., & Jastrabik, L. (2002). Barrier-torch discharge plasma source for surface treatment technology at atmospheric pressure. *Plasma Sources Sci. Technol., 11*(2), 195-202.

Ionita, E. R., Ionita, M. D., Stancu, E. C., Teodorescu, M., & Dinescu, G. (2009). Small size plasma tools for material processing at atmospheric pressure. *Appl. Surf. Sci., 255*(10), 5448-5452.

Janca, J., Klima, M., Slavicek, P., & Zajickova, L. (1999). HF plasma pencil—new source for plasma surface processing. *Surf. Coat. Technol., 116-119*, 547-551.

Jasinski, M., Mizeraczyk, J., Zakrzewski, Z., Ohkubo, T., & Chang, J. S. (2002). CFC-11 destruction by microwave torch generated atmospheric-pressure nitrogen discharge. *J. Phys. D: Appl. Phys., 35*(18), 2274-2280.

Jeong, H. S., Shin, B. J., & Whang, K. W. (1999). Two-dimensional multifluid modeling of the He-Xe discharge in an AC plasma display panel. *IEEE Trans. Plasma Sci., 27*(1), 171-181.

Jeong, J. Y., Babayan, S. E., Schutze, A., Tu, V. J., Park, J., Henins, I., … Hicks, R. F. (1999). Etching polyimide with a nonequilibrium atmospheric-pressure plasma jet. *J. Vac. Sci. Technol. A*, 17(5), 2581-2585.

Jeong, J. Y., Babayan, S. E., Tu, V. J., Park, J., Henins, I., Hicks, R. F., & Selwyn, G. S. (1998). Etching materials with an atmospheric-pressure plasma jet. *Plasma Sources Sci. Technol., 7*(3), 282-285.

Jiang, N., Ji, A., & Cao, Z. (2009). Atmospheric pressure plasma jet: Effect of electrode configuration, discharge behavior, and its formation mechanism. *J. Appl. Phys., 106*(1), 013308.

Jiang, N., Ji, A., & Cao, Z. (2010). Atmospheric pressure plasma jets beyond ground electrode as charge overflow in a dielectric barrier discharge setup. *J. Appl. Phys., 108*(3), 033302.

Jidenko, N., Petit, M., & Borra, J. P. (2006). Electrical characterization of microdischarges produced by dielectric barrier discharge in dry air at atmospheric pressure. *J. Phys. D: Appl. Phys.*, *39*(2), 281-293.

Jones, J. (1968) Ionization coefficients in nitrogen. *J. Phys. D: Appl. Phys.*, *1*, 769-774.

Kachickas, G. A., & Fisher, L. H. (1953). Formative time lags of uniform field breakdown in argon. *Phys. Rev.*, *91*(4), 775-779.

Kalghatgi, S. U., Fridman, G., Cooper, M., Nagaraj, G., Peddinghaus, M., Balasubramanian, M., … Friedman, G. (2007). Mechanism of blood coagulation by nonthermal atmospheric pressure dielectric barrier discharge plasma. *IEEE Trans. Plasma Sci.*, *35*(5), 1559-1566.

Kanazawa, S., Kogoma, M., Moriwaki, T., & Okazaki, S. (1988). Stable glow plasma at atmospheric pressure. *J. Phys. D: Appl. Phys.*, *21*(5), 838-840.

Kim, K. S., Ryu, C. M., Park, C. S., Sur, G. S., & Park, C. E. (2003). Investigation of crystallinity effects on the surface of oxygen plasma treated low density polyethylene using X-ray photoelectron spectroscopy. *Polymer*, *44*(20), 6287-6295.

Kim, M. C., Song, D. K., Shin, H. S., Baeg, S. H., Kim, G. S., Boo, J. H., … Yang, S.H. (2003). Surface modification for hydrophilic property of stainless steel treated by atmospheric-pressure plasma jet. *Surf. Coat. Technol.*, *171*(1-3), 312-316.

Kim, S. J., Chung, T. H., & Bae, S. H. (2009). Characteristic study of atmospheric pressure microplasma jets with various operating conditions. *Thin Solid Films*, *517*(14), 4251-4254.

Kogelschatz, U. (2002). Filamentary, patterned, and diffuse barrier discharges. *IEEE Trans. Plasma Sci.*, *30*(4), 1400-1408.

Kogelschatz, U. (2003). Dielectric-barrier discharges: Their history, discharge physics, and industrial applications. *Plasma Chem. Plasma Process.*, *23*(1), 1-46.

Kogelschatz, U. (2010). Collective phenomena in volume and surface barrier discharges. *J. Phys.: Conf. Ser.*, *257*(1), 012015.

Kogelschatz, U., Akishev, Y. S., & Napartovich, A. P. (2005). History of non-equilibrium air discharges. In K. H. Becker, U. Kogelschatz, K. H. Schoenbach & R. J. Barker (Eds.), *Non-equilibrium air plasmas at atmospheric pressure* (pp. 17-25). London, England: IOP Publishing.

Kogelschatz, U., Eliasson, B., & Egli, W. (1999). From ozone generators to flat television screens: history and future potential of dielectric-barrier discharges. *Pure Appl. Chem.*, *71*(10), 1819-1828.

Koinuma, H., Ohkubo, H., Hoshimoto, T., Inomata, K., Shiraishi, T., Miyanaga, A., & Hayashi, S. (1992). Development and application of a microbeam plasma generator. *Appl. Phys. Lett.*, *60*(7), 816-817.

Kong, P. (2006). Atmospheric-pressure plasma process and applications. In F. Kongoli & R. G. Reddy (Eds.), Sohn international symposium advanced processing of metals and materials: Vol. 6. New, improved and existing technologies: Aqueous and electrochemical processing (pp. 493-506). Warrendale, PA : TMS.

Kostov, K. G., dos Santos, A. L. R., Honda, R. Y., Nascente, P. A. P., Kayama, M. E., Algatti, M. A., & Mota, R. P. (2010). Treatment of PET and PU polymers by atmospheric pressure plasma generated in dielectric barrier discharge in air. *Surf. Coat. Technol.*, *204*(18-19), 3064-3068.

Kostov, K. G., Rocha, V., Koga-Ito, C. Y., Matos, B. M., Algatti, M. A., Honda, R. Y., … Mota, R. P. (2010). Bacterial sterilization by a dielectric barrier discharge (DBD) in air. *Surf. Coat. Technol.*, *204*(18–19), 2954-2959.

Koulik, P., Begounov, S., & Goloviatinskii, S. (1999). Atmospheric plasma sterilization and deodorization of dielectric surfaces. *Plasma Chem. Plasma Process.*, *19*(2), 311-326.

Kramida, A., Ralchenko, Yu., Reader, J., & NIST ASD Team. (2012). *NIST Atomic Spectra Database* (ver. 5.0). Retrieved 31 March 2012 from http://physics.nist.gov/asd.

Laroussi, M. (2002). Nonthermal decontamination of biological media by atmospheric-pressure plasmas: Review, analysis, and prospects. *IEEE Trans. Plasma Sci.*, *30*(4), 1409-1415.

Laroussi, M. (2009). Low-temperature plasmas for medicine? *IEEE Trans. Plasma Sci.*, *37*(6), 714-725.

Laroussi, M., Alexeff, I., & Kang, W. L. (2000). Biological decontamination by nonthermal plasmas. *IEEE Trans. Plasma Sci.*, *28*(1), 184-188.

Laroussi, M., Hynes, W., Akan, T., Lu, X., & Tendero, C. (2008). The plasma pencil: A source of hypersonic cold plasma bullets for biomedical applications. *IEEE Trans. Plasma Sci.*, *36*(4), 1298-1299.

Laroussi, M., & Lu, X. (2005). Room-temperature atmospheric pressure plasma plume for biomedical applications. *Appl. Phys. Lett.*, *87*(11), 113902.

Li, B., Chen, Q., & Liu, Z. W. (2010). A large gap of radio frequency dielectric barrier atmospheric pressure glow discharge. *Appl. Phys. Lett.*, *96*(4), 041502.

Liu, S., & Neiger, M. (2003). Electrical modelling of homogeneous dielectric barrier discharges under an arbitrary excitation voltage. *J. Phys. D: Appl. Phys.*, *36*(24), 3144-3150.

Lofthus, A., & Krupenie, P. H. (1977). The spectrum of molecular nitrogen. *J. Phys. Chem. Ref. Data*, *6*(1), 113-307.

Lu, X. P., Jiang, Z. H., Xiong, Q., Tang, Z. Y., Hu, X. W., & Pan, Y. (2008). An 11 cm long atmospheric pressure cold plasma plume for applications of plasma medicine. *Appl. Phys. Lett.*, *92*(8), 081502.

Lu, X. P., & Laroussi, M. (2006). Dynamics of an atmospheic pressure plasma plume generated by submicrosecond voltage pulses. *J. Appl. Phys.*, *100*, 063302.

Lu, X. P., Xiong, Q., Xiong, Z., Hu, J., Zhou, F., Gong, W., … Pan, Y. (2009). Propagation of an atmospheric pressure plasma plume. *J. Appl. Phys.*, *105*(4), 043304.

Lu, X. P., Ye, T., Cao, Y. G., Sun, Z. Y., Xiong, Q., Tang, Z. Y., … Pan, Y. (2008). The roles of the various plasma agents in the inactivation of bacteria. *J. Appl. Phys.*, *104*(5), 053309.

Ma, H., Chen, P., Zhang, M., Lin, X., & Ruan, R. (2002). Study of $SO_2$ removal using non-thermal plasma induced by dielectric barrier discharge (DBD). *Plasma Chem. Plasma Process.*, *22*(2), 239-254.

Manley, T. C. (1943). The electric characteristics of the ozonator discharge. *J. Electrochem. Soc.*, *84*(1), 83-96.

Massines, F., Gherardi, N., Fornelli, A., & Martin, S. (2005). Atmospheric pressure plasma deposition of thin films by Townsend dielectric barrier discharge. *Surf. Coat. Technol.*, *200*(5–6), 1855-1861.

Massines, F., Gherardi, N., Naude, N., & Segur, P. (2009). Recent advances in the understanding of homogeneous dielectric barrier discharges. *Eur. Phys. J. Appl. Phys.*, *47*(2), 22805.

Massines, F., & Gouda, G. (1998). A comparison of polypropylene-surface treatment by filamentary, homogeneous and glow discharges in helium at atmospheric pressure. *J. Phys. D: Appl. Phys.*, *31*(24), 3411-3420.

Massines, F., Gouda, G., Gherardi, N., Duran, M., & Croquesel, E. (2001). The role of dielectric barrier discharge atmosphere and physics on polypropylene surface treatment. *Plasmas Polym.*, *6*(1-2), 35-49.

Massines, F., Messaoudi, R., & Mayoux, C. (1998). Comparison between air filamentary and helium glow dielectric barrier discharges for the polypropylene surface treatment. *Plasmas Polym.*, *3*(1), 43-59.

Massines, F., Segur, P., Gherardi, N., Khamphan, C., & Ricard, A. (2003). Physics and chemistry in a glow dielectric barrier discharge at atmospheric pressure: diagnostics and modelling. *Surf. Coat. Technol.*, *174-175*, 8-14.

Masuda, S., Akutsu, K., Kuroda, M., Awatsu, Y., & Shibuya, Y. (1988). A ceramic-based ozonizer using high-frequency discharge. *IEEE Trans. Ind. Appl.*, *24*(2), 223-231.

Mericam-Bourdet, N., Laroussi, M., Begum, A., & Karakas, E. (2009). Experimental investigations of plasma bullets. *J. Phys. D: Appl. Phys.*, *42*(5), 055207.

Moisan, M., Sauve, G., Zakrzewski, Z., & Hubert, J. (1994). An atmospheric pressure waveguide-fed microwave plasma torch: the TIA design. *Plasma Sources Sci. Technol.*, *3*(4), 584-592.

Moisan, M., Zakrzewski, Z., & Rostaing, J. C. (2001). Waveguide-based single and multiple nozzle plasma torches: the TIAGO concept. *Plasma Sources Sci. Technol.*, *10*(3), 387-394.

Morfill, G. E., Shimizu, T., Steffes, B., & Schmidt, H. U. (2009). Nosocomial infections—a new approach towards preventive medicine using plasmas. *New J. Phys.*, *11*, 115019.

Morgan, N. N. (2009). Atmospheric pressure dielectric barrier discharge chemical and biological applications. *Int. J. Phys. Sci.*, *4*(13), 885-892.

Nagao, I., Nishida, M., Yukimura, K., Kambara, S., & Maruyama, T. (2002). NOx removal using nitrogen gas activated by dielectric barrier discharge at atmospheric pressure. *Vacuum*, *65*(3-4), 481-487.

Naude, N., Cambronne, J. P., Gherardi, N., & Massines, F. (2005). Electrical model and analysis of the transition from an atmospheric pressure Townsend discharge to a filamentary discharge. *J. Phys. D: Appl. Phys.*, *38*(4), 530-538.

Nikiforov, A. Y., Sarani, A., & Leys, C. (2011). The influence of water vapor content on electrical and spectral properties of an atmospheric pressure plasma jet. *Plasma Sources Sci. Technol.*, *20*(1), 015014.

Nwankire, C. E., Law, V. J., Nindrayog, A., Twomey, B., Niemi, K., Milosavljevic, V., … Dowling, D. P. (2010). Electrical, thermal and optical diagnostics of an atmospheric plasma jet system. *Plasma Chem. Plasma Process.*, *30*(5), 537-552.

Okazaki, S., & Kogoma, M. (1993). Development of atmospheric pressure glow discharge plasma and its application on a surface with curvature. *J. Photopolym. Sci. Technol.*, *6*(3), 339-342.

Okazaki, S., Kogoma, M., Uehara, M., & Kimura, Y. (1993). Appearance of stable glow discharge in air, argon, oxygen and nitrogen at atmospheric pressure using a 50 Hz source. *J. Phys. D: Appl. Phys.*, *26*(5), 889-892.

Pal, U. N., Sharma, A. K., Soni, J. S., Kr, S., Khatun, H., Kumar, M., … Frank, K. (2009). Electrical modelling approach for discharge analysis of a coaxial DBD tube filled with argon. *J. Phys. D: Appl. Phys.*, *42*(4), 045213.

Pappas, D. (2011). Status and potential of atmospheric plasma processing of materials. *J. Vac. Sci. Technol. A*, *29*(2), 020801.

Pearse, R. W. B., & Gaydon, A.G. (1976). *The identification of molecular spectra*, 4th edn. London, England: Chapman and Hall.

Pfender, E. (1999). Thermal plasma technology: Where do we stand and where are we going? *Plasma Chem. Plasma Process.*, *19*(1), 1-31.

Plaksin, V. Y., Penkov, O. V., Ko, M. K., & Lee, H. J. (2010). Exhaust Cleaning with Dielectric Barrier Discharge. *Plasma Sci. Technol.*, *12*(6), 688-691.

Poll, H. U., Schladitz, U., & Schreiter, S. (2001). Penetration of plasma effects into textile structures. *Surf. Coat. Technol., 142-144*, 489-493.

Radu, I., Bartnikas, R., Czeremuszkin, G., & Wertheimer, M. R. (2003). Diagnostics of dielectric barrier discharges in noble gases: Atmospheric pressure glow and pseudoglow discharges and spatio-temporal patterns. *IEEE Trans. Plasma Sci., 31*(3), 411-421.

Raizer, Y. P. (1991). *Gas Discharge Physics*. New York, NY: Springer-Verlag.

Ramakrishnan, S., & Rogozinski, M. W. (1997). Properties of electric arc plasma for metal cutting. *J. Phys. D: Appl. Phys., 30*, 636-644.

Reichen, P., Sonnenfeld, A., & von Rohr, P. R. (2010). Influence of increased velocity on the statistical discharge characteristics of He and air barrier discharges. *J. Phys. D: Appl. Phys., 43*(2), 025207.

Ren, Y., Wang, C., & Qiu, Y. (2008). Aging of surface properties of ultra high modulus polyethylene fibers treated with $He/O_2$ atmospheric pressure plasma jet. *Surf. Coat. Technol., 202*(12), 2670-2676.

Roth, J. R., Nourgostar, S., & Bonds, T. A. (2007). The one atmosphere uniform glow discharge plasma (OAUGDP)—A platform technology for the 21st century. *IEEE Trans. Plasma Sci., 35*(2), 233-250.

Sakamoto, M., Kikuchi, S., & Ohyama, R. (2007). Fundamental characteristics on plasma diagnoses of ges-jet type atmospheric pressure plasma. *Annual Report Conference on Electrical Insulation and Dielectric Phenomena* (pp. 525-528). New York, NY: IEEE.

Salge, J. (1996). Plasma-assisted deposition at atmospheric pressure. *Surf. Coat. Technol., 80*(1-2), 1-7.

Sarani, A., Nikiforov, A. Y., De Geyter, N., Morent, R., & Leys, C. (2011). Surface modification of polypropylene with an atmospheric pressure plasma jet sustained in argon and an argon/water vapour mixture. *Appl. Surf. Sci., 257*(20), 8737-8741.

Schutze, A., Jeong, J. Y., Babayan, S. E., Park, J., Selwyn, G. S., & Hicks, R. F. (1998). The atmospheric-pressure plasma jet: A review and comparison to other plasma sources. *IEEE Trans. Plasma Sci., 26*(6), 1685-1694.

Shao, X. J., Zhang, G. J., Zhan, J. Y., & Xu, G. M. (2011). Research on surface modification of polytetrafluoroethylene coupled with argon dielectric barrier discharge plasma jet characteristics. *IEEE Trans. Plasma Sci., 39*(11), 3095-3102.

Sira, M., Trunec, D., Stahel, P., Bursikova, V., Navratil, Z. & Bursik, J. (2005). Surface modification of polyethylene and polypropylene in atmospheric pressure glow discharge. *J. Phys. D: Appl. Phys., 38* (4), 621-627.

Sjoberg, M., Serdyuk, Y. V., Gubanski, S. M., & Leijon, M. A. S. (2003). Experimental study and numerical modelling of a dielectric barrier discharge in hybrid air–dielectric insulation. *J. Electrostat., 59*(2), 87-113.

Sladek, R. E. J., Stoffels, E., Walraven, R., Tielbeek, P. J. A., & Koolhoven, R. A. (2004). Plasma treatment of dental cavities: A feasibility study. *IEEE Trans. Plasma Sci., 32*(4), 1540-1543.

Sonnenfeld, A., Tun, T. M., Zajickova, L., Kozlov, K. V., Wagner, H. E., Behnke, J. F., & Hippler, R. (2001). Deposition process based on organosilicon precursors in dielectric barrier discharges at atmospheric pressure—a comparison. *Plasmas Polym., 6*(4), 237-266.

Stoffels, E., Kieft, I. E., & Sladek, R. E. J. (2003). Superficial treatment of mammalian cells using plasma needle. *J. Phys. D: Appl. Phys., 36*(23), 2908-2913.

Stoffels, E., Kieft, I. E., Sladek, R. E. J., van den Bedem, L. J. M., van der Laan, E. P., & Steinbuch, M. (2006). Plasma needle for in vivo medical treatment: recent developments and perspectives. *Plasma Sources Sci. Technol., 15*(4), S169-S180.

Takaki, K., Shimizu, M., Mukaigawa, S., & Fujiwara, T. (2004). Effect of electrode shape in dielectric barrier discharge plasma reactor for NOx removal. *IEEE Trans. Plasma Sci., 32*(1), 32-38.

Tendero, C., Tixier, C., Tristant, P., Desmaison, J., & Leprince, P. (2006). Atmospheric pressure plasmas: A review. *Spectrochim. Acta B, 61*(1), 2-30.

Tepper, J., Lindmayer, M., & Salge, J. (1998). Pulsed uniform barrier discharges at atmospheric pressure. *Proc. of 6th Int. Symp. High Pressure, Low Temperature Plasma Chem.* 123-126.

Teschke, M., Kedzierski, J., Finantu-Dinu, E. G., Korzec, D., & Engemann, J. (2005). High-speed photographs of a dielectric barrier atmospheric pressure plasma jet. *IEEE Trans. Plasma Sci., 33*(2), 310-311.

The Physics Hypertextbook. (n.d.). *Density*. Retrieved 30 April 2012 from http://www.physics.info/density/

Toshifuji, J., Katsumata, T., Takikawa, H., Sakakibara, T., & Shimizu, I. (2003). Cold arc-plasma jet under atmospheric pressure for surface modification. *Surf. Coat. Technol., 171*(1-3), 302-306.

Townsend, J. S. (1910). *The theory of ionization of gases by collision*. London, England: Constable & Company, Ltd.

Valdivia-Barrientos, R., Pacheco-Sotelo, J., Pacheco-Pacheco, M., Benitez-Read, J. S., & Lopez-Callejas, R. (2006). Analysis and electrical modelling of a cylindrical DBD configuration at different operating frequencies. *Plasma Sources Sci. Technol., 15*(2), 237-245.

Wagenaars, E., Brandenburg, R., Brok, W. J. M., Bowden, M. D., & Wagner, H. E. (2006). Experimental and modelling investigations of a dielectric barrier discharge in low-pressure argon. *J. Phys. D: Appl. Phys.*, *39*(4), 700-711.

Wagner, H. E., Brandenburg, R., Kozlov, K. V., Sonnenfeld, A., Michel, P., & Behnke, J. F. (2003). The barrier discharge: basic properties and applications to surface treatment. *Vacuum*, *71*, 417-436.

Walsh, J. L., & Kong, M. G. (2007). Room-temperature atmospheric argon plasma jet sustained with submicrosecond high-voltage pulses. *Appl. Phys. Lett.*, *91*(22), 221502.

Wang, C. X., Liu, Y., Xu, H. L., Ren, Y., & Qiu, Y. P. (2008). Influence of atmospheric pressure plasma treatment time on penetration depth of surface modification into fabric. *Appl. Surf. Sci.*, *254*(8), 2499-2505.

Weltmann, K. D., Kindel, E., von Woedtke, T., Hahnel, M., Stieber, M., & Brandenburg, R. (2010). Atmospheric-pressure plasma sources: Prospective tools for plasma medicine. *Pure Appl. Chem.*, *82*(6), 1223-1237.

Weltmann, K. D., & von Woedtke, T. (2011). Campus PlasmaMed—From Basic Research to Clinical Proof. *IEEE Trans. Plasma Sci.*, *39*(4), 1015-1025.

Wu, S. Q., Lu, X. P., Xiong, Z. L., & Pan, Y. (2010). A touchable pulsed air plasma plume driven by DC power supply. *IEEE Trans. Plasma Sci.*, *38*(12), 3404-3408.

Xiong, Q., Lu, X., Ostrikov, K., Xiong, Z., Xian, Y., Zhou, F., … Jiang, Z. (2009). Length control of He atmospheric plasma jet plumes: Effects of discharge parameters and ambient air. *Phys. Plasmas*, *16*(4), 043505.

Xiong, Q., Lu, X. P., Jiang, Z. H., Tang, Z. Y., Hu, J., Xiong, Z. L., & Pan, Y. (2008). An atmospheric pressure nonequilibrium plasma jet device. *IEEE Trans. Plasma Sci.*, *36*(4), 986-987.

Xiong, Q., Nikiforov, A. Y., Lu, X. P., & Leys, C. (2010). High-speed dispersed photographing of an open-air argon plasma plume by a grating–ICCD camera system. *J. Phys. D: Appl. Phys.*, *43*(41), 415201.

Xu, G. M., Ma, Y., & Zhang, G. J. (2008). DBD plasma jet in atmospheric pressure argon. *IEEE Trans. Plasma Sci.*, *36*(4), 1352-1353.

Yip, J., Chan, K., Sin, K. M., & Lau, K. S. (2002). Low temperature plasma-treated nylon fabrics. *J. Mater. Process. Technol.*, *123*(1), 5-12.

Yoshida, T. (1990). The future of thermal plasma processing. *Mater. Trans. JIM*, *31*(1), 1-11.

Zhang, C., Shao, T., Yu, Y., Niu, Z., Yan, P., & Zhou, Y. (2010). Comparison of experiment and simulation on dielectric barrier discharge driven by 50 Hz AC power in atmospheric air. *J. Electrostat.*, *68*(5), 445-452.

Zhang, J., Sun, J., Wang, D., & Wang, X. (2006). A novel cold plasma jet generated by atmospheric dielectric barrier capillary discharge. *Thin Solid Films*, *506-507*, 404-408.